

Dissertation
submitted to the
Combined Faculty of Natural Sciences and Mathematics
of Heidelberg University, Germany
for the degree of
Doctor of Natural Sciences

Put forward by
Tom Segal
born in: Tel Aviv, Israel
Oral examination: 17.10.2019

Mass Measurements of Neon Isotopes at THe-Trap

Referees:

Klaus Blaum

Wolfgang Quint

Präzisions-Massenmessungen von Neonisotopen an THE-Trap – ZUSAMMENFASSUNG

THE-Trap ist ein Penningfallen Experiment zur Präzisionsmassenbestimmung am Max-Planck-Institut für Kernphysik in Heidelberg, Deutschland. Für das Datenerfassungssystem wurden ein neues Python-Programm und eine neue PHP-Website entwickelt. Unter Verwendung eines Lock-In Amplifiers wurde ein neues Locksystem implementiert. Ein Gaseintrittssystem wurde entwickelt und verwendet, um die hochgeladenen Neon-Isotope $^{20}\text{Ne}^{8+}$ und $^{22}\text{Ne}^{7+}$ Neon zu erzeugen und in der Penningfalle einzufangen. Ihre Masse wurde gegen ein ^{12}C Referenzion gemessen. Die ^{20}Ne -Masse wurde mit einer relativen Messunsicherheit von $5.8 \cdot 10^{-10}$ bestimmt. Diese befindet sich innerhalb einer Standardabweichung mit dem Literaturwert mit einer Unsicherheit von $8.4 \cdot 10^{-11}$ im Einklang. Die ^{22}Ne Masse wurde mit einer relative Messunsicherheit von $7.7 \cdot 10^{-10}$ gemessen. Diese befindet sich innerhalb fünf Standardabweichungen im Vergleich zur Messunsicherheit des Literaturwerts, $8.2 \cdot 10^{-10}$. Aufgrund der langen Messdauer ist die Messunsicherheit jeweils von zeitlichen Variationen des Magnetfelds limitiert. Das leichte Edelgas Neon gehört zum "Backbone of the Atomic Mass Evaluation", weshalb es als Bezugsmasse nützlich ist. Die Verbesserung der relativen Neonmessunsicherheit kann also die relative Messunsicherheit von Messungen verbessern, die Neon als Bezugsmasse verwenden.

Mass Measurements of Neon Isotopes at THE-Trap - ABSTRACT

THE-Trap is a Penning-trap experiment for precision mass measurements located at the Max Planck Institute for Nuclear Physics in Heidelberg, Germany. A new python program and PHP website were created for the data acquisition system and a new lock system was developed using a Lock-In Amplifier. A gas injection system was developed and used for injecting and trapping neon isotopes $^{20}\text{Ne}^{8+}$ and $^{22}\text{Ne}^{7+}$. Their masses were then measured with the use of $^{12}\text{C}^{4+}$ as reference ions. The ^{20}Ne mass was measured with a relative uncertainty of $5.8 \cdot 10^{-10}$ and is within one standard deviation in comparison to the literature value, which has a relative uncertainty of $8.4 \cdot 10^{-11}$. The ^{22}Ne mass was measured with a relative uncertainty of $7.7 \cdot 10^{-10}$ and is at a discrepancy of five standard deviations in comparison to the literature value, which has a relative uncertainty of $8.2 \cdot 10^{-10}$. The relative uncertainties of both measurements are limited by temporal variations of the magnetic field due to the long measurement times. Being a light noble gas, neon is a part of the "Backbone of the Atomic Mass Evaluation", such that it is useful as a reference mass. Improving the mass uncertainty of neon can therefore improve the uncertainty of measurements using it as a reference.

“The ability to observe without evaluating is the highest form of intelligence.”
- Jiddu Krishnamurti

“We miss the real by lack of attention and create the unreal by excess of imagination.”
- Nisargadatta Maharaj

CONTENTS

1	MOTIVATION	1
1.1	The Neutrino Mass	1
1.2	The Atomic Mass Evaluation (AME)	4
1.3	Neon Masses	4
1.4	Thesis Layout	5
2	PENNING-TRAP THEORY	7
2.1	Charged Particle Motion in a Penning-Trap	7
2.2	Penning-Trap Geometry	9
2.3	Measurement of the Trapped Particle's Signal	11
2.3.1	Description of The Image Current	12
2.3.2	Detection of the Image Current	12
2.3.3	The Driven Penning-Trap as a Driven Series RLC Circuit	14
2.3.4	The Detailed Detection Circuit	16
2.4	Expansion of the Electrostatic Potential	18
2.5	Excitations and Couplings	20
2.5.1	Drive signals	20
2.5.2	Coupling Signals	21
2.6	Systematic Shifts	22
2.6.1	Electric Field Shifts	22
2.6.2	Magnetic Field Shift - B_2	25
2.6.3	Mixed Shift - $C_1 B_1$	26
2.6.4	THE-Trap Shifts	26
3	THE EXPERIMENTAL SETUP	29
3.1	The Magnet	29
3.1.1	The Repair of the Magnet	32
3.1.2	Shimming the Magnet	32
3.1.3	Shielding Factor Measurements	33
3.2	The Trap Tower	34
3.2.1	The Gas Inlet System	34
3.3	The Stabilization System	34
3.3.1	New Data Acquisition Program - "PyEnvDAQ"	38
3.3.2	New Group Website - "THE-Website"	38
3.4	Loading and Manipulating Ions	38
3.4.1	Locking and detecting the Axial Mode	38
3.4.2	Detecting the Radial Modes	43
4	NEON MASS MEASUREMENTS	47
4.1	Loading a Single Ion	47

4.2	Pulsing the radial modes to roughly determine the Ion Frequencies	48
4.3	Lock Phase Calibration and Locking the Ion	48
4.4	Aligning the Trap	49
4.5	Radial and Axial Calibration Measurements	50
4.6	Magnetron and Modified Cyclotron Calibration Measurements	50
4.7	Axial Calibration Measurements	54
4.8	The Measurement Method - "Sweeps"	56
4.9	Calculating the Systematic Shifts	60
4.10	Data Analysis	61
4.11	Results	61
4.11.1	The $^{20}\text{Ne}^{8+}$ Measurement	62
4.11.2	The $^{22}\text{Ne}^{7+}$ Measurement	62
5	CONCLUDING REMARKS	63
A	APPENDIX	65
A.1	THE-Trap Parameters	65
A.2	Expansion of the Electrostatic Potential	66
A.3	Driving and Coupling the Modes	67
A.4	Systematic Shifts - Formulas not used in the Thesis	68
A.4.1	The $C_{\text{total}4}$ and $C_{\text{total}6}$ Shifts	68
A.4.2	Image Charge Shift	68
A.4.3	Trap Tilt	68
A.4.4	Magnetic Field Shift - B_2	69
	Bibliography	71
B	ACKNOWLEDGMENTS	79

LIST OF FIGURES

Figure 1.1	The kinetic energy spectrum of the electron emitted in the β -decay of tritium.	2
Figure 1.2	Relative uncertainties of the Q -value of the Tritium-He beta decay as a function of time.	3
Figure 1.3	Discrepancy between measurements of light ion masses.	4
Figure 2.1	The trajectory of a charged particle in a Penning-trap.	10
Figure 2.2	Half of a hyperbolic Penning-trap with an impedance component connected between the endcaps for image current detection.	13
Figure 2.3	The image charge created by an oscillating trapped ion in a Penning-trap is equivalent to a series LC circuit.	15
Figure 2.4	The full Penning-trap detection circuit.	16
Figure 3.1	The magnet.	30
Figure 3.2	The magnet's relative magnetic field decay rate in ppt/h.	31
Figure 3.3	The results of shimming the magnet.	33
Figure 3.4	Shielding factor measurements.	35
Figure 3.5	The trap tower and the two traps.	36
Figure 3.6	The gas inlet system.	37
Figure 3.7	The Stabilization System	39
Figure 3.8	The new data acquisition program - "PyEnvDAQ".	40
Figure 3.9	The new group website, "The-Website".	41
Figure 3.10	A ring voltage scan revealing trappable ion species in THE-Trap.	42
Figure 3.11	(a) The old axial locking circuit with the "mix2dc box". (b) the new axial locking circuit with the Lock-In Amplifier.	44
Figure 4.1	Lock Phase Calibration Measurements	49
Figure 4.2	Magnetron and Modified Cyclotron Calibration Measurements.	51
Figure 4.3	Axial Calibration Measurements.	55
Figure 4.4	The Measurement Method - "Sweeps".	58

LIST OF TABLES

Table 4.1	Calibration Measurements	57
Table 4.2	Sweep Measurements	59
Table 4.3	Systematic Shifts Results	60

Table 4.4	Neon masses measurement results	62
Table A.1	THE-Trap Parameters	65

MOTIVATION

Mass spectrometry is the measurement of atomic, nuclear and sub-nuclear masses with high precision. The Penning trap (see Section 2.1) is the best tool for such measurements [1], as relative uncertainties of $\frac{\delta m}{m} = 10^{-9}$ for short-lived radioactive nuclei [2] and 10^{-11} for long-lived and stable nuclei [3] can be reached. Precision mass measurements are used for precisely determining the values of fundamental constants such as the g-factor of different particles [4], for measurements of so-called reference masses, which are masses used as references in different experiments [5], in atomic and nuclear physics to determine nuclear structures, test strong interaction theories, the electroweak Standard Model and quantum electrodynamics [6], and for measuring or inferring upper bounds on the neutrino masses [7]. Two applications of relevance for this thesis will be introduced in more detail in the following.

1.1 THE NEUTRINO MASS

Neutrinos are electrically-neutral leptons which interact only through the weak nuclear force and are at least 100,000 times lighter than electrons [8]. They were first predicted in 1930 by Wolfgang Pauli and formulated into a theory by Enrico Fermi as an explanation for the observed energy spectrum of the electrons e^- emitted in the beta-minus decay of neutrons, which corresponded to that of a three-body problem and not to that of a two-body problem as expected. This is due to the presence of the neutrino, which was not yet observed at that time [9]. There are three neutrino types, also referred to as generations - the electron, tau and muon neutrinos, or six with the anti-neutrinos included. The electron anti-neutrino was first observed in 1956 in the “Cowan-Reines Neutrino Experiment” as a part of the reaction of inverse beta decay in a nuclear reactor $\bar{\nu}_e + p \rightarrow e^+ + n$, where $\bar{\nu}_e$, p , e^+ and n stand for the electron anti-neutrino, the proton, the positron and the neutron, respectively [10]. The muon neutrino was observed in 1962 by observing the decay of a pion beam into muons and neutrinos [11]. The tau neutrino was observed in 2000 as a product of the decay of D_s mesons, which were created using a proton beam shooting on a tungsten target [12]. Neutrinos have been observed to oscillate between one another, suggesting both that neutrinos are not massless, and that the three neutrino types are not mass-eigenstates but superpositions of them, as assumed in the Standard Model [13, 14]. The Nobel prize was awarded to Takaaki Kajita and Arthur B. McDonald in 2015 for this discovery [15]. The squared mass difference of neutrino types can be measured from neutrino oscillations, but not the individual masses. The sum of the three neutrino masses is assumed to be at most $0.39 \frac{\text{eV}}{c^2}$ based on cosmic microwave background observations [16] and $0.2 \frac{\text{eV}}{c^2}$ based on an estimate of the influence of neutrinos on nucleon-synthesis following the Big Bang [17, 18]. An overview of such estimates can be found

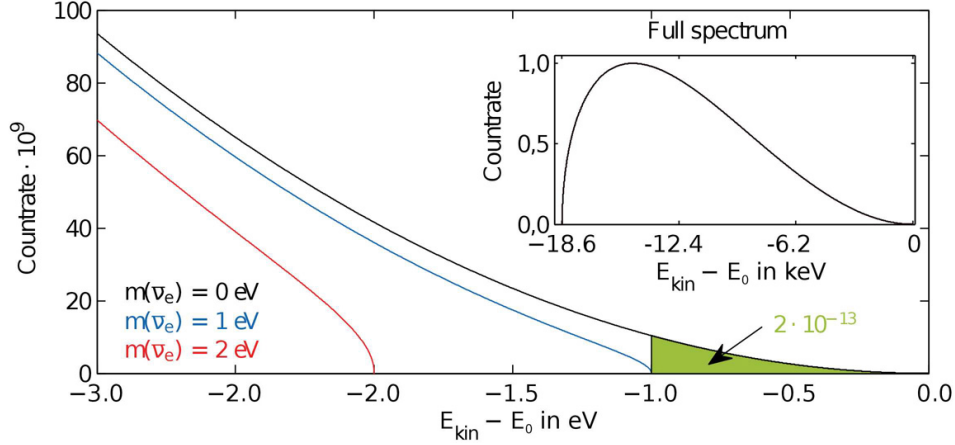


Figure 1.1: The kinetic energy spectrum of the electron emitted in the β -decay of tritium. E_0 is the kinetic energy in case neutrinos are massless, as in $m(\bar{\nu}_e) = 0$. It is also taken into account that the non-finite neutrino mass does not only shift the end-point but also changes the shape of the spectrum proportionally to $m(\bar{\nu}_e)$. Only $2 \cdot 10^{-13}$ of the electrons are emitted in the energy window $E_0 - 1 \text{ eV}$ to E_0 .

in [19]. The upper bound for the mass of the heaviest anti-neutrino, the electron anti-neutrino, was measured to be $m(\bar{\nu}_e) < 2.3 \frac{\text{eV}}{c^2}$ and later refined to be $m(\bar{\nu}_e) < 2.05 \frac{\text{eV}}{c^2}$ [8, 20].

The Karlsruhe Tritium Neutrino Experiment, KATRIN, intends to measure or provide an upper bound of around $m(\bar{\nu}_e) < 0.2 \frac{\text{eV}}{c^2}$ for the electron anti-neutrino mass by measuring the end-point of the energy spectrum of the electrons released in the tritium beta minus decay $T \rightarrow {}^3\text{He} + e + \bar{\nu}_e$. Here T and ${}^3\text{He}$ stand for tritium and for the rare stable helium isotope, respectively. Near the end-point the electrons carry a minimal amount of kinetic energy, such that the difference between the measured energy and the Q -value of about 18.6 keV [21] corresponds to the neutrino's rest mass, see Figures 1.1 and 1.2. The measured energy is given by $E = (m(T) - m({}^3\text{He}) - m(\bar{\nu}_e)) c^2 - E_{\text{EBE}} - E_{\text{REC}}$, where the m 's are the masses of tritium, ${}^3\text{He}$ and the electron anti-neutrino, respectively, E_{EBE} is the electron binding energy and E_{REC} is the ${}^3\text{He}$ recoil energy¹. Calibration of the end-point with its low count rate is technically challenging [7], with a projected uncertainty of 40 meV [23]. Independent measurements are important for testing systematic shifts. The current leading measurements have uncertainties of $1.2 \frac{\text{eV}}{c^2}$ [24] and $70 \frac{\text{meV}}{c^2}$ [25] and differ by two standard deviations.

¹ In the mass spectrometry community, the Q -value is defined as the difference between the masses of the mother and daughter nuclei, $E = (m(\text{mother}) - m(\text{daughter})) c^2$. However, in the β -spectrometry community, the binding energy of the daughter's missing electron E_{EBE} , the daughter's recoil energy E_{REC} , calculated from kinematics [22] and the electron anti-neutrino's mass $m(\bar{\nu}_e)$ are all taken into account.

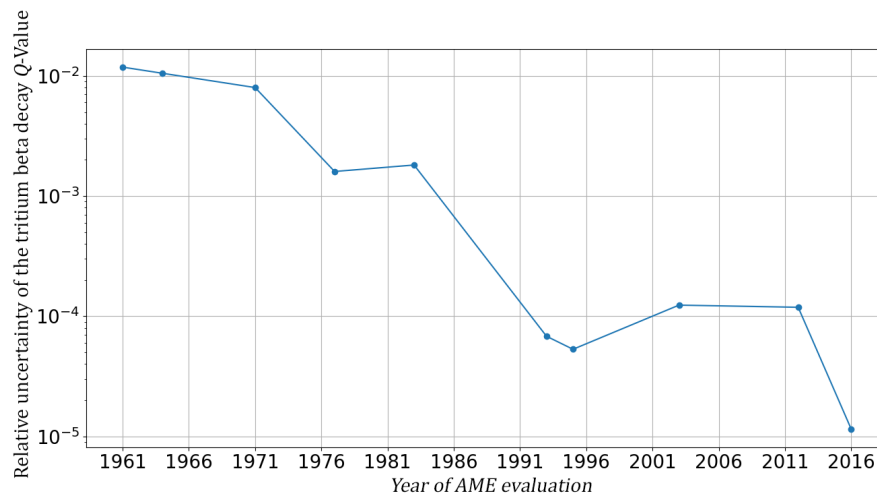


Figure 1.2: Relative uncertainties of the Q -value of the ${}^3\text{T} \rightarrow {}^3\text{He} \beta$ -decay as a function of time gathered from the Atomic Mass Evaluation (AME) [5] by [26]. It can be seen that the relative uncertainties gradually decrease due to innovations and improvements in the measurement method. For instance, in 1989 single ion trapping was achieved and two measurement techniques were implemented: continuous axial detection [27] and “Pulse and Phase” [28]. In 2016 two ions filtered from an injected molecular beam were stored simultaneously in the same trap with the “parking” method and measured with the “Pulse and Phase” method [25]. Note that the data points correspond to the AME evaluation dates and not necessarily to the dates of the experiments.

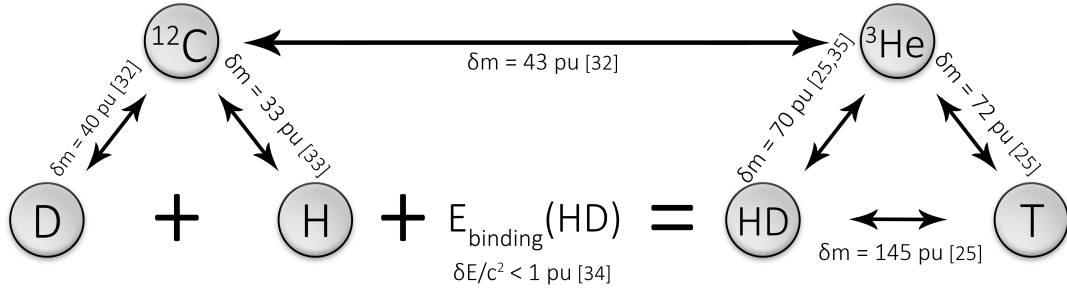


Figure 1.3: Discrepancy between measurements of light ion masses. The HD mass can either be calculated using the $^{12}\text{C} \leftrightarrow \text{D}$ [31] and $^{12}\text{C} \leftrightarrow \text{H}$ [32] links combined with the binding energy of HD [33], or by using the $^{12}\text{C} \leftrightarrow ^3\text{He}$ link [31] and either the $^3\text{He} \leftrightarrow \text{HD}$ link [34, 25] or the $^3\text{He} \leftrightarrow \text{T}$ and $\text{T} \leftrightarrow \text{HD}$ links [25]. A five standard deviations discrepancy is revealed by applying all of the links. Based on Figure 1 from [35].

1.2 THE ATOMIC MASS EVALUATION (AME)

The AME is a project started in 1970 for gathering values for the atomic masses of all known nuclei at that time from measurements done by different groups around the world using mass spectrometers and radioactive decay energy measurements [29, 30]. The precise values of atomic masses play an important role in many fields of physics and chemistry, making the AME one of the most cited publications in atomic and nuclear physics and in chemistry. A group of precisely-measured, relatively easily-obtainable ions is used as reference masses in mass measurements and for systematic checks of various experiments and is thus referred to as the “backbone” of the AME. Members of this “backbone” are among others, the stable neon isotopes $^{20,22}\text{Ne}$.

1.3 NEON MASSES

There is a five standard deviations discrepancy between measurements of light ion masses [35], see Figure 1.3. This discrepancy motivated a precision mass measurement of ^3He . A gas inlet system (see 3.2.1) was implemented in preparation for the measurement and neon gas was used to test this system. Following the successful test, it was decided to perform neon mass measurements, as neon is a part of the “backbone of the AME”, being a readily-available noble gas. In this thesis the masses of $^{20}\text{Ne}^{8+}$ and $^{22}\text{Ne}^{7+}$ were measured with the use of $^{12}\text{C}^{4+}$ as a reference ion. The measurement method, results and the concluding remarks are presented in the rest of the thesis.

1.4 THESIS LAYOUT

In Chapter 2 the theoretical background required for understanding the experiment is explained: Penning-trap theory and the physics of the detection circuit.

In Chapter 3 the experimental setup is described: The magnet including the shielding factor measurements, the trap tower including the gas inlet system, the LHe pressure and level stabilization system including the new python control program and the new php website for plotting the recorded data, the field emission point for loading ions and the detection and manipulation of ions.

In Chapter 4 the neon mass measurements are presented: The measurement process, loading a single ion, calibration measurements, the sweeps measurement method and results.

In Chapter 5 concluding remarks regarding the experiment are given.

PENNING-TRAP THEORY

A Penning-trap is a device for storing charged particles. The radial trapping is done by a static homogeneous magnetic field and the axial trapping by a static quadrupolar electric field. Fundamental properties of the trapped ion, such as its mass, binding energies and magnetic moment or g-factor can then be determined by measuring the ion's frequencies of motion in the trap. A quantum description for the motion exists [36], but due to the high quantum numbers of the stored ion used within the experiment carried out here, the motion can be described classically, which is easier to intuitively grasp and to numerically simulate [37, 38]. In this chapter, the motion of the charged particle is described classically with its resulting frequencies followed by a description of the trap geometry in Section 2.2. In Section 2.3 the detection circuit for detecting the trapped ion's signal is explained. In Section 2.4 the electrostatic potential of the Penning-trap is given a more detailed treatment, which is necessary for the remaining sections. In Section 2.5 excitation and coupling signals are explained, and in Section 2.6 a list of all known shifts and their formulas is provided.

2.1 CHARGED PARTICLE MOTION IN A PENNING-TRAP

A charged particle in a static homogeneous magnetic field parallel to the z direction, $\vec{B} = B\hat{z}$, experiences a Lorentz force. Substitution into the equation of motion yields

$$q \begin{pmatrix} v_y B \\ -v_x B \\ 0 \end{pmatrix} = m \begin{pmatrix} \dot{v}_x \\ \dot{v}_y \\ \dot{v}_z \end{pmatrix}, \quad (2.1)$$

where $q = ne$, m and n are the trapped particle's charge, mass and charge number, with e being the elementary charge. The solutions for the x and y directions is a harmonic motion perpendicular to the magnetic field lines with the cyclotron frequency¹

$$\omega_c = \frac{qB}{m}, \quad (2.2)$$

where the index c stands for cyclotron. For the z direction it is obtained that $v_z = \text{const}$, such that the particle's motion is bound in the x - y plane but unbound in the z direction. To achieve

¹ ω is usually called the angular frequency ($\omega = 2\pi f$, $[\omega] = \frac{\text{rad}}{\text{s}}$), where f is the frequency ($[f] = \text{Hz}$), however in this thesis it is referred to simply as "frequency".

trapping in the z direction as well, a electrostatic potential is added. One could naively expect a potential such as $\phi = 0.5\phi_2 z^2$ to be sufficient, where ϕ_2 is the potential strength parameter². However, this potential does not satisfy Laplace's equation $\Delta\phi = 0$. To satisfy it, the potential is modified to be $\phi = 0.5\phi_2 (z^2 - 0.5\rho^2) + \text{const}$, where $\text{const} \equiv 0$, such that the electric field is given by $\vec{E} = \frac{\phi_2}{2} (\vec{x} + \vec{y} - 2\vec{z})$. However, the additional terms modify the motion in the x - y plane. The motion in the z direction is still that of an harmonic oscillator with the following motion and frequency:

$$z = A_z \cos(\omega_z t + \varphi_z), \omega_z = \sqrt{\frac{q\phi_2}{m}}, \quad (2.3)$$

where A_z is a real number denoting the amplitude of the motion in the z direction and φ_z denotes the phase at time $t = 0$. For the motion to be stable, the frequency must be real and greater than zero such that $q\phi_2 > 0$. This shows that in a Penning-trap, all simultaneously trapped charged particles must have the same charge sign. Substituting Equations (2.2), (2.3) and $u \equiv x + iy$ in Equation (2.1), multiplying the second equation of motion by i and summing both it is obtained that

$$-\ddot{u} + -i\omega_c \dot{u} + \frac{\omega_z^2}{2} u = 0. \quad (2.4)$$

The solution is a superposition of two harmonic motions $u = u_+ e^{-i\omega_+ t} + u_- e^{-i\omega_- t}$ with frequencies satisfying $\omega^2 - \omega_c \omega + \frac{\omega_z^2}{2} = 0$, such that:

$$\omega_{\pm} = \frac{\omega_c \pm \sqrt{\omega_c^2 - 2\omega_z^2}}{2}, \quad (2.5)$$

where ω_+ is called the modified cyclotron frequency and ω_- the magnetron frequency. For typical Penning-trap parameters it holds that $\omega_c > \omega_+ \gg \omega_z \gg \omega_-$. For completion, using Euler's equation, the real part of u is taken to be the motion in the x direction and the imaginary part is taken to be the motion in the y direction, such that:

$$x = A_+ \cos(\omega_+ t + \varphi_+) + A_- \cos(\omega_- t + \varphi_-), \quad (2.6)$$

$$y = -A_+ \sin(\omega_+ t + \varphi_+) - A_- \sin(\omega_- t + \varphi_-), \quad (2.7)$$

where A_{\pm} are real numbers denoting the amplitudes of the motion in the x and y directions, respectively, and φ_{\pm} their phases at time $t = 0$.

² The potential strength parameter is defined as ϕ_2 because in the expansion of the potential shown in Section 2.4 it is the coefficient of the harmonic term in the expansion, the one proportional to the squares of the coordinates.

Previously with $E = 0$ the charged particle was performing a simple circular motion in the x-y plane. Now with $E \neq 0$ and $\vec{E} \perp \vec{B}$, the charged particle accelerates during one half of each cyclotron cycle, where $\vec{E} \cdot \vec{v} > 0$, and decelerates during the other, where $\vec{E} \cdot \vec{v} < 0$, such that the center of the cyclotron motion “drifts” orthogonally to both \vec{E} and \vec{B} . This effect, called the $\vec{E} \times \vec{B}$ drift, creates a second, slow oscillation called the magnetron motion ω_- , superimposed on a “cyclotron motion” with a slightly reduced frequency, called the modified cyclotron motion ω_+ , see Figure 2.1. For the solutions to be harmonic the frequencies need to be real $\omega_c^2 - 2\omega_z^2 \geq 0$, and for them to be unique they need to be distinct $\omega_c^2 - 2\omega_z^2 > 0$, such that $\omega_c^2 > 2\omega_z^2$ needs to be satisfied. Substitution yields $B > \sqrt{2\frac{m}{q}\phi_0}$. The following relations hold:

$$\omega_c^2 = \omega_-^2 + \omega_z^2 + \omega_+^2, \quad (2.8)$$

$$\omega_c = \omega_+ + \omega_-, \quad (2.9)$$

$$\omega_z^2 = 2\omega_+\omega_-. \quad (2.10)$$

Equation (2.8) is called the Brown-Gabrielse invariance theorem [36] and is useful for calculating the cyclotron frequency even in the presence of certain systematic shifts, see Section 2.6. Equation (2.9) is called the sideband frequency equation and Equation (2.10) is useful for roughly calculating ω_- after ω_+ has been calculated, see 4.2. The charged particle’s mass can be determined as follows: The cyclotron frequency ω_c can be measured for two ions in the same trap, under the influence of the same magnetic field \vec{B} . The ratio $(q_1/m_1)/(q_2/m_2)$ can be obtained from the ratio ω_{c1}/ω_{c2} because B cancels out. Since the charges are known, the mass ratio between the two ions is obtained. If one of the ions has a well-known mass, for instance $^{12}\text{C}^{4+}$, the mass of the other ion can be calculated. Taking the masses and binding energies of the missing electrons into account, the mass of the atom can be calculated from that of the ion.

2.2 PENNING-TRAP GEOMETRY

As was shown in Section 2.1, the equipotential surfaces are in the shape of hyperboloids of revolution. To achieve this potential hyperbolic electrodes are used³, called the top endcap, the ring, the bottom endcap and the correction electrodes, see Figure 2.2. The endcap electrode surfaces are given by $z^2 - 0.5\rho^2 = h_{\text{ec}}^2$, where h_{ec} is the distance between the trap center to one of the endcaps. The ring electrode surface is given by $z^2 - 0.5\rho^2 = -0.5\rho_{\text{ring}}^2$, where ρ_{ring} is the

³ Apart from the hyperbolic Penning-traps shown in this thesis, there are also cylindrical ones [40]. It is easier to inject into and transfer ions between cylindrical traps, as precisely manufacturing and aligning injection/transfer holes for stacked hyperbolic Penning-traps is challenging.

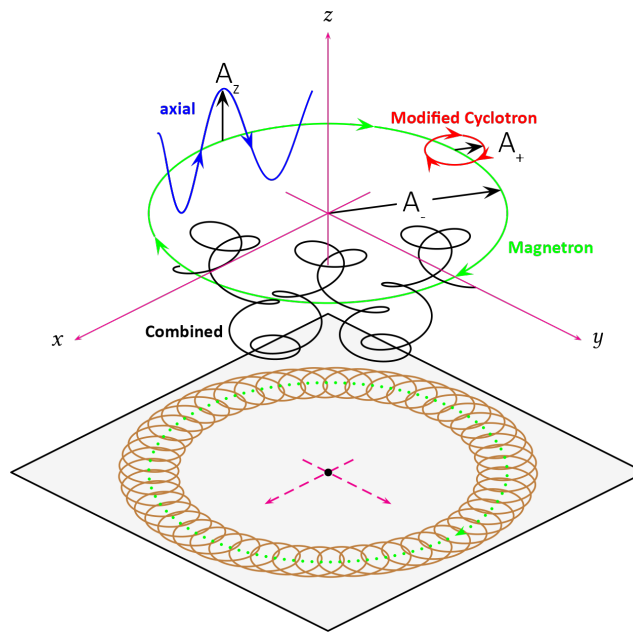


Figure 2.1: The trajectory of a charged particle in a Penning-trap (black), as well as the separate three trajectories that compose it - that of the modified cyclotron motion (red), of the axial motion (blue) and of the magnetron motion (green). The projection on the x - y plane shows the effect of the combined modified cyclotron and magnetron motions - a fast oscillation superimposed on a slow one. The green dots show the magnetron radius. The frequencies are drawn with a ratio of $\omega_+/\omega_z = 50$, $\omega_z/\omega_- = 10$. Based on Figure 2.2 from [39].

distance between the trap center and the ring electrode. The voltage V_0 between any point on the endcap and any point on the ring is given by their potential differences

$$V_0 \equiv \phi_{\text{endcap}} - \phi_{\text{ring}} = \phi_2 \left(\frac{1}{2} \left(h_{\text{ec}}^2 + \frac{\rho_{\text{ring}}^2}{2} \right) \right), \quad (2.11)$$

where the characteristic dimension of the Penning-trap is defined as

$$d \equiv \sqrt{\frac{1}{2} \left(h_{\text{ec}}^2 + \frac{\rho_{\text{ring}}^2}{2} \right)}. \quad (2.12)$$

Substitution of Equation (2.12) in Equation (2.11) yields:

$$\phi_2 = \frac{V_0}{d^2}. \quad (2.13)$$

Substitution allows the axial frequency, the electrostatic potential and the electrostatic field to be represented using trap parameters instead of by using ϕ_2 :

$$\omega_z = \sqrt{\frac{qV_0}{md^2}}, \quad (2.14)$$

$$\phi = \frac{m\omega_z^2}{2q} \left(-\frac{\rho^2}{2} + z^2 \right), \quad (2.15)$$

$$\vec{E} = \frac{m\omega_z^2}{2q} (\vec{x} + \vec{y} - 2\vec{z}). \quad (2.16)$$

The upper limit for the voltage is given by substitution of Equation (2.13) in the threshold for B : $V_0 < qd^2B^2/2m$. This is called the stability limit.

2.3 MEASUREMENT OF THE TRAPPED PARTICLE'S SIGNAL

As explained in Section 2.1, to measure the trapped particle's mass it is required to measure its frequencies of motion ω_{\pm} and ω_z . There are two types of measurement techniques, destructive [42, 41, 43] and non-destructive [44], where the ions are either lost after detection or remaining trapped, respectively. The measurements described in this thesis utilize the latter, and therefore it is the non-destructive measurement method which will be next expanded upon.

2.3.1 Description of The Image Current

The moving trapped ion creates a moving image charge - an image current - on the trap electrodes. In the case of THe-Trap, it is the upper endcap electrode which is used for the image current detection. The image current is given by [45]

$$I = q\vec{z} \cdot \frac{\vec{E}}{V_{\text{UE}}}, \quad (2.17)$$

where \vec{z} is the ion's velocity and \vec{E} is the electric field present when the upper endcap is held at potential V_{UE} , which is calculable numerically. The electric field caused by the endcaps can be approximated by the electric field of a pair of infinite plane capacitors [46] :

$$\vec{E} = -\frac{V_{\text{UE}}}{D}\hat{z}, \quad D \equiv \frac{2z_0}{\kappa}, \quad (2.18)$$

where D is the effective distance between the capacitor planes, $2z_0$ is the distance between the infinite plates capacitor and κ is a scaling factor introduced to account for the fact that the endcaps are not planes but hyperboloid surfaces. κ was numerically calculated to be around $\kappa \approx 0.8$ for THe-Trap⁴ [47]. Substitution yields

$$I = -\frac{q}{D}\dot{z}. \quad (2.19)$$

2.3.2 Detection of the Image Current

It could be naively expected that to detect the image current, a large impedance could be connected between the end-caps, see Figure 2.2. As the positively-charged trapped ion moves upwards, it attracts negative charges in the upper endcap, creating a downwards current across the impedance. In other words, the current through the impedance is opposite in sign to that of the ion. The resulting voltage drop over the impedance is given by

$$V_{\text{UE}} = -IZ. \quad (2.20)$$

Note that it is negative as the negative charges are going into the upper endcap while the voltage across the impedance is defined by the current going out of the electrode. Equations (2.19) and (2.20) can be substituted into Equation (2.18), such that

$$\vec{E} = -\frac{q}{D^2}\dot{z}Z\hat{z}. \quad (2.21)$$

⁴ See Section A.1 for a list of THe-Trap parameters.

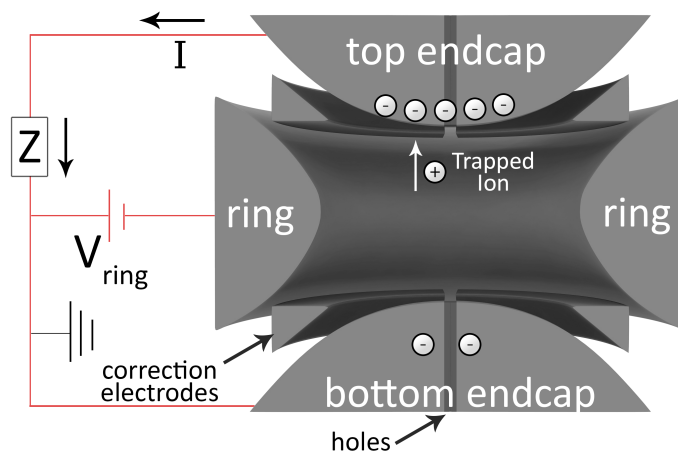


Figure 2.2: Half of a hyperbolic Penning-trap. Mirroring it around the screen or page (the plane defined by h_{ec} and ρ_{ring}) the full Penning-trap surfaces are obtained. The ring electrode is held at a voltage of V_{ring} and the endcap electrodes are held at $V_{ec} = 0$. The geometric center of the trap is at the origin. Note that a real Penning-trap deviates from this structure. In the case of THe-Trap the deviations are holes in the upper and lower endcaps for gas and electron injection, respectively (see Section 3.4), unintentional geometrical deviations due to the finite precision of the machining process (see Section 2.6) and correction electrodes for accounting for some of those (see Section 2.4). An impedance component is connected between the endcaps for image current detection. As the positively-charged trapped particle moves upwards, it attracts negative charges at the upper endcap, creating a downwards current across the impedance component, and vice versa when its going down. In other words, the current on the impedance component is opposite in sign to that of the ion.

The equation of motion in the z direction is modified to

$$\ddot{z} = -\frac{q^2 Z}{mD^2} \dot{z} - \omega_z^2 z. \quad (2.22)$$

In the case where $Z \in \Re$ the equation of motion is that of a damped harmonic oscillator with a damping factor of

$$\gamma \equiv \frac{q^2 Z}{mD^2}. \quad (2.23)$$

Note that $\gamma \propto q^2/m \propto N_{\text{trapped ions}}$. This allows a determination of the number of trapped ions based on a measurement of γ ⁵. A trapped ion will lose energy with a time scale of $1/\gamma$ until it reaches thermal equilibrium with the impedance, such that the energy in the z direction can be expressed by

$$E_z = E_0 e^{-\gamma t} + k_B T_Z, \quad (2.24)$$

where T_Z is the effective temperature of the impedance, in THE-Trap approximated to be 10K [48].

2.3.3 The Driven Penning-Trap as a Driven Series RLC Circuit

In Section 2.3.2 it was shown that measuring the image current can be supposedly achieved by placing an impedance between the end-caps. The larger the impedance, the larger the voltage drop across the endcaps which can then be measured. Actually, this would not work due to the existence of the parasitic capacitance in the trap. A more complicated model treats the ion as a circuit element and the entire circuit as a driven series RLC circuit representing the Penning-trap connected in parallel to a parallel LC circuit used as a detection system [38, 49]. In order to derive that, first it will be shown that in the presence of an alternating-current (AC) drive, the Penning-trap is equivalent to a driven series LC circuit. For a driven LC circuit, the drive can be seen as connected in parallel to the inductor L and the capacitor C , such that their voltages are equal:

$$V_{\text{drive}} = V_L + V_C. \quad (2.25)$$

⁵ The number of trapped ions can actually only be precisely calculated with this equation if all of them are of the same species. However, even if they are not, it can still be used to show that there are multiple ions and that further manipulations are required in order to reduce the amount of ions to one, such that it is useful either way.

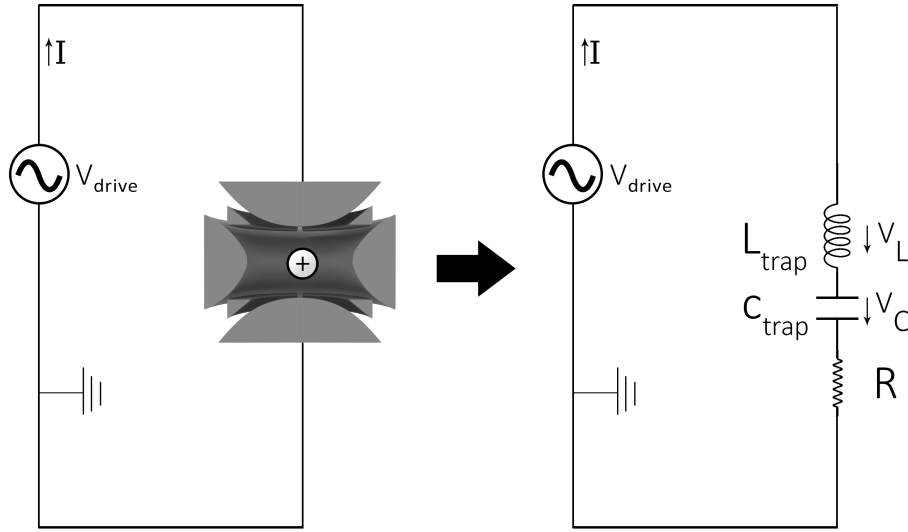


Figure 2.3: The image charge created by an oscillating trapped ion in a Penning-trap is equivalent to a series LC circuit. In reality the components are lossy, which is represented in the figure by the resistance component.

The voltage across an inductor is given by $V_L = \dot{I}L$ and the voltage across a capacitor is given by $V_C = \frac{1}{C} \int I dt$. Substitution into Equation (2.25) and derivation with respect to time yields

$$\dot{V}_{\text{drive}} = \ddot{I}L + \frac{1}{C}I. \quad (2.26)$$

Similarly to Equation (2.18), the electric field can be expressed by the voltage drop across the Penning-trap:

$$\vec{E} = -\frac{V_{\text{drive}}}{D}\hat{z}. \quad (2.27)$$

Through substitution of Equation (2.27) in the equation of motion along with Equation (2.21) for the electric field induced by the image charge, it is obtained that

$$\ddot{z} = -\frac{q}{mD}V_{\text{drive}} - \omega_z^2 z. \quad (2.28)$$

Substitution of Equation (2.19) and its time derivative into the time derivative of Equation (2.28) yields

$$\dot{V}_{\text{drive}} = \frac{mD^2}{q^2}\ddot{I} + \frac{mD^2\omega_z^2}{q^2}I. \quad (2.29)$$

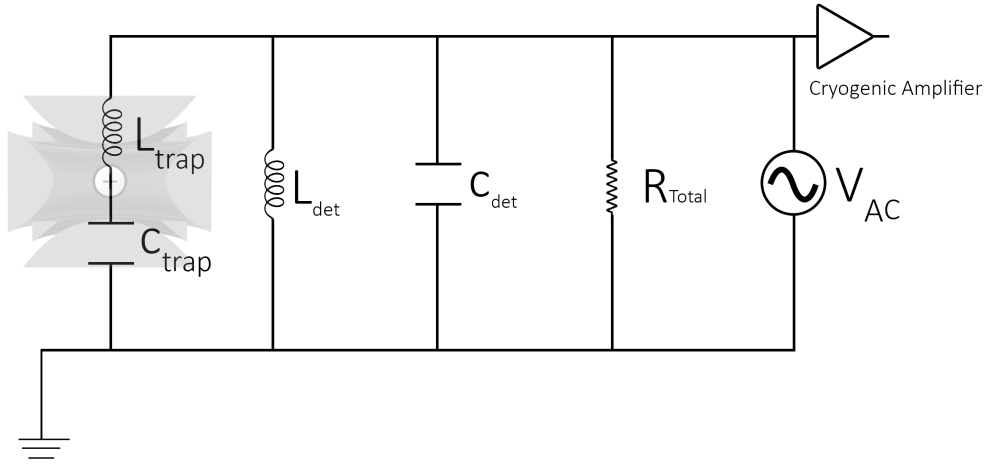


Figure 2.4: The full Penning-trap detection circuit - a series LC circuit representing the Penning-trap (L_{trap} and C_{trap}), connected in parallel to a parallel RLC circuit for detection (R_{total} , $L_{\text{detection}}$, $C_{\text{detection}}$), including an AC drive and a cryogenic amplifier. For details see Section 2.3.4.

Comparison with Equation (2.26) shows that the two circuits are physically equivalent, such that an axially-driven trapped ion in a Penning-trap is equivalent to a driven LC circuit (see Figure 2.3), specifically with the following inductance and capacitance:

$$L = \frac{mD^2}{q^2}, \quad C = \frac{1}{L\omega_z^2} \quad (2.30)$$

Actually, C and L are both lossy, such that their impedance has a real component. These can be combined to be represented by a resistive component in parallel to both L and C , such that the Penning-trap is equivalent to a parallel RLC circuit, see Figure 2.3.

2.3.4 The Detailed Detection Circuit

In the case of THe-Trap, the total capacitance of the circuit is around $C_{\text{total}} \approx 20$ pF [50] and $f_z \approx 4$ MHz, such that the resistance of the capacitance is $R_C = 1/\omega C \approx 2$ k Ω . However, the minimal detectable voltages in the experimental setup are around $V \approx 1$ nV, and the image current is approximately $I \approx 1$ fA. Therefore, the minimal required resistance is $R \approx 1$ M Ω . However, if such a resistance would be connected, it would be connected in parallel to the 2 k Ω of the capacitance, which is far smaller and will thus shorten the image current, leaving no detectable image current on the 1 M Ω resistor. To overcome that, an inductor L_{det} is added. The total resistance of the circuit is

$$R_{\text{total}} = \frac{R_L R_C}{R_L + R_C} = \frac{L}{C \left(\omega L + \frac{1}{\omega C} \right)}. \quad (2.31)$$

Likewise, C_{trap} and C_{det} , the parasitic capacitance of the detection system, are combined into C_{total} . Together with L_{det} , the three components form a parallel RLC circuit, see Figure 2.4. The impedance of the circuit is given by

$$\frac{1}{Z_{\text{total}}} = \frac{1}{R_{\text{total}}} + \frac{1}{Z_{L_{\text{det}}}} + \frac{1}{Z_{C_{\text{total}}}} = \frac{1}{R_{\text{total}}} + i \left(\omega C_{\text{total}} - \frac{1}{\omega L_{\text{det}}} \right), \quad (2.32)$$

such that

$$|Z_{\text{total}}| = \sqrt{\frac{1}{\frac{1}{R_{\text{total}}^2} + \left(\omega C_{\text{total}} - \frac{1}{\omega L_{\text{det}}} \right)^2}}. \quad (2.33)$$

The impedance is maximal when the denominator is minimal, as in for the resonance frequency

$$\omega_{\text{detection}} = \sqrt{\frac{1}{C_{\text{total}} L_{\text{det}}}}. \quad (2.34)$$

For this frequency, the contributions of the capacitance and the inductance to the impedance cancel out, leaving only the contribution of the resistive component, such that $Z_{\text{total}}(\omega = \omega_{\text{det}}) \in \Re$. Near this frequency, $|Z_{\text{total}}|^2$ can be approximated to be a Lorentzian with a maximum value of R_{total}^2 centered around ω_{det} with a full-width of half-maximum (FWHM) of

$$\text{FWHM} = \frac{1}{R_{\text{total}} C_{\text{total}}}, \quad (2.35)$$

such that the total impedance is approximated to be

$$|Z_{\text{total}}|^2 \approx \frac{R_{\text{total}}^2}{1 + (2R_{\text{total}} C)^2 (\omega_{\text{det}} - \omega)^2}. \quad (2.36)$$

The ratio between the resonance frequency and the FWHM for $\omega = \omega_{\text{det}}$ is called the Q factor. Substitution of Equations (2.34) and (2.35) shows that the Q factor is given by:

$$Q \equiv \frac{\omega_{\text{det}}}{\text{FWHM}} = \frac{1}{\left(\omega_{\text{det}} L_{\text{det}} + \frac{1}{\omega_{\text{det}} C_{\text{total}}} \right)} \sqrt{\frac{L_{\text{det}}}{C_{\text{total}}}}. \quad (2.37)$$

The Q factor allows calculation of the time constant for dissipation of energy in the circuit:

$$\tau \equiv \frac{Q}{\omega_{\text{det}}} = \frac{L_{\text{total}}}{\left(\omega_{\text{det}}L_{\text{total}} + \frac{1}{\omega_{\text{det}}C_{\text{total}}}\right)}. \quad (2.38)$$

At THE-Trap, $\omega_z \approx 2 \cdot \pi \cdot 4 \cdot 10^6$ Hz and the Q factor for ω_z is measured to be around $Q \approx 800$, with the time constant $\tau \approx 20$ ms. Both were measured by using a spectrum analyzer. It is also possible to measure R_{total} by measuring L using an RLC meter and then substituting Equation (2.35) in Equation (2.37). A full treatment of the circuit, as in of a series LC circuit connected in parallel to a parallel RLC circuit, instead of just a parallel RLC circuit, shows [38, 51] that at the limit where $\gamma \ll \text{FWHM}$ the full damping term changes from Equation (2.23) to:

$$\gamma = \frac{q^2 Z}{mD^2} \frac{1}{1 + \left(\frac{2(\omega - \omega_{\text{det}})}{\text{FWHM}}\right)^2}. \quad (2.39)$$

Note that $\gamma \propto \frac{q^2}{m}$ still holds. There is an as-of-yet unexplained discrepancy between the measured and the calculated damping terms for hyperbolic Penning-trap experiments where the calculated damping term is lower by factors of between 4/5 and two than the calculated γ . In the case of THE-Trap it is about 0.7γ [36, 46, 50]. The same full treatment also shows a shift of the resonance frequency which is negligible in the case of THE-Trap.

2.4 EXPANSION OF THE ELECTROSTATIC POTENTIAL

For the next sections the electrostatic potential needs to be discussed in more detail. In this section it is represented by a series expansion, with individual contributions from the different electrodes of the trap.

The electrostatic potential for a charge-free region inside the equipotential surfaces of the Penning-trap can be described by a series expansion using Laplace's spherical harmonics $Y_{l,m}(\theta, \varphi)$ multiplied by r^l . These terms form a complete orthogonal set which satisfy Laplace's equation. The terms are complex, but by using specific linear combinations they can be made real. For instance, by setting all coefficients of $r^l Y_{l,m}$ to one and taking the imaginary part of $r^l Y_{l,m}$ in case m is positive and the real part otherwise, real terms are obtained, see Section A.2. In cartesian coordinates, these functions are homogeneous polynomials of degree l and are called the harmonic polynomials [52, 53, 54]. Using these harmonic polynomials the potential can be expressed by

$$\phi = \sum_{l=0}^{\infty} \left(\sum_{m=-l}^0 C_{l,m} r^l \Re(Y_{l,m}) + \sum_{m=0}^l C_{l,m} r^l \Im(Y_{l,m}) \right), \quad (2.40)$$

where $C_{l,m}$ are coefficients which can be calculated numerically or experimentally determined as explained in Section 4.5. The total potential is the sum of contributions from the different electrodes, such that $C_{l,m} \rightarrow (C_{R,l,m} + C_{UE,l,m} + C_{LE,l,m})$, where R, UE and LE stand for ring, upper endcap and lower endcap⁶. Since both endcaps are grounded, their contribution is zero such that $C_{UE,l,m} = C_{LE,l,m} = 0$. For an harmonic potential of an ideal Penning-trap only $r^2 Y_{2,0} = 2z^2 - x^2 - y^2$ contributes, such that

$$C_{l,m} = \begin{cases} \frac{m\omega_z^2}{2q} & l = 2, m = 0 \\ 0 & \text{otherwise} \end{cases}, \quad \omega_z = \sqrt{\frac{2qC_{2,0}}{m}}. \quad (2.41)$$

In reality, deviations such as the ones listed in Section 2.6 add additional terms, with the most significant ones being $C_{4,0}$ and $C_{6,0}$ ⁷. To make the real Penning-trap closer to the ideal one additional electrodes are added, called the ‘‘correction electrodes’’ or the ‘‘guard electrodes’’. These are made to have a low $r^2 Y_{2,0}$ contribution but a high $r^4 Y_{4,0}$ contribution, such that by applying a specific voltage their contribution to $r^4 Y_{4,0}$ cancels that of the ring electrode, making the total $r^4 Y_{4,0}$ component zero.

The ring electrode is cylindrically symmetrical and so is the DC component of the correction electrodes, since the same DC voltage is applied to all of them. As a result, components with $m \neq 0$ or with odd l 's are negligible, such that the expression for the potential becomes

$$\phi = \sum_{l=0}^{\infty} (C_{R,2l,0} + C_{CE,2l,0}) r^{2l} \Re(Y_{2l,0}), \quad (2.42)$$

where $C_{R,l,m}$ is the coefficient of the contribution of the ring electrode to the $r^l Y_{l,m}$ term and $C_{CE,l,m}$ is that of the correction electrodes. One of the correction electrodes is also connected to an AC voltage, while the other three are AC grounded. This is relevant for Section 2.5. In order to maintain consistency with previous theses from the group [50, 47], the coefficients are redefined using $C_1 \equiv C_{R,l,0} + C_{CE,l,0}$, such that the expression for the potential becomes

$$\phi = \sum_{l=0}^{\infty} C_{2l} r^{2l} \Re(Y_{2l,0}). \quad (2.43)$$

In this convention, $C_2 = \frac{V_0}{2d^2}$ such that ω_z and C_2 can be written as:

$$\omega_z = \sqrt{\frac{2qC_2}{m}}, \quad C_2 = \frac{m\omega_z^2}{2q}. \quad (2.44)$$

⁶ Aside from the ring and the endcaps, there are also the skimmer electrodes, but their contribution is assumed to be negligible, both because they are grounded and because they are far away from the trap center.

⁷ The harmonic polynomials coupled to $C_{4,0}$ and $C_{6,0}$ are $r^4 Y_{4,0} = 35z^4 - 30z^2 r^2 + 3r^4$ and $r^6 Y_{6,0} = 231z^6 - 315z^4 r^2 + 105z^2 r^4 - 5r^6$ [52, 53, 54].

Defining V_{CE} to be the correction electrode's voltage used during the measurement and $V_{\text{CE},0}$ to be the correction electrode's voltage setting for which $C_4 = 0$, C_4 can be defined using the difference between these voltages $\Delta V_{\text{CE}} \equiv V_{\text{CE}} - V_{\text{CE},0}$ by using

$$C_4 = \Delta V_{\text{CE}} \cdot C_{\text{CE},4,0}, \quad (2.45)$$

where $C_{\text{CE},4,0}$ can be found using calibration measurements, see Section 4.5, or from simulations $C_{\text{CE},4,0} = -5.34 (36) \cdot 10^8 \text{m}^{-4}$ [47]. The same calibration measurements show that C_6 is approximately only dependent on the ring electrode voltage, such that

$$C_6 = V_0 \cdot C_{\text{R},6,0}. \quad (2.46)$$

2.5 EXCITATIONS AND COUPLINGS

The amplitude and energies of the trapped ion's modes can be increased and decreased using drive signals or swapped using coupling signals⁸, which is important for measuring the ion's frequencies and thus measuring its mass as described in Section 2.5.

2.5.1 Drive signals

Driving the Axial Mode

The axial mode can be driven by an AC signal applied to one of the endcaps at the axial frequency. Since the upper endcap is used for ion detection, the drive signal is applied to the lower endcap. The naive approach would be to set the frequency of the axial drive signal ω_{AD} to that of the axial motion $\omega_{\text{AD}} = \omega_z$. However, since the axial frequency is also the resonance frequency of the tuned circuit, applying drive signals at the axial frequency produces a signal which can be confused with the actual signal of the ion. It is for this reason that the ring voltage is modulated:

The ring electrode's voltage is changed from DC to a mixture of DC and AC: $V_{\text{R}} \rightarrow V_{\text{R}} + V_{\text{mod}} \cos(\omega_{\text{mod}} \cdot t)$, where the index mod stands for modulation. If ω_{mod} is chosen such that $\omega_z < \omega_{\text{mod}} < \text{FWHM}$, the result is that the ion's axial mode can be excited and driven by signals oscillating at the frequencies $\omega = \omega_z \pm \omega_{\text{mod}}$, also called the sideband frequencies. This can be shown by observing the equation of motion for the z direction in the presence of the modulation term, a damping term and a driving term $\vec{E}_{\text{drive}} = E_{\text{drive}} \hat{z}$:

$$\ddot{z} = - \left(\omega_z^2 + \frac{V_{\text{mod}}}{V_{\text{ring}}} \cos(\omega_{\text{mod}} \cdot t) \right) z - \gamma_z \dot{z} + \frac{q}{m} E_{\text{drive}}. \quad (2.47)$$

⁸ It is actually the action which is swapped during coupling. This means that the phases are changed in a predictable way. This can be relevant for phase-sensitive measurement methods such as Pulse and Phase (PnP) and Pulse and Amplify (PnA) [55].

Defining $\varepsilon \equiv V_{\text{mod}}/V_{\text{ring}}$ and assuming that $\varepsilon \ll 1$, it can be shown [38, 36] that the expansion of the modulation contains terms of the form $\cos(\omega_{\text{drive}} \pm \omega_{\text{mod}})$, which are resonant with the ion's motion when $\omega_{\text{drive}} = \omega_{\text{mod}} \pm \omega_z$, also called the sideband drive frequencies. The upper sideband drive frequency $\omega_{\text{mod}} + \omega_z$ is equivalent to a resonant drive with an amplitude multiplier of $\varepsilon\omega_z/4\omega_{\text{mod}}$, but only in the limit where $\varepsilon\omega_z/\omega_{\text{mod}} \ll 1$. In THe-Trap, the maximal values are $\varepsilon = 4 \cdot 10^{-4}$ and $\varepsilon\omega_z/4\omega_{\text{mod}} = 8 \cdot 10^{-3}$. The modulation shifts the ion's frequencies as explained in Section 2.6.4. The ion's axial mode is coupled to the detection circuit and is thus continuously de-energized. Therefore, in order to keep the ion's axial mode energized, the drive signal needs to be applied continuously.

Driving the Radial Modes

To drive the radial modes a field with a large $C_{1,1}$ term is required. Since the ring and the endcap electrodes have a negligible contribution to terms with odd l or non-zero m , one of the bottom correction electrodes is used instead. By applying the drive signal to just one of the four bottom correction electrodes, a field with a relatively low symmetry is produced, such that it contains many terms with odd l and non-zero m , including $C_{\text{CE AC},1,1}$ ⁹. Note that this is not $C_{\text{CE},l,m}$, which is the coefficient of the DC voltage applied on all four correction electrodes, but the coefficient of the AC voltage applied to just one of the bottom correction electrodes.

It is shown in Section A.3 that a forced harmonic oscillator has its amplitude increased by an amount proportional to the duration of the drive signal t . If the mode already has energy greater than its minimal (thermal) energy, then depending on the phase difference between the drive signal and the ion motion, the energy might be at first decreased, until it reaches its minimal (thermal) energy, at which point it will start to increase again.

Unlike the axial mode, the radial modes are not coupled to the detection circuit and are thus not de-energized "automatically".

2.5.2 Coupling Signals

In Section A.3 it is shown that it is possible to exchange the action between two modes of motion in an oscillatory manner or increase the energy in both. This is done by applying a signal with a frequency equal to the sum or the difference of the frequencies of two modes, for instance $\omega_{\text{coupling}} = \omega_z \pm \omega_{\pm}$, with an electrode containing a geometric component corresponding to both modes, for instance $C_{2,-1}$ which corresponds to $r^2Y_{2,-1} = xz$ or $C_{2,1}$ which corresponds to $r^2Y_{2,1} = yz$. Specifically, $\omega_{\text{drive}} = \omega_+ - \omega_z$ and $\omega_{\text{drive}} = \omega_z + \omega_-$ cause action exchange, also called Rabi oscillations, while $\omega_{\text{drive}} = \omega_+ + \omega_z$ and $\omega_{\text{drive}} = \omega_z - \omega_-$ cause energy increase in both modes. In "sweeps", the measurement method utilized in THe-Trap, only the former is used.

Since the axial mode is continuously de-energized to its thermal limit by the detection circuit, repeatedly coupling between it and one of the radial modes can be used to de-energize the latter to its thermal limit as well. Instead of repeatedly coupling, a " π -pulse" can be used

⁹ Simulations show that $C_{\text{CE AC},1,1}/V_{\text{CE AC}} = 1.3 \text{ m}^{-1}$ [50].

as well - a coupling applied for exactly the suitable duration in order to transfer all of the excess energy from the radial mode to the axial mode. Practically at THe-Trap, the coupling drive is applied for about a minute while its frequency is scanned periodically across a range of about 100 Hz every 10 s. It was experimentally observed that for a large parameter space of drive amplitude, frequency scan width and frequency scan time, as long as the suitable frequency ($\omega_{\text{drive}} = \omega_+ - \omega_z$ or $\omega_{\text{drive}} = \omega_z + \omega_-$) is included within the scan, the radial mode is effectively de-energized to its thermal limit, as if a π -pulse was applied. This was identified by a previous member of the group [56] to be a classical analogy of the adiabatic rapid passage [57].

2.6 SYSTEMATIC SHIFTS

The effects mentioned in Section 2.4 affect the charged particle's frequencies of motion. As a result the frequencies measured are "shifted". To correct for this, the different shifts need to be calculated and then added or subtracted to each measured frequency in order to arrive at the real ones¹⁰. The shifts are divided into 4 categories: Electric field shifts, magnetic field shifts, mixed shifts, and THe-Trap shifts. In general, deviations tend to become more prominent the further away the ion oscillates from the trap center, as in the larger its amplitude. It is for this reason that the energy of the modes of motion should be kept at the minimum required in order to perform the measurement.

As described in Section 4.3, in THe-Trap the trapped particle's axial frequency is kept constant through a feedback loop that continuously changes the ring voltage. As a result, shifts to the axial frequency ω_z also shift the ring voltage, which then cause a shift in the radial frequencies ω_{\pm} . The shifts under lock are then given by [56]

$$\Delta\omega_{\pm\text{lock}} = \Delta\omega_{\pm} \pm \frac{\omega_z \Delta\omega_z}{\omega_+ - \omega_-}, \quad (2.48)$$

where $\Delta\omega_z$ is the axial frequency shift, $\Delta\omega_{\pm}$ are the radial frequency shifts and $\Delta\omega_{\pm\text{lock}}$ are the radial frequency shifts when the ion is in lock.

See Section 4.11 for a list of the systematic shift values and their uncertainties for the different ions.

2.6.1 Electric Field Shifts

Since the electrodes are cylindrically-symmetric and the ion moves harmonically in the trap, many machining imperfections can be treated as cylindrically-symmetrical, such that they

¹⁰ The derivations are explained non-rigorously and the end results cited, with the exception of the relativity shift, the derivation of which can be found in Section ?? as an example for how some of the other shifts can be derivated as well. In addition, additional formulas for the different shifts which were not used in the thesis can be found in the appendix.

are negligible when using the invariance theorem (Equation (2.8)). In addition, the invariance theorem holds in the case of trap tilt and trap ellipticity.

2.6.1.1 The $C_{total\ 4}$ and $C_{total\ 6}$ Shifts

The electrostatic field becomes less symmetrical due to deviations from the ideal geometry of the Penning-trap, such as machining imperfections and holes for ion injection. As a result additional terms $C_{l,m}$ contribute to the potential. Symmetry to reflection around the z direction ($C_{l,m} = 0$ for odd l) and cylindrical symmetry ($C_{l,m} = 0$ for $m \neq 0$) are assumed to be maintained. As a result, the next two largest terms after C_2 are C_4 and C_6 , as referred to in Section 2.6. It can be shown [56, 58] that the frequency shifts due to C_4 are:

$$\frac{\Delta\omega_z}{\omega_z} = \frac{3C_4}{4C_2} (-2A_+^2 + A_z^2 - 2A_-^2), \quad (2.49)$$

$$\frac{\Delta\omega_{\pm\ \text{lock}}}{\omega_{\pm}} = \mp \frac{3C_4}{2C_2} \frac{\omega_{\mp}}{\omega_+ - \omega_-} (A_{\pm}^2 + A_z^2), \quad (2.50)$$

and that the frequency shifts due to C_6 are:

$$\frac{\Delta\omega_z}{\omega_z} = \frac{45C_6}{48C_2} (3A_+^4 + A_z^4 - 6A_+^2A_z^2 + 12A_+^2A_-^2 - 6A_-^2A_z^2 + 3A_-^4), \quad (2.51)$$

$$\frac{\Delta\omega_{\pm\ \text{lock}}}{\omega_{\pm}} = \pm \frac{45C_6}{12C_2} \frac{\omega_{\mp}}{\omega_+ - \omega_-} (A_{\pm}^4 - A_z^4 + 3A_+^2A_-^2 + 3A_{\mp}^2A_z^2). \quad (2.52)$$

Typically for THE-Trap $\Delta\omega^{(12C^{4+})}_{C_4}/\omega^{(12C^{4+})} \approx 30(30) \cdot 10^{-12}$ and $\Delta\omega^{(12C^{4+})}_{C_6}/\omega^{(12C^{4+})} \approx 0.1(10) \cdot 10^{-12}$, such that both shifts are negligible.

2.6.1.2 Relativistic Shift

The relativistic mass increase of the ion changes the equations of motion and the resulting frequencies. The derivation shows [56, 36] that substitution of the relativistic momentum $\vec{p} \rightarrow \gamma\vec{p} = \gamma m\vec{v}$ into the equations of motion while omitting non-resonance terms results in the following frequency shifts:

$$\frac{\Delta\omega_z}{\omega_z} \approx -\frac{(\omega_+A_+)^2 + (\omega_-A_-)^2}{4c^2} - \frac{3\omega_z^2A_z^2}{16c^2}, \quad (2.53)$$

$$\frac{\Delta\omega_{\pm\ \text{lock}}}{\omega_{\pm}} \approx \mp \frac{\omega_{\pm}}{\omega_+ - \omega_-} \frac{(\omega_{\pm}A_{\pm})^2 + 2(\omega_{\mp}A_{\mp})^2 + \frac{1}{2}\omega_z^2z^2}{2c^2} \pm \frac{\omega_z^2 \left(-\frac{(\omega_+A_+)^2 + (\omega_-A_-)^2}{4c^2} + \frac{3\omega_z^2A_z^2}{16c^2} \right)}{(\omega_+ - \omega_-)\omega_z\omega_{\pm}}.$$

(2.54)

Typically for THe-Trap $\Delta\omega(^{12}\text{C}^{4+})_{\text{relativistic}}/\omega(^{12}\text{C}^{4+}) \approx -5(10) \cdot 10^{-12}$, such that the relativistic shift is negligible.

2.6.1.3 Image Charge Shift

Image charges are induced in the electrodes by the trapped ion in order to keep the electrode surfaces equipotential. As a result, an additional electric field is induced. Since the trap dimensions are significantly smaller than the wavelengths associated with the modes of motion the field can be considered electrostatic. The induced electric field generally does not satisfy Laplace's equation, such that the Invariance Theorem is violated and the cyclotron frequency is shifted as well. The resulting shifts are [50]

$$\frac{\Delta\omega_z}{\omega_z} \approx -\frac{nq}{m} \frac{E'_z}{2\omega_z^2} \quad (2.55)$$

$$\frac{\Delta\omega_{\pm \text{lock}}}{\omega_{\pm}} \approx \mp \frac{nq(2E'_\rho + E_z)}{2m(\omega_+ - \omega_-)} \approx \mp \frac{n(2E'_\rho + E_z)}{2B}, \quad (2.56)$$

where n is the number of charges ($q = ne$) and E'_z and E'_ρ are the axial and radial amplitudes of the field created by the images charges, simulated for THe-Trap to be $E'_\rho = 4.23(9) \cdot 10^{-2} \text{Vm}^{-2}$, $E'_z = 8.04(13) \cdot 10^{-2} \text{Vm}^{-2}$ [47].

Typically for THe-Trap $\Delta\omega(^{12}\text{C}^{4+})_{\text{image charge}}/\omega(^{12}\text{C}^{4+}) \approx -310(5) \cdot 10^{-12}$, making the image charge shift one of the most significant shift in terms of its magnitude, although its uncertainty is negligible.

2.6.1.4 Trap Tilt & Trap Ellipticity

Trap Tilt:

The Penning-trap is not perfectly aligned. In order to calculate the resulting shift, it is assumed that $\vec{B} \parallel \hat{z}$ and that the trap is tilted by θ around the y direction. Substitution of $x \rightarrow x \cos(\theta) + z \sin(\theta)$, $y \rightarrow y$, $z \rightarrow -x \sin(\theta) + z \cos(\theta)$ into the electric potential while omitting non-resonant terms shows that the frequencies are shifted by [50]:

$$\frac{\Delta\omega_z}{\omega_z} \approx -\frac{3\theta^2}{4}, \quad \frac{\Delta\omega_{+ \text{lock}}}{\omega_+} \approx 0, \quad \frac{\Delta\omega_{- \text{lock}}}{\omega_-} \approx \frac{9}{4}\theta^2. \quad (2.57)$$

Typically $\theta \approx 0.1^\circ$ [55] or $0.05^\circ < \theta < 0.5^\circ$ [50] which lead to $\frac{\Delta\omega_z}{\omega_z} \approx 10 \text{ mHz}$ and $\frac{\Delta\omega_{- \text{lock}}}{\omega_-} \approx 20 \text{ mHz}$, making trap tilt and ellipticity the most dominant systematic shifts in Penning-traps

[59]. However, in practice they are cancelled out when calculating ω_c using the first equation in Equation (2.8), such that they are considered negligible. The shift due to the trap tilt is not cancelled out when calculating ω_c using the second equation in Equation (2.8), such that the difference in ω_c obtained with the two formulas can be used to calculate θ using [36, 38]

$$\sin \theta \approx \theta \approx \frac{2}{3} \sqrt{\frac{2\tilde{\omega}_+ \tilde{\omega}_-}{\tilde{\omega}_z^2} - 1}, \quad (2.58)$$

where $\tilde{\omega}_z$ and $\tilde{\omega}_\pm$ in the above formula are the shifted frequencies.

Trap ellipticity:

The electrical shift is shifted due to elliptical deformations in the following way [36]:

$$\vec{E} \rightarrow \vec{E} - \frac{m\omega_z^2 \epsilon}{2q} \begin{pmatrix} -x \\ y \\ 0 \end{pmatrix}, \quad (2.59)$$

where ϵ characterizes the strength of the elliptical deformation. The frequency shifts can be shown to be [36]

$$\frac{\Delta\omega_{- \text{lock}}}{\omega_-} = \frac{\Delta\omega_-}{\omega_-} = -\frac{\epsilon}{2'}, \quad \frac{\Delta\omega_{+ \text{lock}}}{\omega_+} = \frac{\Delta\omega_+}{\omega_+} = \frac{\Delta\omega_z}{\omega_z} = 0. \quad (2.60)$$

As mentioned above, the shift due to the trap ellipticity, just like the shift due to the trap tilt, is cancelled out to first order when calculating ω_c using Equation (2.8).

2.6.2 Magnetic Field Shift - B_2

Similarly to the expansion of the electrostatic potential shown in Section 2.4, the magnetic potential can be defined and expanded as well. The magnetic field is created by superconducting coils surrounding the traps such that the trap region is source-free. As a result, the magnetic field can be defined by a scalar magnetic potential Ψ such that $\vec{B} = -\vec{\nabla}\Psi$ and $\Delta\Psi = 0$. Similarly to the electrostatic field, due to the rotational symmetry the coefficients of all $r^l Y_{l,m}$ with $m \neq 0$ are zero, such that the magnetic potential can be defined by

$$\Psi = \sum_{l=0}^{\infty} B_{2l} r^{2l} \Re(Y_{2l,0}), \quad (2.61)$$

where B_{2l} are the coefficients of the $r^{2l} \Re(Y_{2l,0})$ functions and $B_0 = B$ is the magnetic field amplitude. The next leading order coefficient is B_2 . It can be shown [36, 56, 60, 58] that the frequency shifts resulting from B_2 are

$$\frac{\Delta\omega_z}{\omega_z} = \frac{B_2}{2B_0} \frac{\omega_c}{\omega_z^2} (\omega_+ A_+^2 + \omega_- A_-^2), \quad (2.62)$$

$$\frac{\Delta\omega_{\pm \text{ lock}}}{\omega_{\pm}} = \pm \frac{B_2}{2B_0} \frac{\omega_c}{\omega_{\pm} (\omega_+ - \omega_-)} (\omega_{\pm} A_z^2 - \omega_{\pm} A_{\pm}^2). \quad (2.63)$$

Typically for THE-Trap $\Delta\omega^{(12\text{C}^{4+})}_{B_2}/\omega^{(12\text{C}^{4+})} \approx -20(10) \cdot 10^{-12}$, such that the B_2 shift is negligible.

2.6.3 Mixed Shift - $C_1 B_1$

Although C_1 and B_1 were individually treated as negligible in sections 2.6.1.1 and 2.6.2 respectively, their combined effect is significant due to its high uncertainty. A potential difference between the end-caps, for instance due to distributions of surface charges frozen on the end-caps due to the liquid hydrogen cooling, shifts the position of the ion by [50]

$$\Delta z = -\frac{qC_1}{m\omega_z^2}. \quad (2.64)$$

In the presence of a $B_1 \neq 0$, the magnetic field changes by $\Delta B = B_1 \Delta z$ across a distance Δz , such that the cyclotron frequency is shifted by

$$\frac{\Delta\omega_c}{\omega_c} = \frac{q\Delta B}{m\omega_c} = \frac{q\Delta z B_1}{m\omega_c}. \quad (2.65)$$

The value used for C_1 in THE-Trap is $C_1 = 0 \pm \frac{100}{5} \frac{\text{mV}}{\text{mm}}$, with the uncertainty estimated using the maximal drop voltage used in THE-Trap, see Section 4.1. The value used for B_1 in THE-Trap is $B_1 = 10^{-3} \pm 10^{-4} \frac{\text{T}}{\text{m}}$ based on upper limit estimations [61].

Typically for THE-Trap $\Delta\omega^{(12\text{C}^{4+})}_{C_1 B_1}/\omega^{(12\text{C}^{4+})} \approx 0(200) \cdot 10^{-12}$, such that although the magnitude of the shift is zero, it is still significant since it has the largest uncertainty.

2.6.4 THE-Trap Shifts

THE-Trap shifts are systematic shifts specific to the measurement scheme used in THE-Trap. The phase, ring modulation and DC offset systematic shifts are a result of the ion's axial frequency being locked as explained in Section 3.4.1.

2.6.4.1 "Sweeps" Fit

A systematic uncertainty of either 2 mHz or 10 mHz was added to each measurement as a result of the measurement method used in this thesis (see Section 4.8). These correspond to $\Delta\omega^{(12\text{C}^{4+})}_{\text{fit}}/\omega^{(12\text{C}^{4+})} = 0(68) \cdot 10^{-12}$ and $\Delta\omega^{(12\text{C}^{4+})}_{\text{fit}}/\omega^{(12\text{C}^{4+})} = 0(341) \cdot 10^{-12}$ respectively, the latter being one of the largest systematic shifts in terms of its uncertainty.

2.6.4.2 Phase Shift

A phase shift causes the error signal waveform to change its shape, shifting the equilibrium point of the voltage and thus the axial frequency. The shifts are

$$\frac{\Delta\omega_z}{\omega_z} = -\frac{\gamma}{2\omega_z} (\Delta\theta)^2, \quad \frac{\Delta\omega_{\pm\text{lock}}}{\omega_{\pm}} = \mp \frac{\omega_z}{\omega_{\pm} (\omega_+ - \omega_-)} \frac{\gamma}{2} (\Delta\theta)^2. \quad (2.66)$$

Typically for THe-Trap $\Delta\omega^{(12\text{C}^{4+})}_{\text{phase shift}}/\omega^{(12\text{C}^{4+})} \approx 0(150) \cdot 10^{-12}$, such that the phase shift is significant due to its uncertainty.

2.6.4.3 Ring Electrode Modulation Shift

As explained in Section 2.5.1, the ring electrode's voltage is changed from DC to a mixture of DC and AC: $V_R \rightarrow V_R + V_{\text{mod}} \cos(\omega_{\text{mod}} \cdot t)$, where $V_{\text{mod}} \ll V_R$ and $\omega_{\text{mod}} \ll \omega_z$. Since $\omega_z \propto \sqrt{V_R}$ as shown in Equation (2.14), and the temporal average of the signal amplitude is not zero due to the non-linearity of the waveform, the axial frequency is shifted by the modulation signal. The shift can be shown to be [36, 56]

$$\frac{\Delta\omega_z}{\omega_z} = -\frac{1}{16} \left(\frac{V_{\text{mod}}}{V_R} \right)^2, \quad \frac{\Delta\omega_{\pm\text{lock}}}{\omega_{\pm}} = \mp \frac{\omega_z^2}{16\omega_{\pm} (\omega_+ - \omega_-)} \left(\frac{V_{\text{mod}}}{V_R} \right)^2. \quad (2.67)$$

Typically for THe-Trap $\Delta\omega^{(12\text{C}^{4+})}_{\text{mod}}/\omega^{(12\text{C}^{4+})} \approx -320(20) \cdot 10^{-12}$, such that the modulation shift is one of the largest shifts in terms of its magnitude.

2.6.4.4 Lock DC Offset

A DC offset to the correction voltage of the axial lock causes the error signal waveform to shift along the vertical direction such that the equilibrium point of the voltage shifts, which then shifts the axial frequency. The shifts are

$$\frac{\Delta\omega_z}{\omega_z} = -\frac{\gamma}{2\omega_z} \left(\frac{V_{\text{offset}}}{V_{\text{error}}} \right)^2, \quad \frac{\Delta\omega_{\pm\text{lock}}}{\omega_{\pm}} = \mp \frac{\omega_z^2}{\omega_{\pm} (\omega_+ - \omega_-)} \frac{\gamma}{2\omega_z} \left(\frac{V_{\text{offset}}}{V_{\text{error}}} \right)^2, \quad (2.68)$$

where γ is the damping defined in Equation (2.23).

Typically for THe-Trap $\Delta\omega^{(12\text{C}^{4+})}_{\text{DC offset}}/\omega^{(12\text{C}^{4+})} \approx -1(0.1) \cdot 10^{-12}$, such that the DC offset is negligible.

2.6.4.5 Coil Pushing

The tuned circuit has been observed to “jump” every few hours, such that the tuned circuit is shifted by about -300 Hz and then returns to the previous value after about one hour. The cause is assumed to be the amplifier heating the liquid helium around it, occasionally creating

bubbles which might get trapped for a while and change the resonance frequency by changing the capacitance. A relative uncertainty of $\Delta\omega(^{12}\text{C}^{4+})_{\text{coil pushing}}/\omega(^{12}\text{C}^{4+}) \approx 0(40) \cdot 10^{-12}$ was assigned in order to account for this [61].

THE EXPERIMENTAL SETUP

THE-Trap, originally UW-PTMS, is a Penning-trap experiment utilizing a ~ 5.2 Tesla superconducting magnet (see Section 3.1) built in 1998 and originally located at the University of Washington, Seattle, under the supervision of Prof. R. S. Van Dyck Jr. [62]. In 2008 it was moved to the Max Plank Institute for Nuclear Physics in Heidelberg, Germany, under the supervision of Prof. Klaus Blaum [48]. The experiment spans across two rooms. The upper room contains electronics and cabling and a crane for controlling and lifting the experimental apparatus (see Section 3.2). The lower room contains the superconducting magnet, the experimental apparatus positioned inside the magnet, the stable power supply and the environmental stabilization system (see Section 3.3).

In Section 3.1 the superconducting magnet is described as shown in Figure 3.1 including its repair (Section 3.1.1), shimming as shown in Figure 3.3 (Section 3.1.2) and shielding factor measurements as shown in Figure 3.4 (Section 3.1.3). In Section 3.2 the experimental apparatus is explained including the gas inlet system as shown in Figure 3.6 (Section 3.2.1). In Section 3.3 the stabilization system is expanded upon including the new data acquisition system (Section 3.3.1) and website (Section 3.3.2). In Section 3.4 loading and manipulation of ions is discussed including locking and detecting the axial mode as shown in Figure 3.11 (Section 3.4.1) and detection of the radial modes (Section 3.4.2).

Additional details on the experimental setup are found in the following theses [62, 63, 58, 47, 50] and articles [48, 64].

3.1 THE MAGNET

The ~ 5.2 Tesla superconducting magnet was designed by Prof. R. S. Van Dyck Jr. [65] and built by Nalorac Cryogenic Corporation in 1998. Its internal structure is onion-like in order to minimize Liquid Helium (LHe) losses. Specifically, the superconducting coils are submerged in LHe, which is enclosed in a vacuum layer, a Liquid Nitrogen (LN) reservoir and a layer of the same vacuum. There are three LHe ports - the cold bore where the trap tower is inserted into, the “charging stack” which is used for charging the magnet and the “filling stack” which is used for filling LHe. There are two LN₂ ports or “stacks” for filling LN₂. See Figure 3.1.

The largest contribution to the measurement uncertainty comes from temporal fluctuations in the magnetic field. As a result there are several mechanisms in place to keep the magnetic field static. To damp vibrations, the LHe reservoir, including the superconducting coils holder called the “pot”, are suspended on the bore joint from above, see Section 3.1.1. In addition, the magnet is placed on foundations which are mechanically de-coupled from those of the building. To reduce temperature fluctuations, which cause permeability and thus magnetic

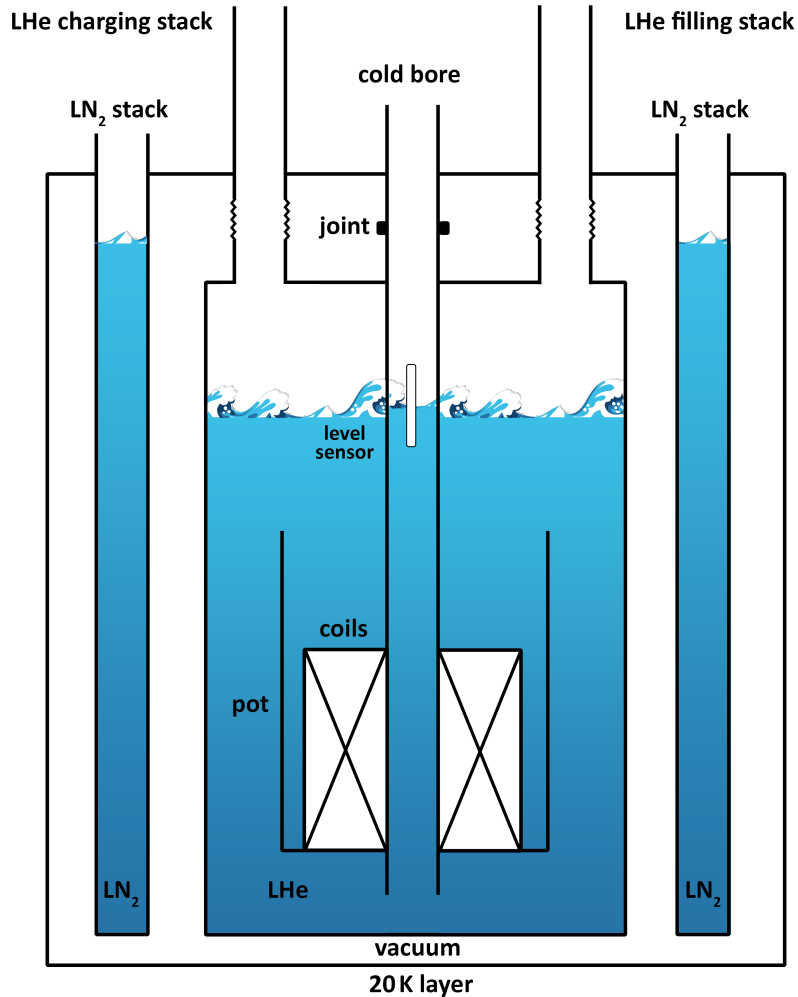


Figure 3.1: The magnet as described in Section 3.1. The superconducting coils are held in a structure called the “pot” submerged in LHe. A level sensor is used as part of a system for regulating the LHe pressure and level. Surrounding the LHe reservoir are insulation compartments for reducing LHe loss - a vacuum compartment, a liquid nitrogen reservoir with two openings for filling and another vacuum compartment. The LHe reservoir has three openings: The “bore” is used for inserting the experimental apparatus and the left and right “stacks” are used for charging and filling the magnet respectively. Note that the LHe reservoir is hung from above through flexible bellows on the stacks and the bore joint on the bore in order to suppress vibrations and so magnetic field fluctuations.

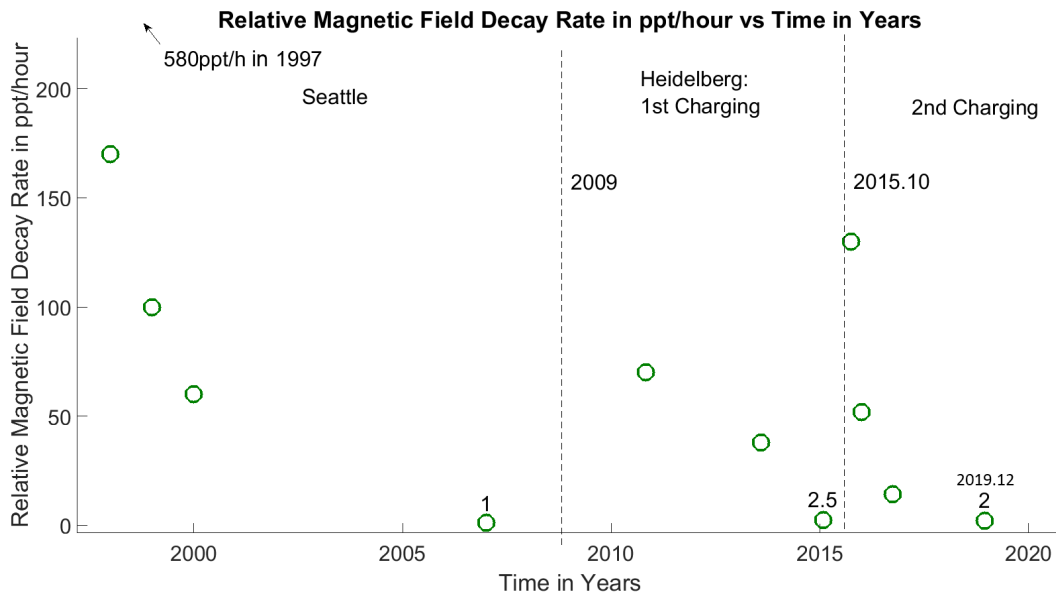


Figure 3.2: The magnet's relative magnetic field decay rate in ppt/h ($10^{-12}/h$). Starting at hundreds of ppt/h in Seattle, it went down to 1 ppt by 2007. In 2009 the magnet was moved to Heidelberg and recharged, reaching the same order of magnitude after about seven years. At the end of 2015 the magnet was charged again, this time using the trick of overcharging the main coil currents to 100.2% of the desired current and then lowering it back to 100%. It is probably as a result of the overcharging trick that the decay rate decreased faster, achieving the same order of magnitude as in Seattle within four years.

field fluctuations, the helium gas pressure and LHe level are regulated with the use of pressure and level sensors controlling valves and a pump, see Section 3.3. Temperature fluctuations are further suppressed by the bore being a cold bore, which results in the experimental apparatus being kept at a constant LHe temperature. To suppress external magnetic field fluctuations additional superconducting coils are used, called shielding coils, which have a similar structure to that of the main coils and passively suppress changes to the magnetic field by induced currents, see Section 3.1.3. Magnetic field fluctuations are monitored using a fluxgate sensor, which can be connected to Helmholtz coils surrounding the magnet to suppress the magnetic field fluctuations in the lower trap region by a factor of three [50]. The Helmholtz coils were not used in this thesis. Lastly, shimming coils are used to make the magnetic field homogeneous in the trap region. These are superconducting coils arranged in different configurations such that each has a strong contribution to the magnet field with respect to a specific spatial component, for instance x or y^2 . They can be tuned to cancel out the spatial components of the main coils, see Section 3.1.2. The resulting temporal decay rate of the magnetic field due to the above-mentioned suppression mechanisms is considered especially low in comparison to other magnets, see Figure 3.2.

3.1.1 *The Repair of the Magnet*

The magnet quenched in January 2015 due to miscommunication regarding the filling of liquid nitrogen (LN). Following the quench, the vacuum of the magnet was tested under both room temperature conditions and LN temperature several times. The temperature changes due to the tests led to a leak and eventually to a complete break of the glue in the bore joint, which is a joint connecting the two G10 parts of the bore with the epoxy glue Armstrong A12, see Figure 3.1. As the glue broke, the LHe reservoir, including the chamber containing the superconducting coils called the “pot”, dropped a few centimeters onto the 20 K surface shield, stretching the flexible bellows of the LHe stacks. In addition to the repair of the joint it was decided to have the magnet undergo a maintenance phase, both of which were performed by the group members. During the maintenance phase part of the magnet top cover and many O-Rings were found to be in an eroded state and were replaced with new Viton ones. To prevent erosion, epoxy spray was sprayed on the magnet top cover, its screws were sealed with theorstat and tape and the stacks were surrounded by Styrofoam and towels. The O-Rings beneath the LN₂ stacks were not replaced as it was impossible to do so without cutting the magnet open. In addition, “Spring-loaded studs” were used to seal the magnet’s bottom entrance port to be used as an extra emergency exit path for LHe in case of a quench. In October 2015 the repair was finished, the magnet charged and shimmed and the trap tower re-inserted.

3.1.2 *Shimming the Magnet*

Shimming is the process of making the magnetic field more homogeneous around a specific region, in this case the region of the lower trap. It is done by the use of the shimming coils, which are coils arranged such that each primarily contributes to a specific spatial component of the magnetic field, such as x , y or z^2 . By applying the suitable amount of current to each coil the non-homogeneous contributions of the main and the shimming coils cancel each other out. In 2009 the magnet was not shimmed as the electrical connections were blocked with ice. The relative homogeneity of the magnet was $\approx 10^{-5}$ around a 1 cm^3 volume [66]. After the magnet repair in 2015 the opportunity was used to shim it to a relative homogeneity of $8.2 \cdot 10^{-8}$ around a 1 cm^3 volume, see Figure 3.3, which is about 100 times more homogeneous than before. The measurement was performed using an NMR probe inserted into a “warm bore”, a cylinder-shaped structure capped from the bottom inserted into the bore in order to make the bore region temporarily LHe-free and warm enough for shimming. Initially a water sample was used, but due to the below-freezing temperature inside the warm bore it was replaced with an acetone sample.

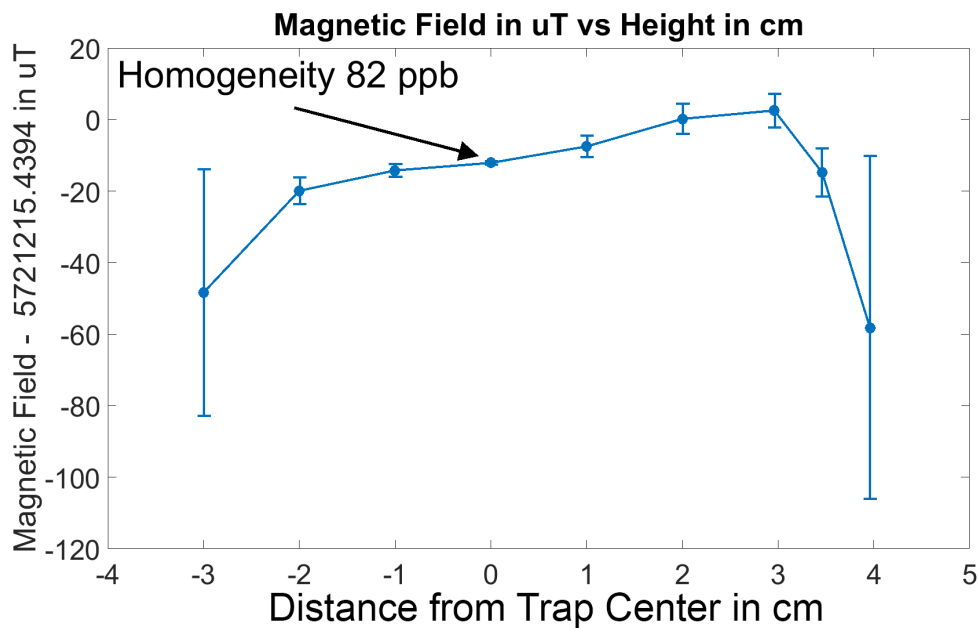


Figure 3.3: The results of shimming the magnet - the magnetic field in μT as a function the axial distance from the trap center in cm. The homogeneity, or relative uncertainty of the magnetic field at the trap region, which corresponds to the position $z = 0$, is shown to be $8.2 \cdot 10^{-8}$.

3.1.3 Shielding Factor Measurements

In addition to the main superconducting coils for generating the magnetic field and the shimming superconducting coils, there are additional superconducting coils for suppressing magnetic field fluctuations, for instance due to movement of people or objects in the vicinity of the magnet. The reciprocal of the suppression ratio in the trap region, or the ratio between the magnetic field measured outside of the magnet and the resulting magnetic field in the trap region is called the shielding factor. The shielding factor was measured to be 180 (uncertainty unknown) back when the magnet was in Seattle [65]. Since then, three additional measurements were performed in Heidelberg, see Figure 3.4. All three measurements use external Helmholtz coils for changing the magnetic field in the trap region. The first measurement yielded 169(13) and was performed using a Fluxgate Magnetometer before the magnet was charged following the quench in 2015. The second measurement resulted in 179(14) and was performed using an NMR probe after the magnet was recharged. The third measurement yielded 173(2) and was performed after inserting the experimental apparatus (Section 3.2) back into the magnet and successfully loading and manipulating $^{12}\text{C}^{4+}$ ions. It involved repeatedly measuring the modified cyclotron frequency of a $^{12}\text{C}^{4+}$ ion using the “sweeps” measurement method (see Section 4.8) while changing the magnetic field in the trap region. The changes in the cyclotron frequency correspond to changes in the magnetic field in the trap region by the use of Equation (2.2).

3.2 THE TRAP TOWER

The Penning-trap is connected to a tower-shaped structure which is inserted into the superconducting magnet, see Figure 3.5. At the top is a scroll pump (not drawn), a turbo pump, an ion source which was never used, the gas injection system (not drawn, see Section 3.2.1) and outlets for electrical connections going down into the traps region. Near the bottom of the tower are two hyperbolic Penning-traps, only the bottom of which is in use. Below it at the very bottom is the resonator, the cryo-amplification and a field emission point (FEP), see Section 3.4. The traps are separated from the rest of the trap tower by a manual valve and by a computer-controlled pneumatic valve [47], which automatically closes when the vacuum pressure exceeds a certain threshold (not drawn).

3.2.1 The Gas Inlet System

A gas inlet system was implemented, allowing trapping of ions not available by extraction from the trap surfaces or from the residual gas, see Figure 3.6. A gas bottle containing either a natural mixture of neon isotopes or a mixture enriched in ^{22}Ne is connected to the apparatus through a pressure reducer and a series of valves. A fine-leak valve is used to introduce the minimal neon pressure necessary for loading neon ions. For the neon loading process, all other valves between the neon gas bottle and the traps are open except for a computer-controlled pneumatic valve. This valve is opened for a duration of one second during ion loading, see Section 3.4. This introduces neon gas into the trap region which is then ionized using the FEP (see Section 3.4) and trapped. The pressure in the trap region is low enough such that ions can stay trapped for several weeks.

3.3 THE STABILIZATION SYSTEM

As mentioned in Section 3.1, temporal and spatial magnetic field stability is important and achieved primarily by stabilization of the helium gas pressure and LHe level, see Figure 3.7. The pressure in the bore is continuously compared and regulated to that of an Absolute Pressure Reference (APR) by the use of a valve and a pump. The level in the bore is continuously compared and regulated to a reading from a level sensor unit with the use of two valves, one controlling pressure release from the bore and the other from the reservoir. Aside from the pressure and the level, the temperature in both rooms is regulated as well. Other parameters, such as the pressure in the room itself, the temperature in different positions in the room, the humidity and changes in the magnetic field are also recorded [67].

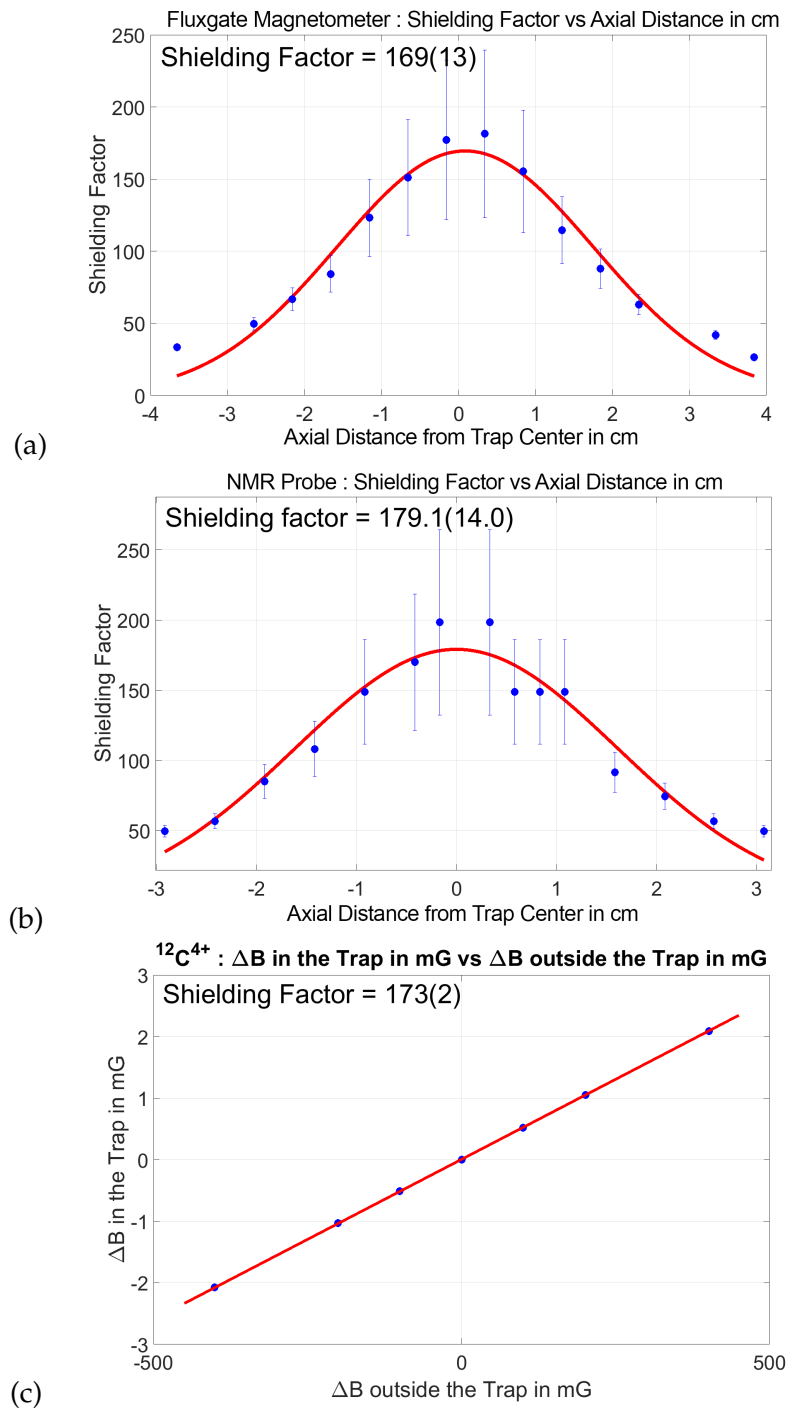


Figure 3.4: Shielding factor measurements. Graph (a) was measured before the magnet was recharged and displays the shielding factor as the ratio between the magnetic field measured inside the magnet using a fluxgate magnetometer and that applied externally using Helmholtz coils surrounding the magnet. The height scale is shifted such that the origin corresponds to the location of the bottom trap. Graph (b) was measured after the magnetic field was charged and displays the same but using an NMR probe. The height scale has a different origin than in (a) but is shifted such that the origin corresponds to the location of the bottom trap. Graph 3 was measured after the experimental apparatus (Section 3.2) was re-inserted and ion loading and manipulation was re-established. It displays the magnetic field change corresponding to changes in the cyclotron frequency of a $^{12}\text{C}^{4+}$ as a function of that of the Helmholtz coils. All three measurements are in agreement. See Section 3.1.3.

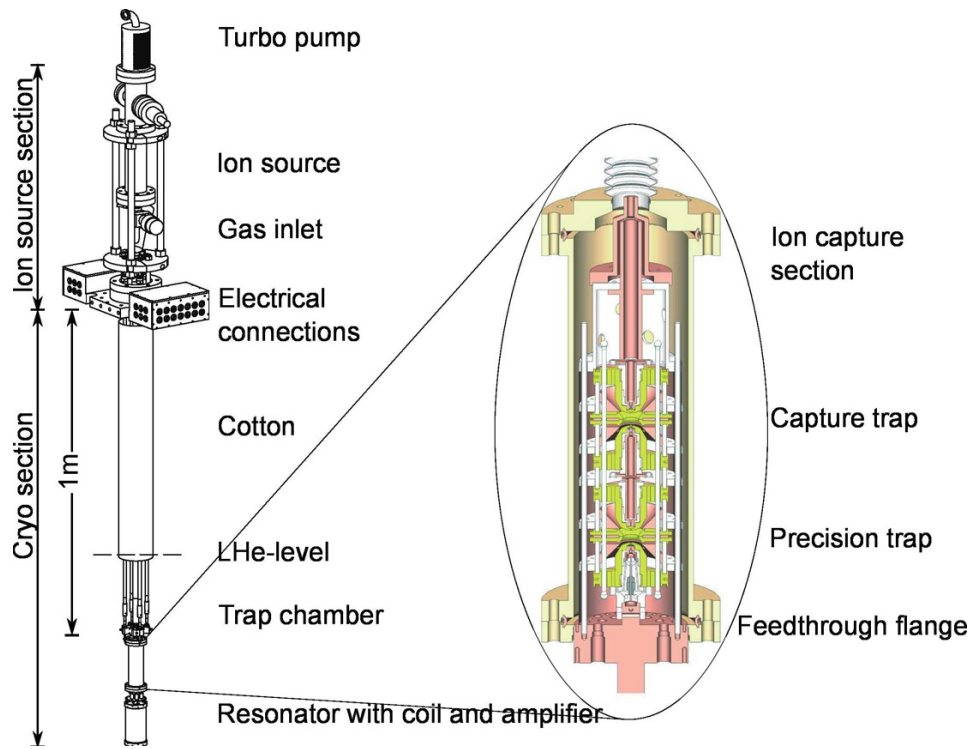


Figure 3.5: The trap tower and the two traps. For more details see Section 1.1.

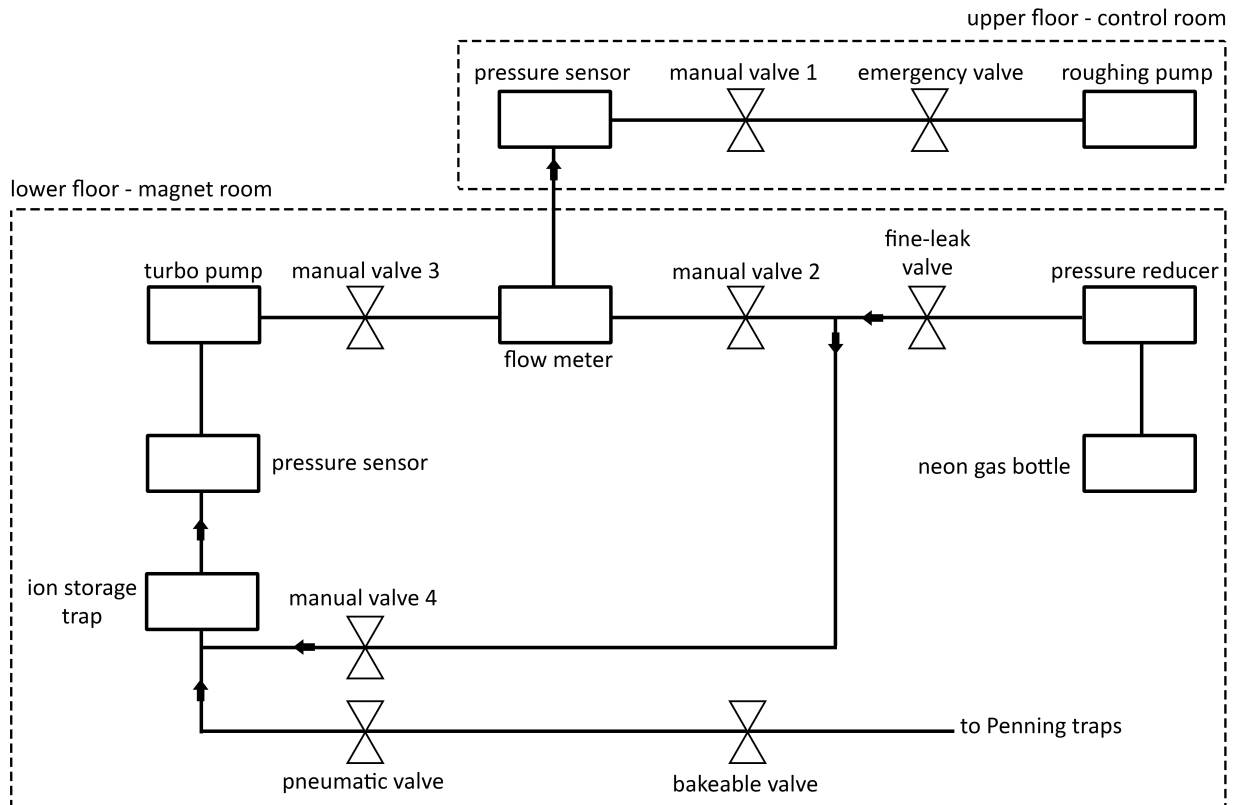


Figure 3.6: The gas inlet system. A neon gas bottle is used to inject gas down into the Penning-traps region containing the storage trap and the experimental trap beneath it. The gas is injected through a pressure reducer, a fine-leak valve, a manual valve, a computer-controlled pneumatic valve and a bakeable manual valve. For injecting neon these are all kept open except for the pneumatic valve, which is opened for one second during electron emission, see Section 3.4. Regarding the other components - manual valve 2 is the only manual valve which stays closed in regular operation as it is used for pumping the system following gas bottle exchange. The emergency valve closes automatically in case the pumps fail and the rough pressure exceeds 0.1 mbar. The ion storage trap was never used.

3.3.1 *New Data Acquisition Program - “PyEnvDAQ”*

The system parameters were originally recorded using a program written in C. A new program was written in Python, “PyEnvDAQ” (Python Environmental Data Acquisition System), see Figure 3.8. The new program provides additional features such as email and Telegram alerts in case the values of recorded parameters are found outside of their pre-defined ranges, advanced plotting options and export options. It also outputs the recorded data in a new format which is compatible with the new controller [68].

3.3.2 *New Group Website - “The-Website”*

The group website was redesigned in order to provide compatibility with the new mass measurement data file formats created by the new controller program [68] and with the new stabilization system data format created by PyEnvDAQ, see Section 3.3.1. It also provides more plotting options for the parameters of the stabilization system, an updated links menu and pre-analysis of calibration data in real time, helping with decision-making during measurements and thus speeding up the process.

3.4 LOADING AND MANIPULATING IONS

Ions are loaded using a Field Emission Point (FEP) which releases an electron beam of a few nA. These electrons then oscillate between the FEP and the top skimmer electrode, which is an electrode placed between the two traps, until they collide either with residual or injected gas molecules, for instance injected neon gas, or with the trap surfaces, releasing and ionizing atoms absorbed into the trap surfaces in the process. The ions are trapped using the electrostatic and the magnetic fields of the trap. In THE-Trap a FEP voltage of -230V is required to ionize $^{12}\text{C}^{4+}$ from the trap surfaces and -390V for ionizing $^{20}\text{Ne}^{8+}$ and $^{22}\text{Ne}^{7+}$ from injected neon gas. The process for removing ions until only one is left is described in Section 4.1. The detectable and trappable ions in THE-Trap are shown in Figure 3.10 and [48, 63].

3.4.1 *Locking and detecting the Axial Mode*

The axial frequency is kept constant, or locked. This cancels axial frequency shifts caused by energy changes of the radial modes and is essential for the measurement process, see Chapter 4. The locking is achieved by the use of a correction circuit, see Figure 3.11. The ion’s axial mode

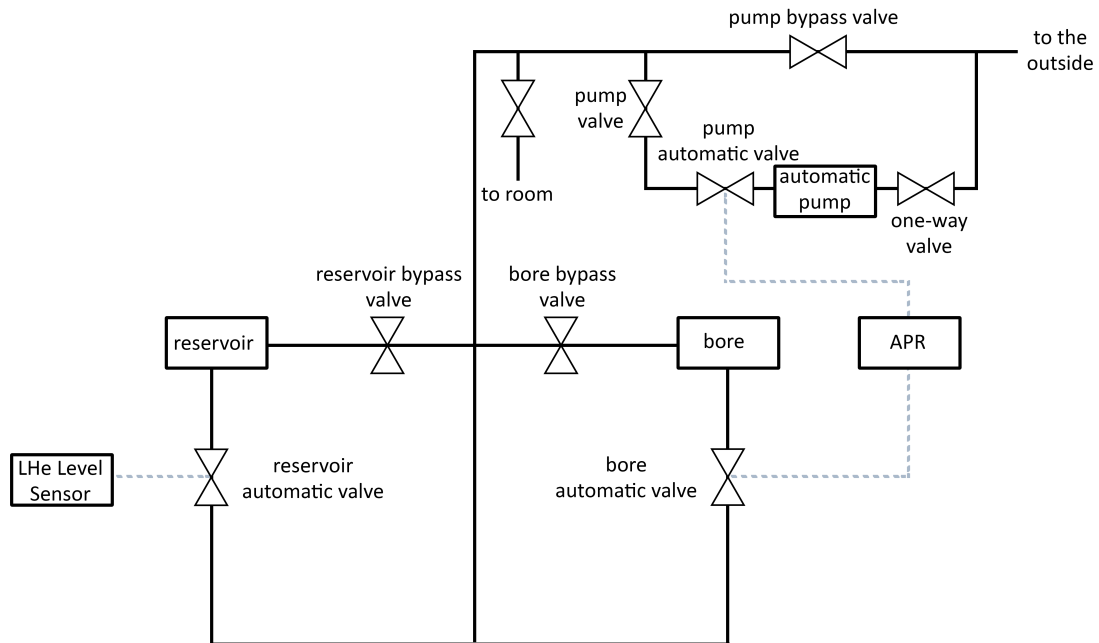


Figure 3.7: The stabilization system. The helium gas pressure in the bore is continuously compared and regulated to that of an Absolute Pressure Reference (APR) unit using a PI control system (not drawn) which controls both the bore and the pump automatic valves. The liquid helium level is measured and regulated using a PI control system which controls the reservoir automatic valve and thus the helium gas pressure in the reservoir. The bore, reservoir and pump bypass valves are closed during regular operation, such that the helium gas from the bore and the reservoir flows through their respective automatic valves through the pump and its valves to the outside. In this way both the helium gas pressure and the liquid helium level in the bore stay constant. It is also possible to turn off the level stabilization system by opening the bore and reservoir bypass valves, such that the helium gas flows from the bore and the reservoir through the pump and its valves straight to the outside. The pump and its valves are bypassed during liquid helium filling by opening the pump bypass valve. For a more detailed drawing and explanation see [67].

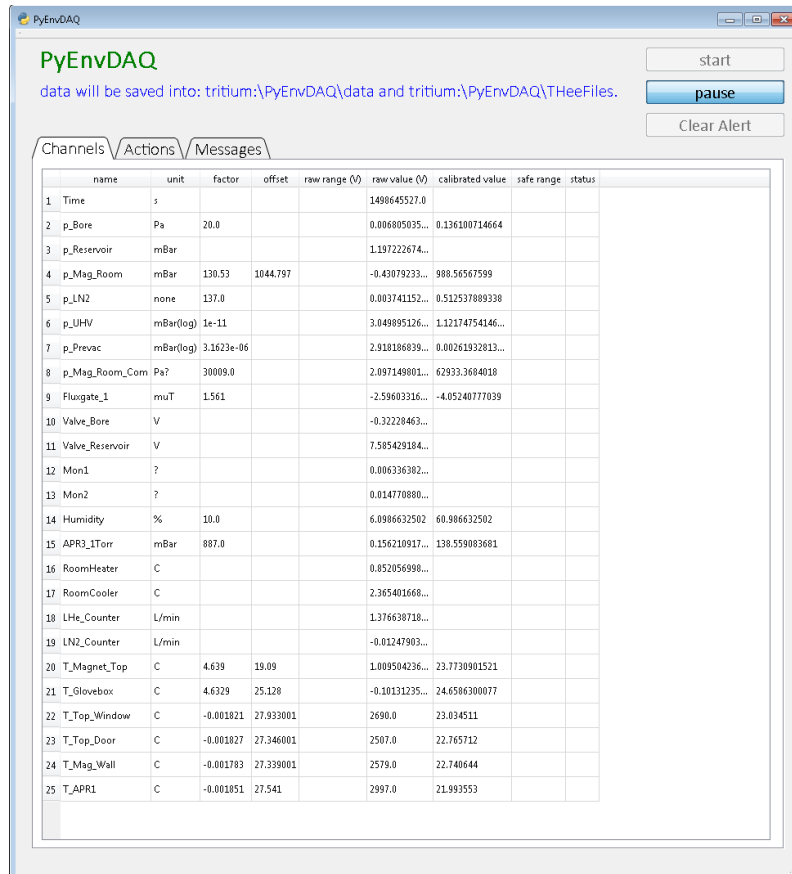


Figure 3.8: The new data acquisition program - “PyEnvDAQ” as described in Section 3.3.1. The program has 3 tabs, or windows. The channels tab displays 25 channels of recorded data including the raw data, its physical unit, calibration factors and the calibrated values. It is also possible to set minimal and maximal ranges for each parameter such that an alarm is sent per email and per Telegram when the measured value gets out of range. The actions tab allows plotting and exporting of the recorded channels. The messages tab shows timestamped alerts for parameters that are outside of their specified ranges.

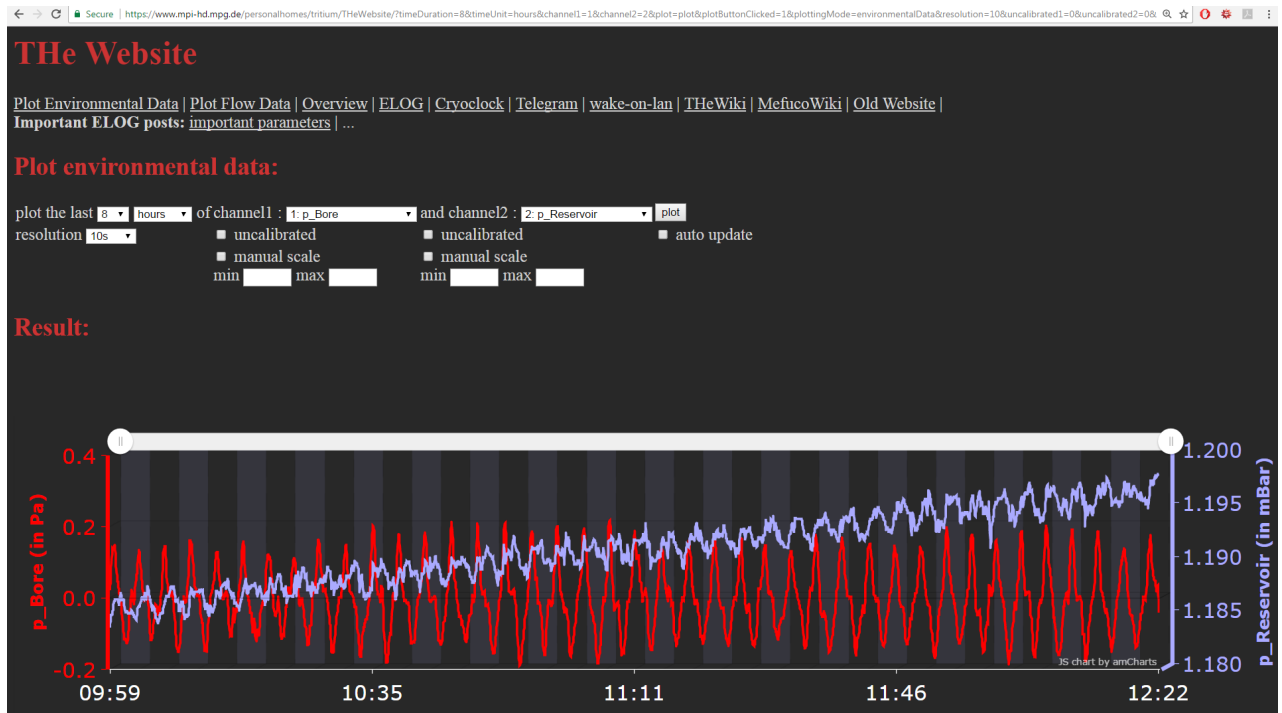


Figure 3.9: The new group website, “The-Website”, as described in Section 3.3.2. “Plot Environmental Data” allows plotting of up to 2 environmental channels simultaneously such as pressure, temperature and magnetic flux. “Plot Flow Data” plots the helium and nitrogen gas flows. “Overview” plots a set of pre-configured plots of important recorded parameters such that the user can get a quick glimpse of the state of the system. The rest are links to other websites.

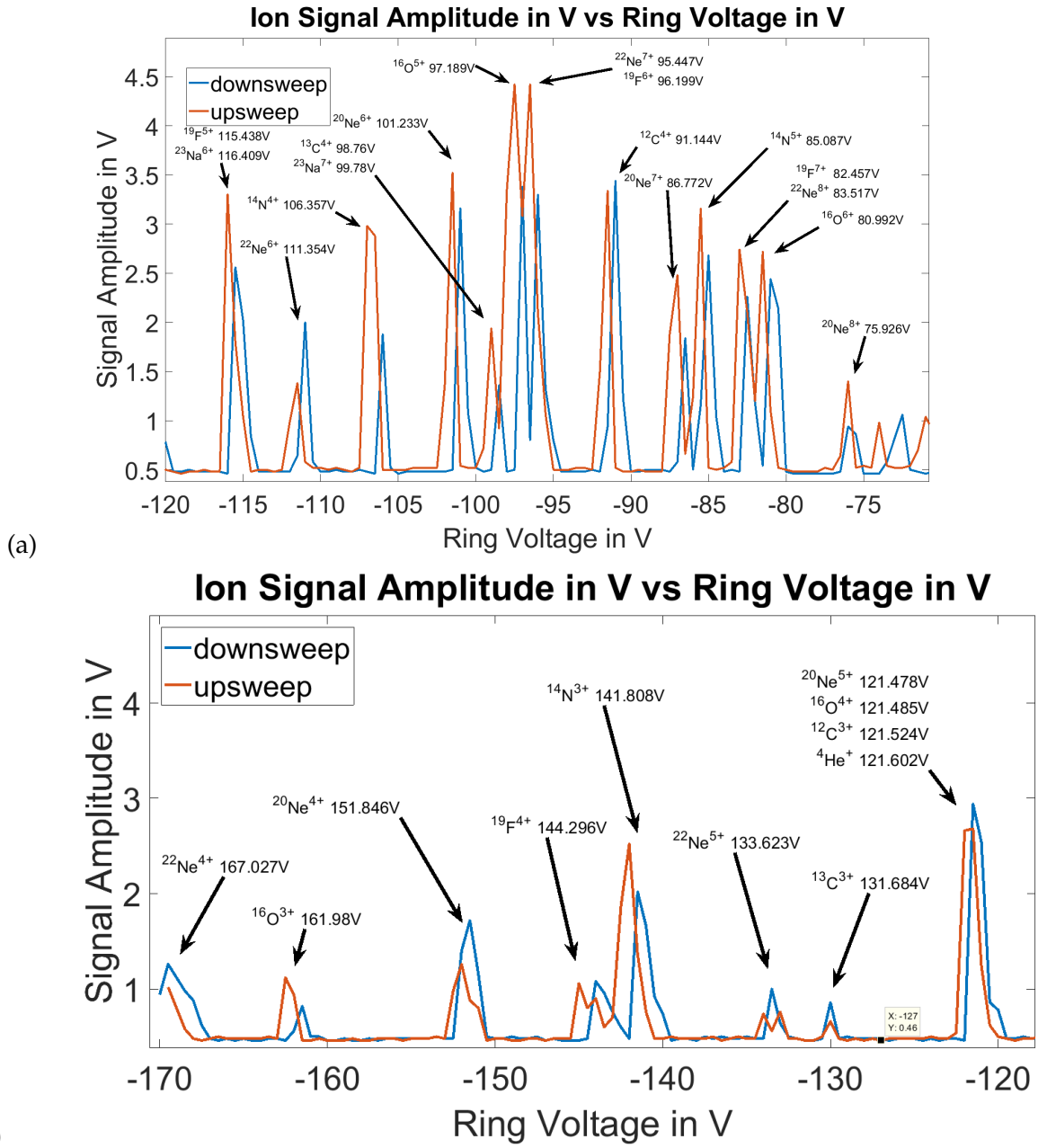


Figure 3.10: A ring voltage scan revealing trappable ion species in THE-Trap: $^1\text{H}^+$ and $^2\text{H}^+$, $^4\text{He}^+$ to $^4\text{He}^{2+}$, $^{12}\text{C}^{2+}$ to $^{12}\text{C}^{4+}$, $^{14}\text{N}^{3+}$ to $^{14}\text{N}^{5+}$, $^{16}\text{O}^{3+}$ to $^{16}\text{O}^{6+}$, $^{19}\text{F}^{4+}$ to $^{19}\text{F}^{7+}$, $^{20}\text{Ne}^{4+}$ to $^{20}\text{Ne}^{8+}$, $^{22}\text{Ne}^{4+}$ to $^{22}\text{Ne}^{8+}$, $^{35}\text{Cl}^{6+}$, $^{35}\text{Cl}^{7+}$ and $^{45}\text{Sc}^{9+}$. To plot the graphs, ions were loaded and the ring voltage was swept while observing the amplitude of the signal coming from the trap. As the ring voltage changes, so does the axial frequency of the ions. When the axial frequency of an ion equals that of the detection circuit, the ion releases its energy in the form of a visible peak. The peaks can be identified with specific ion species using Equation (2.14) and extrapolation from known values such as 91.144V for $^{12}\text{C}^{4+}$. Note that the stable voltage source can only be set between -100V and 0, such that a different voltage source was used to explore the -170V to -100V region. This voltage source can be used to trap the ions but is not stable enough in order to perform precision mass measurements.

is continuously excited using a ≈ 4.1 MHz signal (see Section 2.5.1), producing a constant ≈ 4 MHz ion signal which is detected using the detection circuit, see Section 2.3. The same ≈ 4.1 MHz excitation signal is also mixed with the ≈ 4 MHz ion signal such that signals at ≈ 100 kHz and ≈ 8.1 MHz are produced. These are filtered by a 100 kHz band-pass filter such that only the ≈ 100 kHz component is left. It then gets mixed with another 100 kHz signal, called the mixing signal, to produce signals at ≈ 200 kHz and at DC. These are filtered by a low-pass filter such that only the DC component is left. Setting the phase of the 100 kHz mixing signal properly causes the DC signal to have a dispersion shape with respect to changes in the axial frequency. This DC signal, called the error signal, is integrated, divided and then connected as the ground or “low” of the ring electrode voltage, the “high” being a sum of a fixed DC contribution and the ring modulation signal¹. This creates a feedback loop which keeps the axial frequency constant.

Initially, the mixing down of the 100 kHz signal to DC and its integration were performed by a custom-made box called the “mix2dc box”². After performing the first $^{20}\text{Ne}^{8+}$ measurement the box broke and was replaced with a commercial Zurich Instruments “HF2LI” Lock-In Amplifier, see Figure 3.11. The Lock-In Amplifier mixes the ion signal from 4 MHz straight to DC with no 4.1 MHz or 100 kHz mixing in-between and uses the resulting DC signal as the input for a feedback (PID) circuit. The rest of the circuit remains the same. Unlike the analog mix2dc box, the Lock-In Amplifier is digital. This means its phase is arbitrarily reset whenever one of its parameters is adjusted, such as the mixing frequency, which means that the phase has to be calibrated more often than for the mix2dc box, see Section 4.3.

3.4.2 Detecting the Radial Modes

Unlike the axial mode, which interacts with the detection circuit and leaves a recognizable peak, the radial modes cannot be directly detected. Rather, they are detected indirectly through a change in the axial frequency, or under axial lock a change in the lock error signal. Effects such as relativity, $C_4 \neq 0$ and $B_2 \neq 0$ cause the frequency of each mode to be dependent on the energy of all three modes. Specifically, the axial frequency is dependent on the energy of the modified cyclotron and the magnetron frequencies. Using Equations (2.49), (2.62) and (2.62), it is obtained that the relative axial frequency shift up to second order in A_{\pm}^2 is given by

$$\frac{\Delta\omega_z}{\omega_z} = \left(-\frac{3C_4}{2C_2} + \frac{B_2}{2B_0} \frac{\omega_c}{\omega_z^2} \omega_+ - \frac{\omega_+^2}{4c^2} \right) A_+^2 + \left(-\frac{3C_4}{2C_2} + \frac{B_2}{2B_0} \frac{\omega_c}{\omega_z^2} \omega_- - \frac{\omega_-^2}{4c^2} \right) A_-^2. \quad (3.1)$$

¹ The ring voltage is negative, such that the “high” is actually at most $+100 \mu\text{V}$ and the “low” is negative tens of volts, for instance -90V for $^{12}\text{C}^{4+}$.

² The mixing of the DC and AC components of the ring voltage is done by another custom-made box called the “wing box”, omitted from the drawing, which applies another low-pass filter on the DC component and is capable of switching the “high” of the ring voltage between two voltage sources. At one point during the measurements it broke and a replacement with a similar functionality was internally constructed.

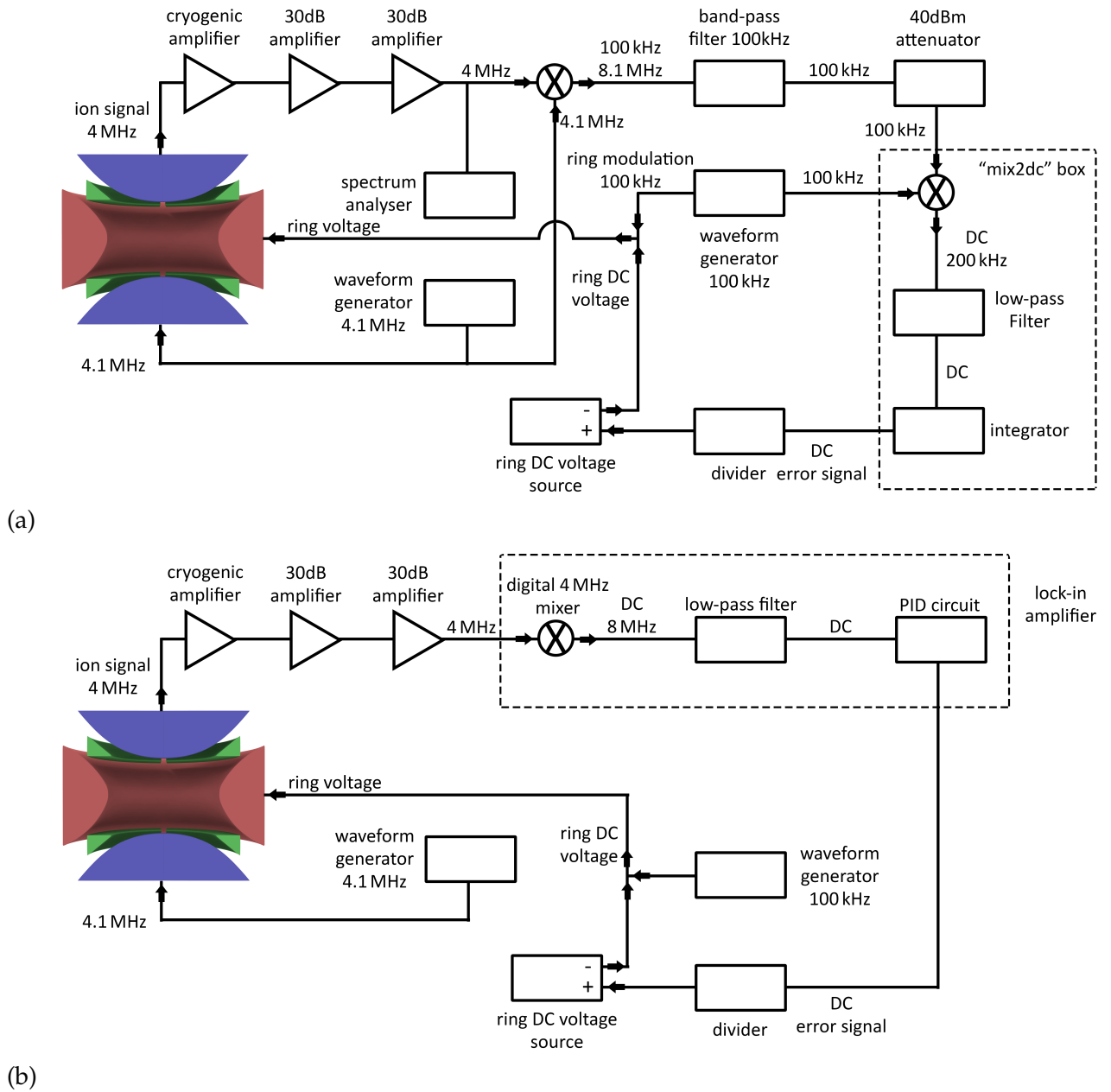


Figure 3.11: (a) The old axial locking circuit with the “mix2dc box”. The ion signal is mixed down from 4 MHz to 100 kHz and then to DC. It is then integrated, divided and set as the ground or “low” of the ring voltage, the “high” being a sum of a fixed DC contribution and the ring modulation signal. This creates a feedback loop which keeps the ring voltage, and so the axial frequency, constant. (b) the new axial locking circuit with the Lock-In Amplifier. The ion signal is mixed down from 4 MHz directly to DC, is amplified, integrated and derivated (PID) as opposed to just integrated, and the attenuation and division factors are different, but effectively the functionality is the same as for (a). See Section 3.4.1 for more details.

Under lock, it is not the axial frequency which is shifted, but the lock error signal. The measurement method for detecting ω_{\pm} involves radially exciting the ion with varying frequencies $\omega_{\text{guess}} - \frac{\Delta\omega}{2} < \omega < \omega_{\text{guess}} + \frac{\Delta\omega}{2}$ via one of the correction electrodes while observing the lock error signal, where ω_{guess} is a guess value for ω_{\pm} and $\Delta\omega$ is the scan width. If the real ω_{\pm} is found inside the scan range, at some point the excitation frequency will be equal to ω_{\pm} and the ω_{\pm} mode will be energized, causing the axial frequency to shift since to lowest order $\frac{\Delta\omega_z}{\omega_z} \propto E_{\pm}$, or rather the lock error signal will shift since the axial frequency is locked. The frequency for which the lock error signal shifts is ω_{\pm} . See Section 4.8 for more details.

NEON MASS MEASUREMENTS

In this chapter the neon mass measurements performed in the context of this thesis are described. In Section ?? the measurement process is elaborated upon. Specifically, in Section 4.1 it is explained how a single ion is loaded into the trap. In Section 4.2 it is shown how pulses exciting the radial modes were used to roughly measure the ion frequencies. In Section 4.3 the process of locking the ion is elaborated upon. In Section 4.4 it is shown how to align the trap. In Section 4.5 the different calibration measurements are explained. In Section 4.8 the measurement method for precisely finding the ion frequencies is shown. In Section 4.9 the calculation of the systematic shifts is explained. In Section 4.10 the data analysis is described. In Section 4.11 the measurement results are shown. Specifically, Sections 4.11.1 and 4.11.2 contain the measurement results for $^{20}\text{Ne}^{8+}$ and $^{22}\text{Ne}^{7+}$, respectively.

4.1 LOADING A SINGLE ION

To prepare a single ion, first many ions are loaded using a FEP voltage of -230 V for $^{12}\text{C}^{4+}$ or -390 V for $^{20}\text{Ne}^{8+}$ and $^{22}\text{Ne}^{7+}$ as explained in Section 3.4. Next, high amplitude (5 Vpp) excitation signals called “brooms” are applied to the lower endcap with frequencies ranging from around twice the magnetron frequency of the ion of interest (several hundred kHz) to about twice the axial frequency of the ion of interest (several MHz), except for a window several tens of kHz wide around the axial frequency of the ion of interest. In this way the axial modes of all ions in the trap except for that of the ion of interest are energized. This causes all ions other than the ion of interest to oscillate at high amplitudes. As a result some collide with the endcaps and exit the trap. The brooms are followed by a reduction in the ring and ring correction voltages (in absolute value) called a “drop” which lasts 10 s. During a drop, the potential well is temporarily shallow, causing energetic ions to exit the trap. Once the ring voltage is restored to its original value, magnetron coupling is performed to de-energize the magnetron mode of the ion of interest, which is excited by the brooms via the $f_z - f_-$ sideband as explained in Section 2.5.2. The axial mode of the ion of interest is then energized with a pulse as explained in Section 2.5.2. The resulting signal picked up by the amplifier shows several peaks in case there are many ions left or a single peak in case there are few ions or a single ion left. The sequence of brooms, drop, magnetron coupling and axial excitation are repeated with the drop voltages decreasing (in absolute value) from a few negative volts to a few negative tens of mV until the axial excitations show a single peak. There are then several ways to verify whether there is a single ion left in the trap:

An “Ion dip measurement” can be performed by continuously exciting the axial mode as explained in Section 2.5.2 while recording and averaging the resulting ion signal. The existence

of additional ions can be verified or excluded by measuring the damping term, which is the width of the resulting dip, see Section 2.3.4. Alternatively, the stability of the axial lock can be observed. When several ions are present in the trap, they apply forces on each other, causing energy exchange between one another. Abrupt shifts in the error signal are observed as a result. In addition, the “ring/correction ratio”, also called the “trap orthogonality constant” or the “tuning ratio” can be measured. In the case of THe-Trap, a change in the ring voltage of 1 mV requires a change of 750 mV in the correction electrodes voltage in order to keep the error signal constant. In the presence of several ions the potential seen by the ion of interest changes and as a result the $\Delta V_{\text{corr}}/\Delta V_{\text{ring}}$ ratio changes by about a factor of 1/2. However, even if all tests are consistent with having a single ion, it is still possible that there are additional ones with radii and energies so large that they do not affect the ion of interest. Such ions might de-energize over days or weeks and then become detectable.

Loading the trap creates “patch potentials” which are charges trapped on the surfaces of the trap. Patch potentials shift the minimal drop voltage required to get a single ion, the calibration parameters (see Section 4.5) and the “magic ring correction voltage” (see Section 4.8), such that the calibration measurements need to be manually repeated between loadings. This is the main source of systematic uncertainty in the measurement as explained in Section 4.11.

4.2 PULSING THE RADIAL MODES TO ROUGHLY DETERMINE THE ION FREQUENCIES

In Section 4.1 the trap voltages were adjusted to determine the axial frequency to within 2 Hz. Next, a rough value for the magnetron frequency is found using magnetron excitation pulses. A magnetron pulse is applied, typically at an amplitude of 5 V and a duration of 10 ms. Then, coupling is performed as explained in Section 2.5.2. If an ion signal is observed, it can be concluded that the magnetron pulse successfully energized the magnetron mode. The cycle of magnetron pulse and magnetron coupling is then repeated while gradually changing the magnetron pulse frequency, lowering its amplitude to around 100 mV and increasing its duration to around 1 s. In this way the magnetron frequency is determined to within 1 Hz. Next the modified cyclotron frequency is found using the same method with cyclotron pulses and cyclotron coupling using a starting value calculated using Equation (2.10).

4.3 LOCK PHASE CALIBRATION AND LOCKING THE ION

Once there is a single ion in the trap, the axial frequency has been set to be the resonance frequency of the tuned circuit within 2 Hz and the magnetron mode has been de-energized, locking is established as explained in Section 3.4.1. First the phases of the lock-related signals are calibrated by fixing the mix2dc or LIA error signal and measuring the resulting ion signal as a function of the phases of the lock-related signals, see Figure 4.1. In the case of the mix2dc box, these are the two 100 kHz mixing signals and the 4.1 MHz excitation signal. In the case of the LIA, these are the LIA 4 MHz mixing signal and the 4.1 MHz excitation signal. A second-degree polynomial fit is applied to find the phases for which the ion signal amplitude is maximal.

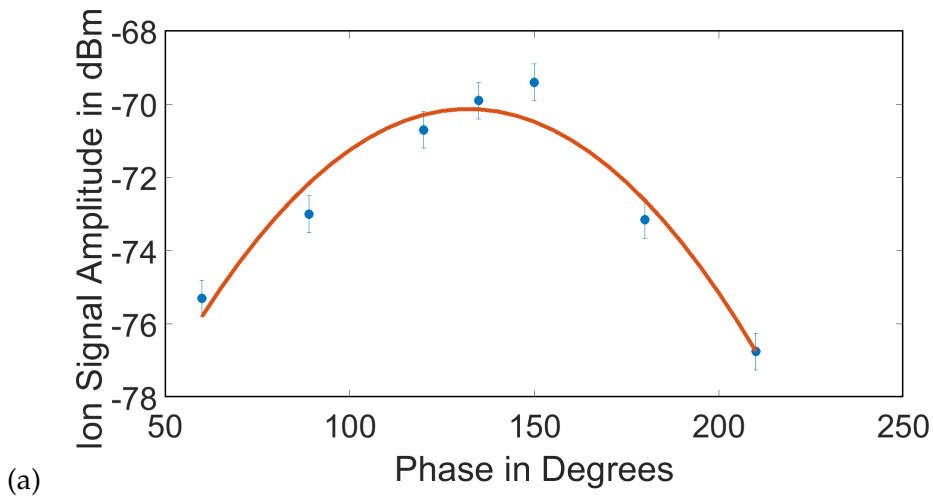


Figure 4.1: Lock Phase Calibration Measurements. The ion signal amplitude is maximized by tuning the phases of the lock-related signals as explained in Section 4.3.

Once the phases have been calibrated, the error signal is set to be no longer fixed, and in the case of the LIA the PID feedback parameters are then automatically tuned by the LIA's control program. At this point the ion is locked but at an arbitrary error signal value. The ring voltage is then modified in steps of $1 \mu\text{V}$ until the error signal is zero, which means that the axial frequency has been determined to within the noise of the detection circuit and the voltage source, which is a few μV or a few 100 mHz.

4.4 ALIGNING THE TRAP

Once axial locking has been established the trap can be aligned to be perpendicular to \vec{B} . The process of alignment involves tilting the trap in steps using an xy displacement and tilting stage connected to the trap tower (see Section 3.2) and observing the resulting axial frequency, which is maximal when the trap is aligned. Initially the steps cause large changes in the axial frequency such that it is roughly measured using axial excitation pulses. The final steps cause smaller changes which can be measured while the ion is locked for fine tuning. The trap can be aligned with a precision of about $\delta\theta = 0.1^\circ$ using this method. In practice, the trap tilt is negligible due to the use of the invariance theorem, see Equation (2.8), for the determination of f_c [36].

4.5 RADIAL AND AXIAL CALIBRATION MEASUREMENTS

Once the phases of the lock-related signals are calibrated and ion locking is achieved, radial and axial calibration measurements are performed. These calibration measurements are used for determining the C_4 , C_6 , B_2 , relativistic and sweep fit systematic shifts (see Section 2.6), see Section 4.8. The calibration results are given in Table 4.1.

4.6 MAGNETRON AND MODIFIED CYCLOTRON CALIBRATION MEASUREMENTS

In the modified cyclotron and magnetron calibration measurements, the dependency of the axial frequency on the energy in the radial modes is measured, see Figure 4.2. The ring correction voltage for which the axial frequency is the least dependent on the pulse amplitude is found, along with their scaling factor, both of which are needed to calculate the systematic shifts mentioned above. This is done by de-energizing the radial modes, locking the ion, measuring the average error signal, exciting the respective radial mode using a pulse, re-locking the ion and measuring the average error signal again¹. The measured difference in error signal corresponds to the axial frequency shift caused by the respective radial mode being energized. The process is repeated for different pulse energies. Specifically, the pulse duration is kept constant at 50 ms for the magnetron excitation or 65 ms for the modified cyclotron excitation. As discussed in more detail below, the relative error signal change scales linearly with the square and quadrature of the pulse amplitude. As a result the measurement is fitted to $y = ax^2 + bx^4$, where x and y are the pulse amplitude and the error signal shift, respectively. The measurement is then repeated for different correction electrode voltages and linearly fitted such that $y = cx + d$, where x and y are the ring correction electrode voltage and the a parameter from the previous fit, respectively. The average b parameter, the ring correction electrode voltage for which $a = 0$ and the c parameter are used to calculate the systematic shifts mentioned above.

Specifically, for the magnetron mode, the relative axial frequency shift due to a change in the magnetron amplitude up to fourth order is given by the C_4 and C_6 shifts (see Section 2.6.1.1)²:

$$\frac{\Delta\omega_z}{\omega_z} = -\frac{3C_4}{2C_2}A_-^2 + \frac{45C_6}{16C_2}A_-^4, \quad (4.1)$$

The relative change in the axial frequency is expressed using a linear approximation of Equation (2.14):

-
- 1 The error signal for the de-energized state is measured multiple times in order to minimize ring voltage fluctuation effects.
 - 2 The relativistic and B_2 shifts were neglected. For example, the absolute values of the A_-^2 coefficients for the first $^{12}\text{C}^{4+}$ measurement (see Section 4.11) are about 1.5 , $5 \cdot 10^{-2}$ and $8 \cdot 10^{-6}$ for the C_4 , B_2 and relativistic shifts, respectively.

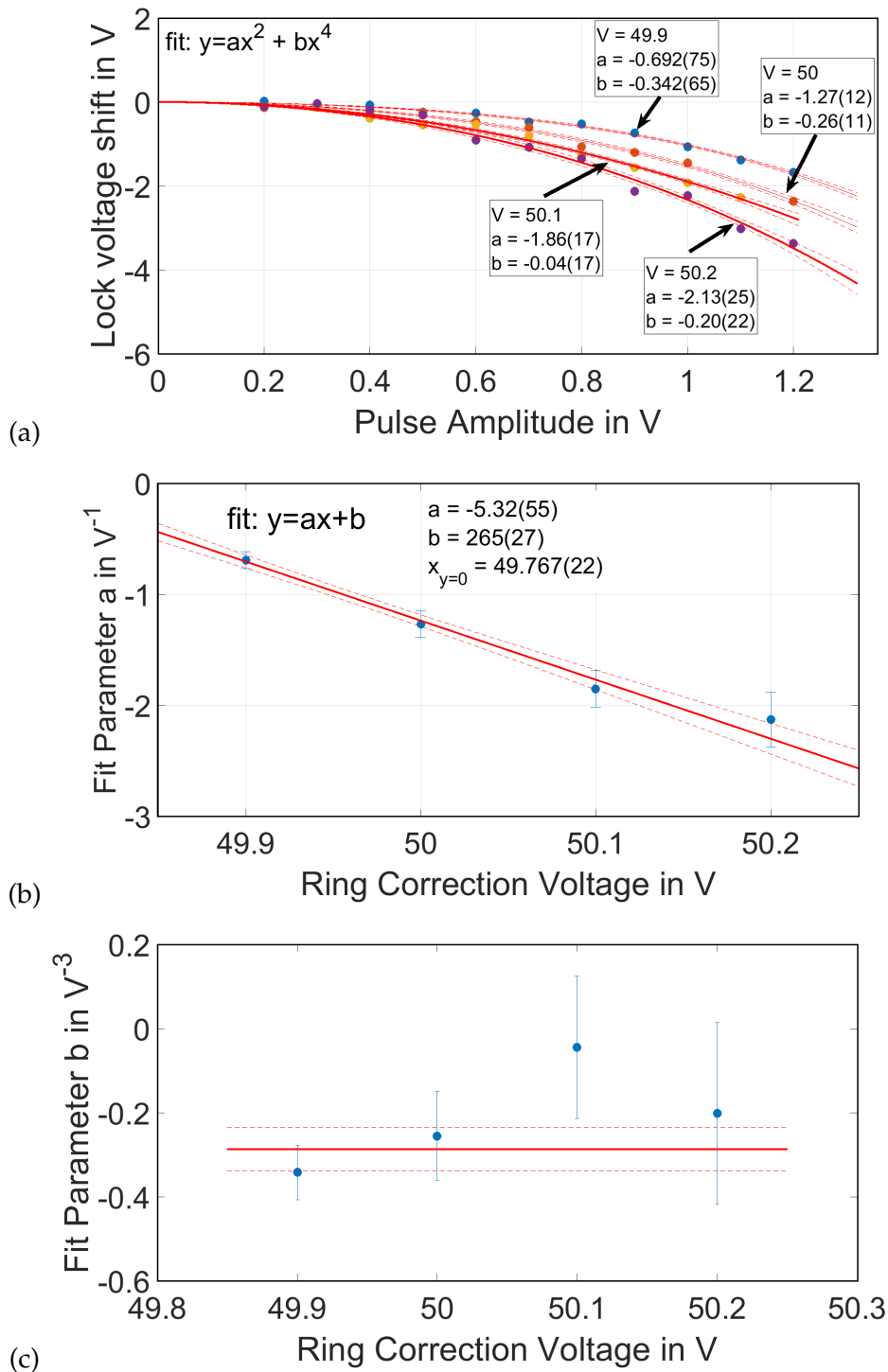


Figure 4.2: Magnetron and modified cyclotron calibration Measurements. (a) One of the radial modes is energized with pulses of different amplitudes and the corresponding lock voltage shift is measured and fit. The measurement is repeated for different correction voltages. (b) the a parameter from each fit in (a) is linearly fit to find the correction voltage for which $a = 0$. (c) The b parameter from each fit is averaged to arrive at the value for b . These parameters are necessary for calculating certain systematic shifts, see Section 4.7.

$$\frac{\Delta\omega_z}{\omega_z} = \frac{\Delta V_{\text{ring}}}{2V_{\text{ring}}}. \quad (4.2)$$

The ring voltage change ΔV_{ring} is expressed as the lock correction voltage change divided by the calibration factor $V_{\text{lock cal}}$ (see Section 3.4.1):

$$\Delta V_{\text{ring}} = -\frac{\Delta V_{\text{lock}}}{V_{\text{lock cal}}}, \quad (4.3)$$

such that the relative change in axial frequency is given by

$$\frac{\Delta\omega_z}{\omega_z} = -\frac{\Delta V_{\text{lock}}}{2V_{\text{ring}}V_{\text{lock cal}}}. \quad (4.4)$$

The magnetron, axial and modified cyclotron amplitudes A_+ , A_z and A_+ can be related to the pulse amplitudes and durations by the use of the calibration constants $A_{\text{cal } +}$, $A_{\text{cal } z}$ and $A_{\text{cal } +}$ respectively:

$$A_{+/z/-} = A_{\text{cal } +/z/-} A_{\text{pulse}} t_{\text{pulse}}. \quad (4.5)$$

Substitution of Equations (2.44), (2.45), (4.4) and (4.5) into Equation (4.1) yields the relation between the change in lock voltage and the pulse amplitude

$$\Delta V_{\text{lock}} = a_{\text{mag}} \cdot A_{\text{pulse}}^2 t_{\text{pulse}}^2 + b_{\text{mag}} \cdot A_{\text{pulse}}^4 t_{\text{pulse}}^4, \quad (4.6)$$

where

$$a_{\text{mag}} \equiv \frac{6q\Delta V_{\text{CE}} C_{\text{CE},4,0} V_{\text{ring}} V_{\text{lock cal}}}{m\omega_z^2} A_{\text{-cal}}^2 \quad (4.7)$$

and

$$b_{\text{mag}} \equiv -\frac{45qC_6 V_{\text{ring}} V_{\text{lock cal}}}{4m\omega_z^2} A_{\text{-cal}}^4 \quad (4.8)$$

are determined from the fit in Figure 4.2(a). In Figure 4.2(b) a_{mag} is fit as a function of the correction voltage ΔV_{CE} . The curvature c_{mag} is given by

$$c_{\text{mag}} \equiv \frac{6qC_{\text{CE},4,0} V_{\text{ring}} V_{\text{lock cal}}}{m\omega_z^2} A_{\text{-cal}}^2 \quad (4.9)$$

and the intersection point with the horizontal axis occurs at $V_{CE} = V_{\text{mag}}$, which is V_0 from Figure 4.2(b) and is the correction voltage for which the axial frequency is the least dependent on the magnetron energy. In Figure 4.2(c) b_{mag} is fit, which allows $A_{-\text{cal}}$ and C_6 to be calculated using

$$A_{-\text{cal}} = \sqrt{\frac{c_{\text{mag}} m \omega_z^2}{6q C_{CE,4,0} V_{\text{lock cal}} V_{\text{ring}}}} \quad (4.10)$$

and

$$C_6 = -\frac{4m\omega_z^2 b_{\text{mag}}}{45q A_{-\text{cal}}^4 V_{\text{ring}} V_{\text{lock cal}}}. \quad (4.11)$$

$A_{-\text{cal}}$, C_6 and V_{mag} are necessary for calculating the C_4 , C_6 and relativistic systematic shifts. The relative axial frequency shift due to a change in the modified cyclotron amplitude is given by

$$\frac{\Delta\omega_z}{\omega_z} = -\frac{3C_4}{2C_2} A_+^2 + \frac{45C_6}{16C_2} A_+^4 + \frac{B_2}{2B_0} \frac{\omega_c \omega_+}{\omega_z^2} A_+^2 - \frac{\omega_+^2}{4c^2} A_+^2, \quad (4.12)$$

which in comparison to Equation (4.1) also includes the B_2 and relativistic shifts as they are not negligible. Substitution of Equations (2.44), (2.45), (4.4) and (4.5) into Equation (4.6) yields the relation between the change in lock voltage and the pulse amplitude

$$\Delta V_{\text{lock}} = a_{\text{cyc}} \cdot A_{\text{pulse}}^2 t_{\text{pulse}}^2 + b_{\text{cyc}} \cdot A_{\text{pulse}}^4 t_{\text{pulse}}^4, \quad (4.13)$$

where

$$a_{\text{cyc}} \equiv -2V_{\text{ring}} V_{\text{lock cal}} \left(-\frac{3q\Delta V_{CE} \cdot C_{CE,4,0}}{m\omega_z^2} + \frac{B_2\omega_c\omega_+}{2B_0\omega_z^2} - \frac{\omega_+^2}{4c^2} \right) A_{+\text{cal}}^2 \quad (4.14)$$

and

$$b_{\text{cyc}} \equiv -\frac{45q V_{\text{ring}} V_{\text{lock cal}} A_{+\text{cal}}^4 C_6}{4m\omega_z^2} \quad (4.15)$$

are determined from the fit in Figure 4.2(a). In Figure 4.2(b) a_{cyc} is linearly fit to the correction voltage, from which the curvature c_{cyc} is obtained:

$$c_{\text{cyc}} \equiv \frac{6q V_{\text{ring}} V_{\text{lock cal}} C_{CE,4,0} A_{+\text{cal}}^2}{m\omega_z^2}. \quad (4.16)$$

The intersection point with the horizontal axis gives

$$B_2 = \frac{B\omega_z^2}{2c^2} + \frac{6\Delta V_{CE} \cdot C_{CE,4,0}}{\omega_+} \quad (4.17)$$

and occurs at $V_{CE} = V_{cyc}$, which is V_0 from Figure 4.2(b) and is the correction voltage for which the axial frequency is the least dependent on the modified cyclotron energy. In Figure 4.2(c) b_{cyc} is fit, which allows A_{+cal} and C_6 to be calculated using

$$A_{+cal} = \sqrt{\frac{c_{cyc} m \omega_z^2}{6 \cdot C_{CE,4,0} q V_{lock cal} V_{ring}}} \quad (4.18)$$

$$\text{and } C_6 = -\frac{4m\omega_z^2 b_{cyc}}{A_{+cal}^4 45q V_{ring} V_{lock cal}}, \quad (4.19)$$

which together with B_2 and V_{cyc} are necessary for calculating the C_4, C_6 , relativistic and B_2 systematic frequency shifts (see Section 2.6).

4.7 AXIAL CALIBRATION MEASUREMENTS

In the axial calibration measurement, the dependency of the axial frequency on the energy in the axial mode is determined, see Figure 4.3. Unlike for the radial modes, pulses cannot be used as the axial mode is continuously excited by the 4.1 MHz excitation signal and de-energized by the tuned circuit. Thus, the error signal shift is measured as a function of the amplitude of the 4.1 MHz excitation signal. This is done by measuring the average error signal as a function of the the 4.1 MHz excitation signal amplitude. The measured difference in error signal corresponds to the axial frequency shift caused by the energy in the axial mode. Unlike for the magnetron and modified cyclotron calibration measurements, the error signal shifts observed are too small in order to measure the second order shift, which is proportional to A_z^4 . Therefore the measurement is fitted to the function $y = a_{axial} (x^2 - 1^2)$, where x and y are the 4.1 MHz excitation signal amplitude and the error signal shift, respectively. The fit function compensates for the error signal shift caused by the default excitation signal amplitude of 1 V by the use of the -1^2 component. The measurement is then repeated for different correction electrode voltages, and the resulting measurement is fitted to $y = b_{axial}x + c_{axial}$, where x and y are the ring correction electrode voltage and a_{axial} , respectively. The b_{axial} parameter is used to calculate the systematic shifts mentioned above.

The relative axial frequency shift due to a change in the axial amplitude up to fourth order is given by the C_4 and C_6 shifts, see Section 2.6.1.1³:

³ The relativistic shift was neglected. For example, the absolute values of the A_z^2 coefficients for the first $^{12}\text{C}^{4+}$ measurement (see Section 4.11) are about 1.5 and $1 \cdot 10^{-3}$ for the C_4 and relativistic shifts, respectively.

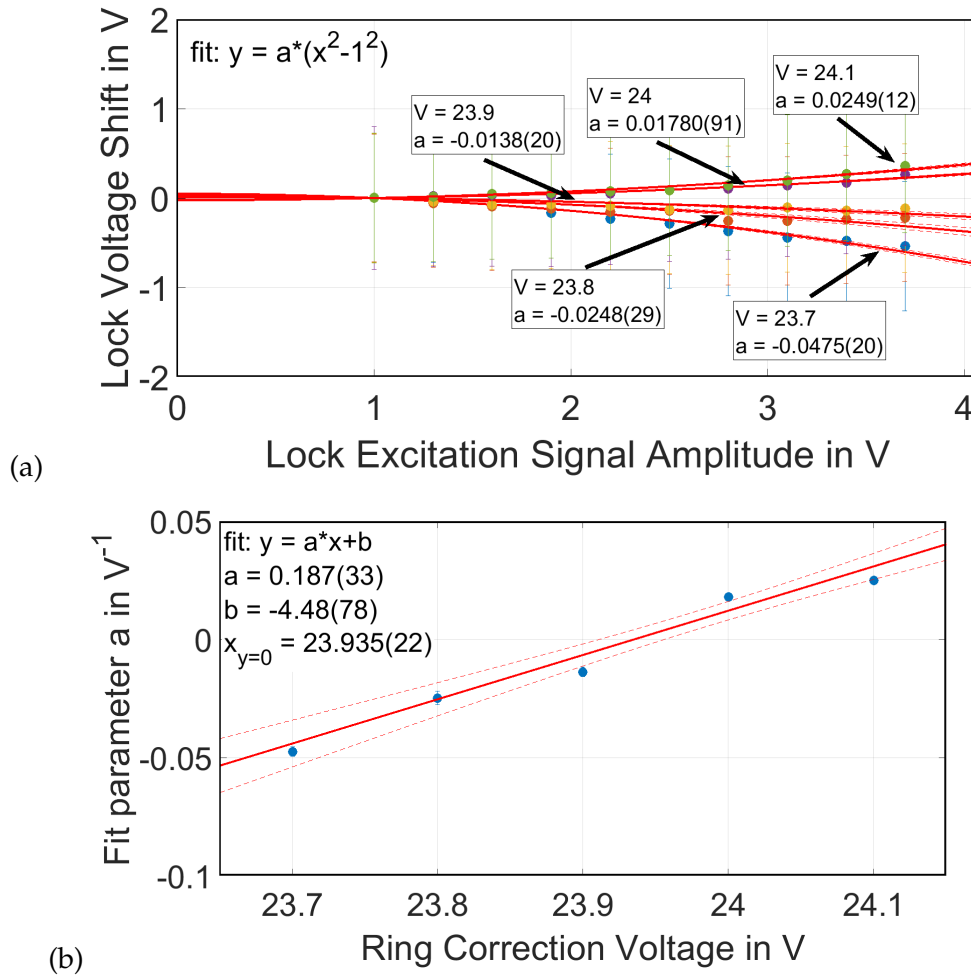


Figure 4.3: Axial Calibration Measurements. (a) The 4.1 MHz signal continuously exciting the axial mode is set to different amplitudes and the corresponding lock voltage shift is measured and fit. The measurement is then repeated for different correction voltages. (b) the a parameter from each fit in (a) is linearly fit to find the correction voltage for which $a = 0$. These parameters are necessary for calculating certain systematic shifts.

$$\frac{\Delta\omega_z}{\omega_z} = \frac{3C_4}{4C_2}A_z^2 + \frac{45C_6}{48C_2}A_z^4. \quad (4.20)$$

Substitution of Equations (2.44) , (2.45) , (4.4) and the axial mode version of (4.5):

$$A_z = A_{z\text{cal}}A_{4.1\text{MHz}} \quad (4.21)$$

into Equation (4.1) yields the relation between the change in lock voltage and the pulse amplitude

$$\Delta V_{\text{lock}} \approx a_{\text{axial}} \cdot A_{4.1\text{MHz}}^2, \quad (4.22)$$

where

$$a_{\text{axial}} \equiv 2V_{\text{ring}}V_{\text{lock cal}} \frac{3q\Delta V_{\text{CE}} \cdot C_{\text{CE},4,0}}{m\omega_z^2} A_{z\text{cal}}^2 \quad (4.23)$$

is determined from the fit in Figure 4.3(a). In Figure 4.3(b) a_{axial} is linearly fit to the correction voltage. The curvature b_{axial} is given by

$$b_{\text{axial}} \equiv -\frac{3qV_{\text{ring}}V_{\text{lock cal}}C_{\text{CE},4,0}A_{z\text{cal}}^2}{m\omega_z^2}, \quad (4.24)$$

such that $A_{z\text{cal}}$ is given by

$$A_{z\text{cal}} = \sqrt{-\frac{b_{\text{axial}}m\omega_z^2}{3C_{\text{CE},4,0}qV_{\text{lock cal}}V_{\text{ring}}}}. \quad (4.25)$$

The intersection point with the horizontal axis occurs at $V_{\text{CE}} = V_{\text{axial}}$, which is V_0 from Figure 4.2(b) and is the correction voltage for which the axial frequency is the least dependent on the axial energy. $A_{z\text{cal}}$ is necessary for calculating the C_4 , relativistic and B_2 systematic shifts (see Section 2.6).

4.8 THE MEASUREMENT METHOD - "SWEEPS"

The measurement method, called "sweeps", is based on using the unharmonicities of the electrostatic potential, which cause the frequencies of the three different modes of motion

Table 4.1: Calibration Measurements

	V_{mag}	b_{mag}	c_{mag}	b_{axial}	V_{cyc}	b_{cyc}	c_{cyc}
$^{12}\text{C}^{4+}$	-39.3936(51)	-0.868(65)	29.24(87)	2.75(28)	-39.3242(22)	-5.14(12)	66.74(86)
$^{20}\text{Ne}^{8+}$	-30.6683(49)	-1.135(40)	29.8(13)	2.51(26)	-30.5959(23)	-2.84(10)	44.95(59)
$^{12}\text{C}^{4+}$	-37.7213(70)	-0.349(32)	4.84(18)	0.476(50)	-37.7009(76)	-0.591(69)	6.47(20)
$^{20}\text{Ne}^{8+}$	-25.8199(51)	-0.595(27)	5.02(14)	0.187(33)	-25.743(67)	-0.453(54)	5.0(1.5)
$^{12}\text{C}^{4+}$	-49.767(22)	-0.287(51)	5.32(55)	0.446(23)	-49.600(38)	-0.210(56)	4.83(56)
$^{20}\text{Ne}^{8+}$	-34.0753(50)	-0.173(38)	5.20(21)	0.146(70)	-34.0036(44)	-0.203(22)	5.21(34)
$^{12}\text{C}^{4+}$	-41.11(3)	-0.187(38)	4.3(14)	0.250(33)	-40.87(0.14)	-0.58(17)	7.3(20)
$^{22}\text{Ne}^{7+}$	-40.369(14)	-0.355(36)	5.10(36)	0.201(82)	-40.2654(77)	-0.874(30)	7.07(80)

Calibration Measurements Results for the three $^{20}\text{Ne}^{8+}$ measurements and for the $^{22}\text{Ne}^{7+}$ measurement as explained in Section 4.5. The magnetron and modified cyclotron pulse durations are $t_{\text{pulse mag}} = 65$ ms and $t_{\text{pulse cyc}} = 50$ ms. V_{mag} and V_{cyc} are in V, b_{mag} and b_{cyc} are in V^{-3} , c_{mag} and c_{cyc} are in V^{-2} and b_{axial} is in V^{-1} . The c_{mag} , b_{axial} , b_{cyc} and c_{cyc} values for the first measurement pair of $^{12}\text{C}^{4+}$ and $^{20}\text{Ne}^{8+}$ are about an order of magnitude larger than for the other measurements as they were measured while the "mix2dc box" was still in use, where the lock signal was about 9 times weaker compared to the later measurements where the Lock-In Amplifier was used. Their a_{axial} values are extrapolated based on older measurements [50].

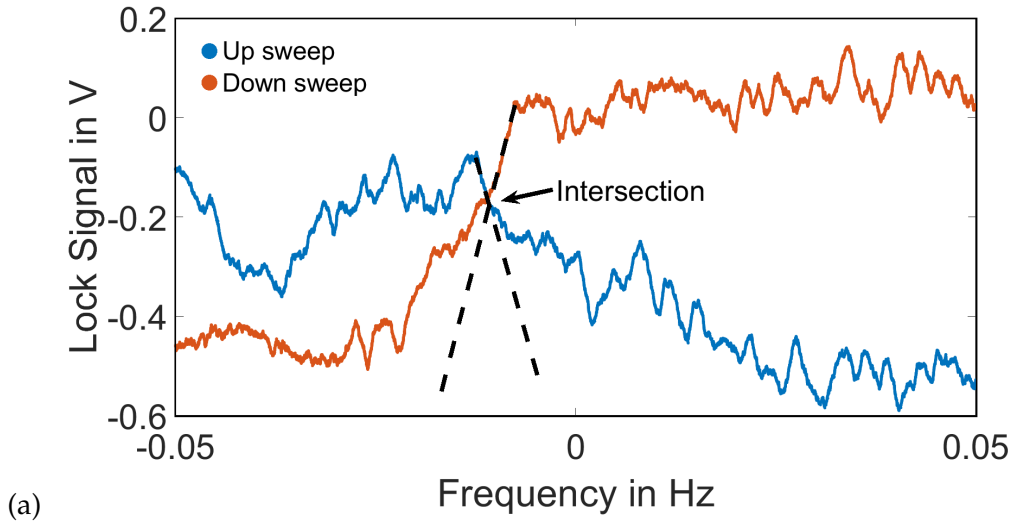


Figure 4.4: The measurement method - “sweeps”. One of the radial modes, the modified cyclotron or the magnetron, is excited with a signal of a changing frequency. Once the frequency of the excitation signal approaches that of the respective radial mode, it is energized, causing the error signal to shift. The measurement is repeated while scanning the frequency of the excitation signal in the opposite direction. The intersection point of the fitted region of both measurements corresponds to the frequency of the respective mode [64].

to be dependent on the energy of the other two modes. Specifically, the axial frequency is shifted when the modified cyclotron or the magnetron modes are energized. Due to the axial frequency being locked, this means that the axial frequency stays constant but the error signal shifts. In the sweeps method an excitation signal is applied to one of the correction electrodes. Its frequency is scanned, or swept, across a range of frequencies centered around an initial guess for the corresponding radial mode which is obtained using a rough measurement using pulses, see Section 4.2. The error signal is observed during the excitation. If the actual radial frequency is found in the range of the sweep, the error signal will shift during the sweep. The sweep is then repeated in the other direction and the intersection of the two graphs is used to determine the radial frequency, compare Figure 4.4. The sweeps are analysed using a Python program written by [47]. The measurement uncertainty can be reduced by making the two sweep directions more symmetric. This can be achieved by selecting the ring correction voltage for which $a_{\text{cyc}} = 0$ such that the anharmonicities cancel each other up to first order in the modified cyclotron mode energy⁴. This ring correction voltage is called the “magic ring correction voltage” and is given by summing the C_4 (Equation (2.50)) and relativistic (Equation (2.54)) shifts for the modified cyclotron mode to zero, yielding

⁴ The sweeps are made symmetric for the modified cyclotron mode and not for the magnetron mode as it is the modified cyclotron mode which needs to be measured with lower uncertainty.

Table 4.2: Sweep Measurements

	V_{ring} in V	V_{CE} in V	f_- in kHz	f_z in MHz	f_+ in MHz	f_{cyc} in MHz
$^{12}\text{C}^{4+}$	90.861010(1)	39.630(1)	283.697477(1)	4.057019	29.008733411(1)	29.292430794(3)
$^{20}\text{Ne}^{8+}$	75.629660(1)	30.236(1)	235.606332(1)	4.057019	34.9298903081(6)	35.165496618 (4)
$^{12}\text{C}^{4+}$	90.707052(1)	37.438(1)	283.694610(3)	4.057000	29.008734516(2)	29.292429239(4)
$^{20}\text{Ne}^{8+}$	75.408014(1)	25.300(1)	235.603912(6)	4.057000	34.929890652(2)	35.165494754(4)
$^{12}\text{C}^{4+}$	91.632730(1)	49.900(1)	285.669863(7)	4.070940	29.006756536(4)	29.292423686(6)
$^{20}\text{Ne}^{8+}$	76.184490(1)	33.900(1)	237.370036(4)	4.072060	34.928119533(3)	35.165488100(4)
$^{12}\text{C}^{4+}$	91.333680(1)	40.812(1)	285.412522(4)	4.069130	29.007012864(4)	29.292423531(6)
$^{22}\text{Ne}^{7+}$	95.595590(1)	41.500(1)	299.176547(4)	4.069130	27.672497074(3)	27.971671766(4)

Sweep Measurements Results for the three $^{20}\text{Ne}^{8+}$ measurements and for the $^{22}\text{Ne}^{7+}$ measurement as explained in Section 4.5 along with the ring and ring correction voltages. The axial frequency f_z is assumed to have zero uncertainty as the uncertainty is already taken into account via the uncertainties of the lock-related shifts, see Table 4.3. The axial frequency changes between measurements as the tuned circuit drifts and is adjusted from time to time in order to keep the ion exactly at its center.

$$\Delta V_{\text{CE}} = V_{\text{magic}} - V_{\text{mag}} = -\frac{\omega_+^3 B_0}{3c^2 C_{\text{CE},4,0}}. \quad (4.26)$$

The anharmonicities shift the up and down sweeps by different amounts, such that there is a net shift called power broadening, or "fit shift". Power broadening has been experimentally confirmed to be minimal and at most 2 mHz when using the "magic ring correction voltage" [50], and as such a systematic uncertainty of 2 mHz was added to the three $^{12}\text{C}^{4+}$ measurements using it. However, unlike for $^{12}\text{C}^{4+}$, setting the ring correction voltage to the "magic ring correction voltage" value did not seem to make the $^{20}\text{Ne}^{8+}$ or the $^{22}\text{Ne}^{7+}$ modified cyclotron sweeps symmetric. Seeing how the C_4 , relativity and B_2 -related parameters are all of the same order of magnitude for $^{12}\text{C}^{4+}$, $^{20}\text{Ne}^{8+}$ and $^{22}\text{Ne}^{7+}$ (see Table 4.3) the cause for this is unclear. Therefore the ring correction voltage was tuned for the neon ions manually instead. The difference in frequency values between the up and the down sweeps has been found to be smaller for most neon ions than for the carbon ions, such that the power broadening is not expected to be significantly larger for the neon ions than for the carbon ions. Despite that, a probably over-estimated systematic uncertainty of 10 mHz, five times that for $^{12}\text{C}^{4+}$, was added to all other measurements in order to be on the safe side, see "Fit" in Table 4.3. The frequency measurement results are given in Table 4.2

Table 4.3: Systematic Shifts Results

	$^{12}\text{C}^{4+}$	$^{20}\text{Ne}^{8+}$	$^{12}\text{C}^{4+}$	$^{20}\text{Ne}^{8+}$	$^{12}\text{C}^{4+}$	$^{20}\text{Ne}^{8+}$	$^{12}\text{C}^{4+}$	$^{22}\text{Ne}^{7+}$
C_4	17(20)	18(23)	27(33)	13(16)	25(31)	10(17)	14(18)	11(16)
C_6	0.03(4)	0.03(3)	0.12(14)	0.02(2)	0.07(8)	0.005(5)	0.03(3)	0.03(4)
Rel.	-4(7)	-4(7)	-6(11)	-3(5)	-5(10)	-2(4)	-3(6)	-2(4)
IC	-313(4)	-522(7)	-313(4)	-522(5)	-313(4)	-513(7)	-313(4)	-574(8)
B_2	-12(4)	-9(3)	-5(3)	-7(3)	-42(19)	-5(3)	-35(24)	-12(8)
C_1B_1	0(173)	0(207)	0(173)	0(208)	0(172)	0(206)	0(172)	0(164)
Phase	0(41)	0(166)	0(41)	0(166)	0(42)	0(166)	0(42)	0(127)
Mod	-276(14)	-272(14)	-323(17)	-320(16)	-319(16)	-316(16)	-320(16)	-322(17)
Offset	-0.8(2)	-1.4(3)	-0.8(1)	-1.4(3)	-0.8(2)	-1.4(3)	-0.8(2)	-1.5(3)
B Drift	-422(149)	0(0)	-129(329)	0(0)	-130(472)	0(0)	-369(587)	0(0)
Fit	0(68)	0(284)	0(68)	0(284)	0(341)	0(284)	0(68)	0(358)
Coil	0(40)	0(40)	0(40)	0(40)	0(40)	0(40)	0(40)	0(40)
Total	167(247)	790(393)	492(385)	840(392)	526(613)	836(391)	1027(619)	902(416)

Systematic shifts results for the three $^{20}\text{Ne}^{8+}$ measurement runs and for the $^{22}\text{Ne}^{7+}$ measurement run as explained in Section 2.6. All shifts are given as relative shifts in ppt. Rel. stands for relativity, IC for image charge, Phase for the lock phase, Mod for the ring modulation shift, offset for the lock DC offset, Fit for the sweep fit and Coil for the coil pushing. The B temporal shift should be added to the measured f_{cyc} , where the other shifts are “already included” in it and should therefore be subtracted. The “total” is therefore the B temporal shift minus all the rest.

4.9 CALCULATING THE SYSTEMATIC SHIFTS

Following the calibration measurements and the sweep measurements, the systematic shifts were calculated in the following way:

The C_4 shift was calculated by calculating $A_{\pm \text{ cal}}$ and $A_{z \text{ cal}}$ using Equations (4.18), (4.25) and (4.10) and substituting them in Equation (4.5) to calculate A_{\pm} and A_z . In addition, C_2 was calculated using Equation (2.44) and C_4 was calculated by substituting V_{mag} in Equation (2.45). A_{\pm} , A_z , C_2 and C_4 were then substituted in Equations (2.49) and (2.50).

The C_6 shift was calculated by calculating the average C_6 from Equations (4.11) and (4.19) and substituting it and previously-calculated parameters in Equations (2.51) and (2.52).

The relativistic shift was calculated by substituting previously-calculated parameters in Equations (2.53) and (2.54).

The image charge shift was calculated by calculating B using the $^{12}\text{C}^{4+}$ measurements and substituting it and E'_z and E'_ρ from Chapter 2.6.1.3 in Equations (2.55) and (2.56).

The B_2 shift was calculated by substituting previously-calculated parameters in Equation (4.17) to calculate B_2 and substituting it in Equations (2.62) and (2.63).

The C_1B_1 shift was calculated by substituting C_1 from Section 2.6.3 into Equation (2.64) to calculate Δf_z and substituting it and B_1 from Section 2.6.3 into Equation (2.65).

The lock phase, modulation and DC offset shifts were calculated by substituting previously-calculated parameters into Equations (2.66), (2.67) and (2.68), respectively.

The B drift shift was calculated by subtracting the results of two different $^{12}\text{C}^{4+}$ modified cyclotron sweep measurements measured a few days apart from one another and extrapolating for the date where the neon ion modified cyclotron sweeps were performed.

The coil shift was assumed to be 0 (40) based on estimates done by previous members of the group [61].

The systematic shifts are given in Table 4.3.

4.10 DATA ANALYSIS

The data analysis was performed using several programs and programming languages. Initially the sweep and calibration data was displayed and pre-analysed on the THE-Website, see Section 3.3.2. The calibration data was analysed in Matlab using a script written by [50] (see Section 4.5) and the sweep data was analysed in Python using a script written by [47], see Section 4.8. The calibration and sweep data was then given as input to a Matlab script which uses them to calculate the systematic shifts, magnetic field decay rate and the final results for the neon masses. An independent analysis was performed by [68] in order to verify the results.

4.11 RESULTS

The results for the systematic shifts are given in Table 4.3 and for the neon masses and frequency ratios in Table 4.4.

Both the $^{20}\text{Ne}^{8+}$ and $^{22}\text{Ne}^{7+}$ measurements are limited by long measurement times of about six days between the modified cyclotron sweeps of each pair, contributing to a dominating B temporal drift shift. The measurement times are significantly longer than those of the previous measurements of $^{16}\text{O}^{5+}$ performed by THE-Trap [50] which took a few hours per ion. While the previous measurement used FEP voltages of around -230 V , the neon measurements used FEP voltages of up to -390 V , which produce electron currents strong enough to create a substantial amount of patch potentials (see Section 4.1) on the trap electrodes. These change the trap conditions and thus the calibration parameters after every loading, requiring all calibration measurements to be manually repeated each time.

The neon mass measurement results were re-analysed independently [68]. The results of the two independent analyses were found to be in agreement within a single standard deviation.

Table 4.4: Neon masses measurement results

Isotope	$^{20}\text{Ne}^{8+}$	$^{22}\text{Ne}^{7+}$
$m_{\text{THE-Trap}}$ in amu	19.992 440 170 6(12) _{st} (116) _{sy}	21.991 385 221(4.2) _{st} (16) _{sy}
$m_{\text{literature}}$ in amu	19.992 440 176 2(17)[5, 69]	21.991 385 109(18)[5, 70]
$\delta m_{\text{THE-Trap}}/m_{\text{THE-Trap}}$	$5.8 \cdot 10^{-10}$	$7.7 \cdot 10^{-10}$
$\delta m_{\text{literature}}/m_{\text{literature}}$	$8.4 \cdot 10^{-11}$ [5, 69]	$8.2 \cdot 10^{-10}$ [5, 70]
$\frac{m_{\text{THE-Trap}} - m_{\text{literature}}}{m_{\text{literature}}}$ in ppt	-281 (589)	-5100(1100)
$f_{\text{cycNe}}/f_{\text{cyc}^{12}\text{C}^{4+}}$	0.832 987 831 993(42) _{st} (403) _{sy}	1.047 217 476 89(20) _{st} (82) _{sy}

Neon masses measurement results. The measured and literature [5] ^{20}Ne and ^{22}Ne atomic mass, relative atomic mass uncertainties, cyclotron frequency ratio and the relative distance between the measurements are displayed. “st” and “sy” stand for statistical and systematic uncertainty, respectively. The results are discussed in Section 4.11.

4.11.1 The $^{20}\text{Ne}^{8+}$ Measurement

The $^{20}\text{Ne}^{8+}$ result is comprised of three measurement runs. The first measurement was performed using the “mix2dc” box and the other two are performed using the Lock-In Amplifier. As mentioned in Section 4.11, the uncertainty is dominated by the B temporal drift caused by the long measurement times and as a result the relative uncertainty is about six times as high as that of the literature value [5]. The measured value is one standard deviation smaller than the literature value and is thus in good agreement with it.

4.11.2 The $^{22}\text{Ne}^{7+}$ Measurement

The $^{22}\text{Ne}^{7+}$ result is comprised of a single measurement run. Unlike the $^{22}\text{Ne}^{8+}$ result, the $^{22}\text{Ne}^{7+}$ result is in strong disagreement with the literature value, being about five standard deviations smaller [5, 70], although both the $^{22}\text{Ne}^{8+}$ and the $^{22}\text{Ne}^{7+}$ measurements were performed with the same apparatus and analysed with the same code. To investigate this, a measurement that used ^{22}Ne reference ions to measure the masses of ^{46}Ti and ^{46}V was used [71]. The resulting mass values for ^{46}Ti and ^{46}V each contribute 14% of their respective literature values and are at discrepancies of -1.4 and -2.1 standard deviations in comparison with their literature values, respectively. Re-analysis of the measurements using the THE-Trap value for the ^{22}Ne mass instead of the literature value for the ^{22}Ne mass increases the discrepancies of the resulting mass values for ^{46}Ti and ^{46}V from -1.4 and -2.1 to -1.8 and -2.4 standard deviations in comparison to their respective literature values, respectively. Seeing how both the literature and the THE-Trap values for the ^{22}Ne mass cause a discrepancy in the ^{46}Ti and ^{46}V masses, it is difficult to decide which ^{22}Ne mass value is correct without additional data [26].

CONCLUDING REMARKS

In the scope of this thesis a gas inlet system was constructed and used to inject neon into a Penning-trap and measure the mass of two neon isotopes $^{20,22}\text{Ne}$ using a $^{12}\text{C}^{4+}$ reference ion. The mass of $^{20}\text{Ne}^{8+}$ was measured with a relative uncertainty of $5.8 \cdot 10^{-10}$ and is within one standard deviation in agreement with the literature value, which has a relative uncertainty of $8.4 \cdot 10^{-11}$. The mass of $^{22}\text{Ne}^{7+}$ was measured with a relative uncertainty of $7.7 \cdot 10^{-10}$. The measured value is at a discrepancy of five standard deviations in comparison to the literature value, which has a relative uncertainty of $8.2 \cdot 10^{-10}$. The discrepancy is difficult to explain as the ^{20}Ne mass measurement was performed using the same setup and was analyzed with the same methods and is in agreement with the literature value. In addition, mass measurements of ^{46}Ti and ^{46}V performed using a ^{22}Ne reference ion are in disagreement with their respective literature values when using both the measured and the literature ^{22}Ne mass values.

The applied FEP voltage of -390 V caused noticeable patch potentials on the trap electrodes, changing the calibration parameters between measurements and thus forcing the calibration measurements to be continuously repeated. This prolonged the measurement times and increased the systematic uncertainty of the magnetic field drift to the extent where it became the leading cause of systematic uncertainty for both measurements. The measurement time can be reduced by introducing a high precision voltage source capable of reaching voltages of -152 V and -167 V and thus trapping $^{20}\text{Ne}^{4+}$ and $^{22}\text{Ne}^{4+}$, respectively. These ion species require a lower (in absolute value) FEP voltage of about -220 V to ionize and thus should not create any noticeable patch potentials, judging from past measurements in the group where a FEP voltage of -230 V was used. Alternatively, the ion loading frequency can be reduced by using a second Penning trap, such that the neon ion is measured at one trap while the $^{12}\text{C}^{4+}$ ion is stored at the other. The ions are then switched and the $^{12}\text{C}^{4+}$ ion is measured.

In addition to the neon mass measurements, the magnet was repaired, charged, shimmed and had its shielding factor measured to be 173 (2). Also, a new Python program and a new PHP website were created for the data acquisition system and a new lock system was developed using a Lock-In Amplifier.

A new experiment is constructed in the group using the same magnet which aims at the first direct high-precision (10^{-9}) measurement of the nuclear magnetic moment of helium-3. Specifically, as the measurement techniques which will be used are based on the detection of single spin-flips, a novel Penning-trap design is developed which is optimized for nuclear spin-flip detection.

APPENDIX

A.1 THE-TRAP PARAMETERS

Table A.1: THE-Trap Parameters

Symbol	Value	Reference	Section
κ	≈ 0.8	[47]	2.3.1
C_{total}	≈ 20 pF	[50]	2.3.1
Q	≈ 800		2.3.4
τ	≈ 20 ms		2.3.4
ε	$4 \cdot 10^{-4}$		2.5.1
$\varepsilon\omega_z/4\omega_{\text{mod}}$	$8 \cdot 10^{-3}$		2.5.1
$C_{\text{CE},1,1}/V_{\text{CE}}$	1.3m^{-1}	[50]	2.4
T_z	10K	[48]	2.3.2
$V_{\text{mod mix2dc}}$	0.016 V		2.5.1
$V_{\text{mod LIA}}$	0.017 V		2.5.1
ω_{mod}	$2\pi \cdot 10^5$ Hz		2.5.1
$C_{\text{CE},4,0}$	$-5.34(36) \cdot 10^8\text{m}^{-4}$	[47]	2.4
$V_{\text{LHe in Magnet}}$	200 L	[50]	3.1
$I_{\text{magnet inner coil}}$	32.44 A		3.1
$I_{\text{magnet outer coil}}$	37.71 A		3.1
d	2.11 mm	[47]	2.2
ρ_0	2.77 mm	[47]	2.2
z_0	2.29 mm	[47]	2.2
d	2.11 mm	[47]	2.2
$\rho_{\text{endcap hole}}$	300 μm	[47]	Section 2.2
$V_{\text{lock cal}}$	$\begin{cases} 99920 & \text{mix2dc} \\ 10717 & \text{LIA} \end{cases}$		3.4.1

A.2 EXPANSION OF THE ELECTROSTATIC POTENTIAL

the first few $r^l Y_{l,m}$ terms in Cartesian coordinates are:

$$l = 0 : Y_{0,0} = \frac{1}{\sqrt{4\pi}}, \quad (\text{A.1})$$

$$l = 1 : rY_{1,-1} = \sqrt{\frac{3}{8\pi}}(x - iy), rY_{1,0} = \sqrt{\frac{3}{8\pi}}z, rY_{1,1} = -\sqrt{\frac{3}{8\pi}}(x + iy), \quad (\text{A.2})$$

$$l = 2 : r^2Y_{2,-2} = \sqrt{\frac{15}{32\pi}}(x - iy)^2, r^2Y_{2,-1} = \sqrt{\frac{15}{8\pi}}(x - iy)z, \quad (\text{A.3})$$

$$r^2Y_{2,0} = \sqrt{\frac{5}{16\pi}}(2z^2 - x^2 - y^2), r^2Y_{2,1} = -\sqrt{\frac{15}{8\pi}}(x + iy)z, r^2Y_{2,2} = \sqrt{\frac{15}{32\pi}}(x + iy)^2. \quad (\text{A.4})$$

The terms are complex. By using specific linear combinations they can be made real. For instance, by setting all coefficients of $r^l Y_{l,m}$ to 1 and taking the imaginary part of $r^l Y_{l,m}$ in case m is positive and the real part otherwise, the first few terms become:

$$l = 0 : Y_{0,0} = 1, \quad (\text{A.5})$$

$$l = 1 : rY_{1,-1} = x, rY_{1,0} = z, rY_{1,1} = y, \quad (\text{A.6})$$

$$l = 2 : r^2Y_{2,-2} = x^2 - y^2, r^2Y_{2,-1} = xz, \quad (\text{A.7})$$

$$r^2Y_{2,0} = z^2 - \frac{1}{2}x^2 - \frac{1}{2}y^2, r^2Y_{2,1} = yz, r^2Y_{2,2} = xy, \quad (\text{A.8})$$

where the coefficient for $r^2Y_{2,0}$ was halved in order to maintain consistency with other publications [50].

A.3 DRIVING AND COUPLING THE MODES

In Section 2.5 it was mentioned that:

1. the amplitude of a forced harmonic oscillator is proportional to the duration t the force was applied during.
2. applying a non-homogenous signal at the sum or the difference between two frequencies ω_z and ω_{\pm} will cause for one of the cases action transfer between the modes and for the other exponential increase of the amplitudes of both.

Next a non-rigorous proof will be given of both claims.

1. Substituting $x = Bt \sin(\omega_0 t)$ in the equation of motion for a forced harmonic oscillator:

$$-\omega_0^2 x + A \cos(\omega_0 t) = \ddot{x}, \quad (\text{A.9})$$

it is obtained that $x = \frac{A}{2\omega_0} t \sin(\omega_0 t)$. Thus it is shown that the amplitude of a forced harmonic oscillator is proportional to t . It also lags 90° behind the drive force, which will be relevant for the second point.

2. As an example, the force coupling between ω_z and ω_+ will be discussed:

$$\vec{F} \propto (z\hat{x} + x\hat{z}) \cos(\omega_{\text{drive}} t). \quad (\text{A.10})$$

It is assumed for simplicity that the reduced cyclotron motion is one-dimensional, specifically that it is only acting on the x direction.

Assume that the initial conditions for the ion motion are $x(t=0) = 0$, $z(t=0) \neq 0$, such that $z(t) \propto \cos(\omega_z t + \varphi_z)$. First the case of $\omega_{\text{drive}} = \omega_z - \omega_+$ will be analysed. Using $\cos(a) \cos(b) = \frac{1}{2} \cos(a+b) + \frac{1}{2} \cos(a-b)$, it is obtained that

$$\vec{F} \propto (z\hat{x} + x\hat{z}) \cos(\omega_+ t + \varphi_z) t, \quad (\text{A.11})$$

where the effect of the first term is assumed to be negligible because its non-resonant. As previously shown, the forced harmonic oscillator motion inspired by this driving force has a phase of $\varphi_z - \frac{\pi}{2}$. This motion inspires a force in the z direction:

$$F_z \propto \cos\left(\omega_z t + \varphi_z - \frac{\pi}{2}\right), \quad (\text{A.12})$$

which inspires a motion in the z direction with a π phase difference to the original motion. As a result, the z amplitude will decrease. In conclusion, the force will cause the x amplitude to increase and the z amplitude to decrease. Eventually the z amplitude will reach 0, such that $F_x = 0$. However, seeing how the x amplitude is positive, it still holds that $F_z \neq 0$, and so

the z amplitude will continue to decrease to negative values. The force in the x direction will decrease because it is proportional to the z amplitude which changed its sign. This continues until $x = 0$, at which point the x amplitude becomes negative, the force in the z direction switches sign, the z amplitude starts increasing and so on in an oscillatory manner. Thus $\omega_{\text{drive}} = \omega_+ - \omega_z$ causes Rabi oscillations.

For the case of $\omega_{\text{drive}} = \omega_z + \omega_+$, a similar argument shows that the force in the x direction is $F_x \propto \cos(\omega_+ t - \phi_z)$, such that the x motion is given by $x \propto \cos(\omega_+ t - \phi_z - \frac{\pi}{2})$. The force in the z direction is $F_z \propto \cos(\omega_z t + \phi_z + \frac{\pi}{2})$ such that the z motion is given by $z \propto \cos(\omega_z t + \phi_z)$. It is seen that for $\omega_{\text{drive}} = \omega_z + \omega_+$, the z amplitude increases, not decreases. Seeing how both the z and the x amplitudes increase, instead of oscillations an exponential increase of both amplitudes is obtained.

For $\omega_{\text{drive}} = \omega_z \pm \omega_-$, the motion is caused by the $\vec{E} \times \vec{B}$ drift force and not by $\vec{F} = -k\vec{x}$. It can be shown that the motion inspired by such a force is 90° ahead of it in phase, not 90° behind. As a result the roles are reversed: Rabi oscillations are caused by $\omega_{\text{drive}} = \omega_z + \omega_-$ and exponential increase is caused by $\omega_{\text{drive}} = \omega_z - \omega_-$.

A.4 SYSTEMATIC SHIFTS - FORMULAS NOT USED IN THE THESIS

A.4.1 The $C_{\text{total } 4}$ and $C_{\text{total } 6}$ Shifts

$$\frac{\Delta\omega_{\pm}}{\omega_{\pm}} = \pm \frac{3C_{4 \text{ total}}}{2C_{2 \text{ total}}} \frac{\omega_{\mp}}{\omega_+ - \omega_-} (A_{\pm}^2 - 2A_z^2 + 2A_{\mp}^2), \quad (\text{A.13})$$

$$\frac{\Delta\omega_{\pm}}{\omega_{\pm}} = \mp \frac{45C_{6 \text{ total}}}{24C_{2 \text{ total}}} \frac{\omega_{\mp}}{\omega_+ - \omega_-} (A_{\pm}^4 - 6A_{\pm}^2 A_z^2 + 3A_z^4 + 6A_+^2 A_-^2 - 12A_{\mp}^2 A_z^2 + 3A_{\mp}^4). \quad (\text{A.14})$$

A.4.2 Image Charge Shift

$$\frac{\Delta\omega_{\pm}}{\omega_{\pm}} \approx \mp \frac{nE'_{\rho}}{B} \frac{\omega_+ + \omega_-}{\omega_+ - \omega_-} \approx \mp \frac{nE'_{\rho}}{B}, \quad (\text{A.15})$$

$$\frac{\Delta\omega_c}{\omega_c} \approx -n \frac{2E'_{\rho} + E'_z}{2B}. \quad (\text{A.16})$$

A.4.3 Trap Tilt

$$\frac{\Delta\omega_+}{\omega_+} \approx \frac{9}{2} \frac{\omega_-^2}{(\omega_+ - \omega_-)(\omega_+ - 2\omega_-)} \theta^2 + \frac{3}{2} \frac{\omega_-}{\omega_+ - \omega_-} \theta^2 \approx \frac{3}{2} \frac{\omega_-}{\omega_+} \theta^2, \quad (\text{A.17})$$

$$\frac{\Delta\omega_-}{\omega_-} \approx \frac{9}{2} \frac{\omega_+^2}{(\omega_+ - \omega_-)(\omega_+ - 2\omega_-)} \theta^2 - \frac{3}{2} \frac{\omega_+}{\omega_+ - \omega_-} \theta^2 \approx \frac{3}{4} \theta^2. \quad (\text{A.18})$$

A.4.4 *Magnetic Field Shift - B_2*

$$\frac{\Delta\omega_{\pm}}{\omega_{\pm}} = \pm \frac{B_2}{2B_0} \frac{\omega_c}{\omega_{\pm}(\omega_+ - \omega_-)} (\omega_{\pm} A_z^2 - \omega_{\pm} A_{\pm}^2 - (\omega_+ + \omega_-) A_{\mp}^2). \quad (\text{A.19})$$

BIBLIOGRAPHY

- [1] Edmund G. Myers. “The most precise atomic mass measurements in Penning traps.” In: *International Journal of Mass Spectrometry* 349-350 (2013). 100 years of Mass Spectrometry, pp. 107–122. DOI: <https://doi.org/10.1016/j.ijms.2013.03.018>. URL: <http://www.sciencedirect.com/science/article/pii/S1387380613001097> (cit. on p. 1).
- [2] K.S. Sharma. “Mass spectrometry—The early years.” In: *International Journal of Mass Spectrometry* 349-350 (2013). 100 years of Mass Spectrometry, pp. 3–8. DOI: <https://doi.org/10.1016/j.ijms.2013.05.028>. URL: <http://www.sciencedirect.com/science/article/pii/S1387380613002145> (cit. on p. 1).
- [3] Simon Rainville, James K. Thompson, and David E. Pritchard. “An Ion Balance for Ultra-High-Precision Atomic Mass Measurements.” In: *Science* 303.5656 (2004), pp. 334–338. DOI: [10.1126/science.1092320](https://doi.org/10.1126/science.1092320). eprint: <http://science.sciencemag.org/content/303/5656/334.full.pdf>. URL: <http://science.sciencemag.org/content/303/5656/334> (cit. on p. 1).
- [4] A Mooser, A Rischka, A Schneider, K Blaum, S Ulmer, and J Walz. “A New Experiment for the Measurement of the g-Factors of $^3\text{He}^+$ and $^3\text{He}^{2+}$.” In: *Journal of Physics: Conference Series* 1138 (Nov. 2018), p. 012004. DOI: [10.1088/1742-6596/1138/1/012004](https://doi.org/10.1088/1742-6596/1138/1/012004) (cit. on p. 1).
- [5] Meng Wang, G. Audi, F.G. Kondev, W.J. Huang, S. Naimi, and Xing Xu. “The AME2016 atomic mass evaluation (II). Tables, graphs and references.” In: *Chinese Physics C* 41.3 (2017), p. 030003. URL: <http://stacks.iop.org/1674-1137/41/i=3/a=030003> (cit. on pp. 1, 3, 62).
- [6] Jens Dilling, Klaus Blaum, Maxime Brodeur, and Sergey Eliseev. “Penning-Trap Mass Measurements in Atomic and Nuclear Physics.” In: *Annual Review of Nuclear and Particle Science* 68.1 (2018), pp. 45–74. DOI: [10.1146/annurev-nucl-102711-094939](https://doi.org/10.1146/annurev-nucl-102711-094939). eprint: <https://doi.org/10.1146/annurev-nucl-102711-094939>. URL: <https://doi.org/10.1146/annurev-nucl-102711-094939> (cit. on p. 1).
- [7] E.W. Otten, J. Bonn, and Ch. Weinheimer. “The Q-value of tritium beta-decay and the neutrino mass.” In: *International Journal of Mass Spectrometry* 251.2 (2006). ULTRA-ACCURATE MASS SPECTROMETRY AND RELATED TOPICS Dedicated to H.-J. Kluge on the occasion of his 65th birthday anniversary, pp. 173–178. DOI: <https://doi.org/10.1016/j.ijms.2006.01.035>. URL: <http://www.sciencedirect.com/science/article/pii/S1387380606000741> (cit. on pp. 1, 2).
- [8] V. N. Aseev et al. “Upper limit on the electron antineutrino mass from the Troitsk experiment.” In: *Phys. Rev. D* 84 (11 Dec. 2011), p. 112003. DOI: [10.1103/PhysRevD.84.112003](https://doi.org/10.1103/PhysRevD.84.112003). URL: <https://link.aps.org/doi/10.1103/PhysRevD.84.112003> (cit. on pp. 1, 2).

- [9] Chen Ning Yang. “Fermi’s beta-decay Theory.” In: *Asia Pacific Physics Newsletter* 01.01 (2012), pp. 27–30. DOI: [10.1142/S2251158X12000045](https://doi.org/10.1142/S2251158X12000045). eprint: <https://doi.org/10.1142/S2251158X12000045>. URL: <https://doi.org/10.1142/S2251158X12000045> (cit. on p. 1).
- [10] F. Reines and C. Cowan. “The Reines-Cowan experiments: Detecting the Poltergeist.” In: *Los Alamos Sci.* 25 (1997), pp. 4–27 (cit. on p. 1).
- [11] G. Danby, J-M. Gaillard, K. Goulianos, L. M. Lederman, N. Mistry, M. Schwartz, and J. Steinberger. “Observation of High-Energy Neutrino Reactions and the Existence of Two Kinds of Neutrinos.” In: *Phys. Rev. Lett.* 9 (1 July 1962), pp. 36–44. DOI: [10.1103/PhysRevLett.9.36](https://doi.org/10.1103/PhysRevLett.9.36). URL: <https://link.aps.org/doi/10.1103/PhysRevLett.9.36> (cit. on p. 1).
- [12] B. Lundberg, K. Niwa, and V. Paolone. “OBSERVATION OF THE TAU NEUTRINO.” In: *Annual Review of Nuclear and Particle Science* 53.1 (2003), pp. 199–218. DOI: [10.1146/annurev.nucl.53.041002.110555](https://doi.org/10.1146/annurev.nucl.53.041002.110555). eprint: <https://doi.org/10.1146/annurev.nucl.53.041002.110555>. URL: <https://doi.org/10.1146/annurev.nucl.53.041002.110555> (cit. on p. 1).
- [13] Y. Fukuda et al. “Evidence for Oscillation of Atmospheric Neutrinos.” In: *Phys. Rev. Lett.* 81 (8 Aug. 1998), pp. 1562–1567. DOI: [10.1103/PhysRevLett.81.1562](https://doi.org/10.1103/PhysRevLett.81.1562). URL: <https://link.aps.org/doi/10.1103/PhysRevLett.81.1562> (cit. on p. 1).
- [14] Q. R. Ahmad et al. “Direct Evidence for Neutrino Flavor Transformation from Neutral-Current Interactions in the Sudbury Neutrino Observatory.” In: *Phys. Rev. Lett.* 89 (1 June 2002), p. 011301. DOI: [10.1103/PhysRevLett.89.011301](https://doi.org/10.1103/PhysRevLett.89.011301). URL: <https://link.aps.org/doi/10.1103/PhysRevLett.89.011301> (cit. on p. 1).
- [15] Takaaki Kajita. “Nobel Lecture: Discovery of atmospheric neutrino oscillations.” In: *Rev. Mod. Phys.* 88 (3 July 2016), p. 030501. DOI: [10.1103/RevModPhys.88.030501](https://doi.org/10.1103/RevModPhys.88.030501). URL: <https://link.aps.org/doi/10.1103/RevModPhys.88.030501> (cit. on p. 1).
- [16] K.A. Olive. “Review of Particle Physics.” In: *Chinese Physics C* 38.9 (Aug. 2014), p. 090001. DOI: [10.1088/1674-1137/38/9/090001](https://doi.org/10.1088/1674-1137/38/9/090001). URL: <https://doi.org/10.1088/1674-1137/38/9/090001> (cit. on p. 1).
- [17] Uros Seljak, Anze Slosar, and Patrick McDonald. “Cosmological parameters from combining the Lyman-alpha forest with CMB, galaxy clustering and SN constraints.” In: *JCAP* 0610 (2006), p. 014. DOI: [10.1088/1475-7516/2006/10/014](https://doi.org/10.1088/1475-7516/2006/10/014). arXiv: [astro-ph/0604335](https://arxiv.org/abs/astro-ph/0604335) [astro-ph] (cit. on p. 1).
- [18] Marco Cirelli and Alessandro Strumia. “Cosmology of neutrinos and extra light particles after WMAP3.” In: *JCAP* 0612 (2006), p. 013. DOI: [10.1088/1475-7516/2006/12/013](https://doi.org/10.1088/1475-7516/2006/12/013). arXiv: [astro-ph/0607086](https://arxiv.org/abs/astro-ph/0607086) [astro-ph] (cit. on p. 1).
- [19] Elena Giusarma, Roland de Putter, Shirley Ho, and Olga Mena. “Constraints on neutrino masses from Planck and Galaxy clustering data.” In: *Phys. Rev. D* 88 (6 Sept. 2013), p. 063515. DOI: [10.1103/PhysRevD.88.063515](https://doi.org/10.1103/PhysRevD.88.063515). URL: <https://link.aps.org/doi/10.1103/PhysRevD.88.063515> (cit. on p. 2).

- [20] Ch Kraus et al. "Final results from phase II of the Mainz neutrino mass search in tritium beta decay." In: *The European Physical Journal C - Particles and Fields* 40.4 (Apr. 2005), pp. 447–468. DOI: [10.1140/epjc/s2005-02139-7](https://doi.org/10.1140/epjc/s2005-02139-7). URL: <https://doi.org/10.1140/epjc/s2005-02139-7> (cit. on p. 2).
- [21] Guido Drexlin. "KATRIN - direct measurement of a sub-eV neutrino mass." In: *Nuclear Physics B - Proceedings Supplements* 145 (2005). NOW 2004, pp. 263–267. DOI: <https://doi.org/10.1016/j.nuclphysbps.2005.04.019>. URL: <http://www.sciencedirect.com/science/article/pii/S0920563205005165> (cit. on p. 2).
- [22] L. I. Bodine, D. S. Parno, and R. G. H. Robertson. "Assessment of molecular effects on neutrino mass measurements from tritium beta decay." In: *Phys. Rev. C* 91 (3 Mar. 2015), p. 035505. DOI: [10.1103/PhysRevC.91.035505](https://doi.org/10.1103/PhysRevC.91.035505). URL: <https://link.aps.org/doi/10.1103/PhysRevC.91.035505> (cit. on p. 2).
- [23] S Bauer, R Berendes, F Hochschulz, H -W Ortjohann, S Rosendahl, T Thümmeler, M Schmidt, and C Weinheimer. "Next generation KATRIN high precision voltage divider for voltages up to 65kV." In: *Journal of Instrumentation* 8.10 (Oct. 2013), P10026–P10026. DOI: [10.1088/1748-0221/8/10/p10026](https://doi.org/10.1088/1748-0221/8/10/p10026). URL: <https://doi.org/10.1088/1748-0221/8/10/p10026> (cit. on p. 2).
- [24] Sz Nagy, T Fritioff, M Björkhage, I Bergström, and R Schuch. "On the Q-value of the tritium beta-decay." In: *Europhysics Letters* 74.3 (May 2006), pp. 404–410. DOI: [10.1209/epl/i2005-10559-2](https://doi.org/10.1209/epl/i2005-10559-2). URL: <https://doi.org/10.1209/epl/i2005-10559-2> (cit. on p. 2).
- [25] E. G. Myers, A. Wagner, H. Kracke, and B. A. Wesson. "Atomic Masses of Tritium and Helium-3." In: *Phys. Rev. Lett.* 114 (1 Jan. 2015), p. 013003. DOI: [10.1103/PhysRevLett.114.013003](https://doi.org/10.1103/PhysRevLett.114.013003). URL: <https://link.aps.org/doi/10.1103/PhysRevLett.114.013003> (cit. on pp. 2–4).
- [26] Wenjia Huang. "private communication with Wenjia Huang." In: (2019) (cit. on pp. 3, 62).
- [27] R. S. Van Dyck, F. L. Moore, D. L. Farnham, and P. B. Schwinberg. "Number dependency in the compensated Penning trap." In: *Phys. Rev. A* 40 (11 Dec. 1989), pp. 6308–6313. DOI: [10.1103/PhysRevA.40.6308](https://doi.org/10.1103/PhysRevA.40.6308). URL: <https://link.aps.org/doi/10.1103/PhysRevA.40.6308> (cit. on p. 3).
- [28] Eric A. Cornell, Robert M. Weisskoff, Kevin R. Boyce, Robert W. Flanagan, Gregory P. Lafyatis, and David E. Pritchard. "Single-ion cyclotron resonance measurement of $M(\text{CO}^+)/M(\text{N}_2^+)$." In: *Phys. Rev. Lett.* 63 (16 Oct. 1989), pp. 1674–1677. DOI: [10.1103/PhysRevLett.63.1674](https://doi.org/10.1103/PhysRevLett.63.1674). URL: <https://link.aps.org/doi/10.1103/PhysRevLett.63.1674> (cit. on p. 3).
- [29] Jochen Erler, Noah Birge, Markus Kortelainen, Witold Nazarewicz, Erik Olsen, Alexander M. Perhac, and Mario Stoitsov. "The limits of the nuclear landscape." In: *Nature* 486 (June 2012), 509 EP -. URL: <https://doi.org/10.1038/nature11188> (cit. on p. 4).

- [30] Georges Audi. "The history of nuclidic masses and of their evaluation." In: *International Journal of Mass Spectrometry* 251.2 (2006). ULTRA-ACCURATE MASS SPECTROMETRY AND RELATED TOPICS Dedicated to H.-J. Kluge on the occasion of his 65th birthday anniversary, pp. 85–94. DOI: <https://doi.org/10.1016/j.ijms.2006.01.048>. URL: <http://www.sciencedirect.com/science/article/pii/S1387380606000820> (cit. on p. 4).
- [31] S L Zafonte and R S Van Dyck. "Ultra-precise single-ion atomic mass measurements on deuterium and helium-3." In: *Metrologia* 52.2 (Mar. 2015), pp. 280–290. DOI: [10.1088/0026-1394/52/2/280](https://doi.org/10.1088/0026-1394/52/2/280). URL: <https://doi.org/10.1088/0026-1394/52/2/280> (cit. on p. 4).
- [32] F. Heiße et al. "High-Precision Measurement of the Proton's Atomic Mass." In: *Phys. Rev. Lett.* 119 (3 July 2017), p. 033001. DOI: [10.1103/PhysRevLett.119.033001](https://doi.org/10.1103/PhysRevLett.119.033001). URL: <https://link.aps.org/doi/10.1103/PhysRevLett.119.033001> (cit. on p. 4).
- [33] Zong-Chao Yan, Jun-Yi Zhang, and Yue Li. "Energies and polarizabilities of the hydrogen molecular ions." In: *Phys. Rev. A* 67 (6 June 2003), p. 062504. DOI: [10.1103/PhysRevA.67.062504](https://doi.org/10.1103/PhysRevA.67.062504). URL: <https://link.aps.org/doi/10.1103/PhysRevA.67.062504> (cit. on p. 4).
- [34] S. Hamzeloui, J. A. Smith, D. J. Fink, and E. G. Myers. "Precision mass ratio of $^3\text{He}^+$ to HD^+ ." In: *Phys. Rev. A* 96 (6 Dec. 2017), p. 060501. DOI: [10.1103/PhysRevA.96.060501](https://doi.org/10.1103/PhysRevA.96.060501). URL: <https://link.aps.org/doi/10.1103/PhysRevA.96.060501> (cit. on p. 4).
- [35] F. Heiße et al. "The LIONTRAP experiment - A new high-precision mass spectrometer for light ions." In: (2019) (cit. on p. 4).
- [36] Lowell S. Brown and Gerald Gabrielse. "Geonium theory: Physics of a single electron or ion in a Penning trap." In: *Rev. Mod. Phys.* 58 (1 Jan. 1986), pp. 233–311. DOI: [10.1103/RevModPhys.58.233](https://doi.org/10.1103/RevModPhys.58.233). URL: <https://link.aps.org/doi/10.1103/RevModPhys.58.233> (cit. on pp. 7, 9, 18, 21, 23, 25, 27, 49).
- [37] Eric A. Cornell, Robert M. Weisskoff, Kevin R. Boyce, and David E. Pritchard. "Mode coupling in a Penning trap: pi pulses and a classical avoided crossing." In: *Phys. Rev. A* 41 (1 Jan. 1990), pp. 312–315. DOI: [10.1103/PhysRevA.41.312](https://doi.org/10.1103/PhysRevA.41.312). URL: <https://link.aps.org/doi/10.1103/PhysRevA.41.312> (cit. on p. 7).
- [38] Robert Mark Weisskoff. "Detecting single, trapped ions." In: *Massachusetts Institute of Technology* (1988). URL: <http://hdl.handle.net/1721.1/68230> (cit. on pp. 7, 14, 18, 21, 25).
- [39] Jochen Ketter. "Verbesserungen der Ionennachweissysteme des Präzisions-Penningfallen-Massenspektrometers TRIGA-TRAP." In: *Diplomarbeit, Johannes Gutenberg-Universität Mainz* (2009). URL: <http://hdl.handle.net/11858/00-001M-0000-0011-767C-C> (cit. on p. 10).
- [40] Joseph Tan and Gerald Gabrielse. "One electron in an orthogonalized cylindrical Penning trap." English (US). In: *Applied Physics Letters* 55.20 (Dec. 1989), pp. 2144–2146. DOI: [10.1063/1.102084](https://doi.org/10.1063/1.102084) (cit. on p. 9).

- [41] G. Gräff, H. Kalinowsky, and J. Traut. "A direct determination of the proton electron mass ratio." In: *Zeitschrift für Physik A Atoms and Nuclei* 297.1 (Mar. 1980), pp. 35–39. DOI: [10.1007/BF01414243](https://doi.org/10.1007/BF01414243). URL: <https://doi.org/10.1007/BF01414243> (cit. on p. 11).
- [42] G. Gärtner and E. Klempt. "A direct determination of the proton-electron mass ratio." In: *Zeitschrift für Physik A Atoms and Nuclei* 287.1 (Mar. 1978), pp. 1–6. DOI: [10.1007/BF01408352](https://doi.org/10.1007/BF01408352). URL: <https://doi.org/10.1007/BF01408352> (cit. on p. 11).
- [43] S. Eliseev, K. Blaum, M. Block, C. Droese, M. Goncharov, E. Minaya Ramirez, D. A. Nesterenko, Yu. N. Novikov, and L. Schweikhard. "Phase-Imaging Ion-Cyclotron-Resonance Measurements for Short-Lived Nuclides." In: *Phys. Rev. Lett.* 110 (8 Feb. 2013), p. 082501. DOI: [10.1103/PhysRevLett.110.082501](https://doi.org/10.1103/PhysRevLett.110.082501). URL: <https://link.aps.org/doi/10.1103/PhysRevLett.110.082501> (cit. on p. 11).
- [44] H. G. Dehmelt and F. L. Walls. "'Bolometric" Technique for the rf Spectroscopy of Stored Ions." In: *Phys. Rev. Lett.* 21 (3 July 1968), pp. 127–131. DOI: [10.1103/PhysRevLett.21.127](https://doi.org/10.1103/PhysRevLett.21.127). URL: <https://link.aps.org/doi/10.1103/PhysRevLett.21.127> (cit. on p. 11).
- [45] W. Shockley. "Currents to Conductors Induced by a Moving Point Charge." In: *Journal of Applied Physics* 9.10 (1938), pp. 635–636. DOI: [10.1063/1.1710367](https://doi.org/10.1063/1.1710367). eprint: <https://doi.org/10.1063/1.1710367>. URL: <https://doi.org/10.1063/1.1710367> (cit. on p. 12).
- [46] Gerald Gabrielse. "Detection, damping, and translating the center of the axial oscillation of a charged particle in a Penning trap with hyperbolic electrodes." In: *Phys. Rev. A* 29 (2 Feb. 1984), pp. 462–469. DOI: [10.1103/PhysRevA.29.462](https://doi.org/10.1103/PhysRevA.29.462). URL: <https://link.aps.org/doi/10.1103/PhysRevA.29.462> (cit. on pp. 12, 18).
- [47] M. Schuh. "Simulations of the electrostatic and magnetic field properties and tests of the Penning-ion source at THE-Trap." In: *Master Thesis, Karl-Ruprecht-Universität, Heidelberg* (2014). URL: <http://hdl.handle.net/11858/00-001M-0000-0024-46A3-7> (cit. on pp. 12, 19, 20, 24, 29, 34, 58, 61, 65).
- [48] "Progress with the MPIK/UW-PTMS in Heidelberg." In: *Springer Netherlands* (2011), 199(1-3):291–300. URL: <http://dx.doi.org/10.1007/s10751-011-0324-6> (cit. on pp. 14, 29, 38, 65).
- [49] D. J. Wineland and H. G. Dehmelt. "Principles of the stored ion calorimeter." In: *Journal of Applied Physics* 46.2 (1975), pp. 919–930. DOI: [10.1063/1.321602](https://doi.org/10.1063/1.321602). eprint: <https://doi.org/10.1063/1.321602>. URL: <https://doi.org/10.1063/1.321602> (cit. on p. 14).
- [50] M Höcker. "Precision Mass Measurements at THE-Trap and the FSU trap." In: *PhD Thesis, Ruprecht-Karls-Universität, Heidelberg*. (2016). URL: <http://hdl.handle.net/11858/00-001M-0000-002B-13A5-5> (cit. on pp. 16, 18, 19, 21, 24, 26, 29, 31, 57, 59, 61, 65, 66).
- [51] Michael Patrick Bradley. "A sub-ppb measurement of the mass of cesium for a new determination of the fine-structure constant." In: *Massachusetts Institute of Technology*. (2000). URL: <http://hdl.handle.net/1721.1/28222> (cit. on p. 18).

- [52] Martin Kretzschmar. "Single particle motion in a Penning trap: description in the classical canonical formalism." In: *Physica Scripta* 46.6 (Dec. 1992), pp. 544–554. DOI: [10.1088/0031-8949/46/6/011](https://doi.org/10.1088/0031-8949/46/6/011). URL: <https://doi.org/10.1088/0031-8949/46/6/011> (cit. on pp. 18, 19).
- [53] Martin Kretzschmar. "Theoretical investigations of different excitation modes for Penning trap mass spectrometry." In: *International Journal of Mass Spectrometry* 349-350 (2013). 100 years of Mass Spectrometry, pp. 227–239. DOI: <https://doi.org/10.1016/j.ijms.2013.03.023>. URL: <http://www.sciencedirect.com/science/article/pii/S1387380613001383> (cit. on pp. 18, 19).
- [54] E.J. Braendas and E.S. Kryachko. "Fundamental World of Quantum Chemistry." In: *Kluwer Academic Publishers* (2003) (cit. on pp. 18, 19).
- [55] Sven Sturm. "The g-factor of the electron bound in $^{28}\text{Si}^{13+}$: The most stringent test of bound-state quantum electrodynamics." eng. PhD thesis. Mainz: Johannes-Gutenberg Universität, 2012 (cit. on pp. 20, 24).
- [56] Jochen Ketter. "Theoretical treatment of miscellaneous frequency-shifts in Penning traps with classical perturbation theory." In: *PhD Thesis, Ruprecht-Karls-Universität, Heidelberg* (2015). URL: <http://hdl.handle.net/11858/00-001M-0000-0026-BF31-9> (cit. on pp. 22, 23, 25, 27).
- [57] B. W. Shore, M. V. Gromovyy, L. P. Yatsenko, and V. I. Romanenko. "Simple mechanical analogs of rapid adiabatic passage in atomic physics." In: *American Journal of Physics* 77.12 (2009), pp. 1183–1194. DOI: [10.1119/1.3231688](https://doi.org/10.1119/1.3231688). eprint: <https://doi.org/10.1119/1.3231688>. URL: <https://doi.org/10.1119/1.3231688> (cit. on p. 22).
- [58] Jochen Ketter, Tommi Eronen, Martin Höcker, Sebastian Streubel, and Klaus Blaum. "First-order perturbative calculation of the frequency-shifts caused by static cylindrically-symmetric electric and magnetic imperfections of a Penning trap." In: *International Journal of Mass Spectrometry* 358 (2014), pp. 1–16. DOI: <https://doi.org/10.1016/j.ijms.2013.10.005>. URL: <http://www.sciencedirect.com/science/article/pii/S1387380613003722> (cit. on pp. 23, 25, 29).
- [59] G. Gabrielse. "The true cyclotron frequency for particles and ions in a Penning trap." In: *International Journal of Mass Spectrometry* 279.2 (2009), pp. 107–112. DOI: <https://doi.org/10.1016/j.ijms.2008.10.015>. URL: <http://www.sciencedirect.com/science/article/pii/S1387380608004247> (cit. on p. 25).
- [60] Ch. Gerz, D. Wilsdorf, and G. Werth. "A high precision Penning trap mass spectrometer." In: *Nuclear Instruments and Methods in Physics Research Section B: Beam Interactions with Materials and Atoms* 47.4 (1990), pp. 453–461. DOI: [https://doi.org/10.1016/0168-583X\(90\)90626-6](https://doi.org/10.1016/0168-583X(90)90626-6). URL: <http://www.sciencedirect.com/science/article/pii/0168583X90906266> (cit. on p. 25).
- [61] "Private communicaton with Dr. Martin Höcker." In: () (cit. on pp. 26, 28, 61).

- [62] D. B. Pinegar. "Tools for a precise tritium to helium-3 mass comparison. Ph.D. thesis." In: *University of Washington, Seattle* (2007). URL: <http://search.proquest.com/docview/304796368/abstract> (cit. on p. 29).
- [63] Christoph Diehl. "First mass measurements with the MPIK/UW-PTMS." In: *MPI for Nuclear Physics* (2011). URL: <http://www.ub.uni-heidelberg.de/archiv/12038> (cit. on pp. 29, 38).
- [64] S. Streubel, T. Eronen, M. Höcker, J. Ketter, M. Schuh, R. S. Van Dyck, and K. Blaum. "Toward a more accurate Q value measurement of tritium: status of THE-Trap." In: *Applied Physics B* 114.1 (Jan. 2014), pp. 137–145. DOI: 10.1007/s00340-013-5669-x. URL: <https://doi.org/10.1007/s00340-013-5669-x> (cit. on pp. 29, 58).
- [65] R. S. Van Dyck, D. L. Farnham, S. L. Zafonte, and P. B. Schwinberg. "Ultrastable superconducting magnet system for a penning trap mass spectrometer." In: *Review of Scientific Instruments* 70.3 (1999), pp. 1665–1671. DOI: 10.1063/1.1149649. eprint: <https://doi.org/10.1063/1.1149649>. URL: <https://doi.org/10.1063/1.1149649> (cit. on pp. 29, 33).
- [66] Marius Tremer. "Untersuchung und Optimierung des externen Ladens von Ionen bei THE-Trap." deu. MA thesis. Heidelberg: Ruprecht-Karls-Universität, Oct. 2011 (cit. on p. 32).
- [67] Sebastian Dennis Streubel. "Kontrolle der Umwelteinflüsse auf THE-Trap am Beispiel der Bestimmung des Massenverhältnisses von Kohlenstoff-12 zu Sauerstoff-16. Ph.D. thesis." In: *Heidelberg University Faculty of Physics and Astronomy* (2014). URL: <http://www.ub.uni-heidelberg.de/archiv/16870> (cit. on pp. 34, 39).
- [68] Marc Schuh. "Simulations of the image charge effect in high-precision Penning." In: *PhD Thesis, University of Heidelberg* (2019) (cit. on pp. 38, 61).
- [69] F. DiFilippo, V. Natarajan, M. Bradley, F. Palmer, and D. E. Pritchard. "Accurate Atomic Mass Measurements from Penning Trap Mass Comparisons of Individual Ions." In: *AIP Conference Proceedings* 323.1 (1994), pp. 149–175. DOI: 10.1063/1.2946003. eprint: <https://aip.scitation.org/doi/pdf/10.1063/1.2946003>. URL: <https://aip.scitation.org/doi/abs/10.1063/1.2946003> (cit. on p. 62).
- [70] Tomas Fritioff, Conny Carlberg, Guilhem Douysset, Reinhold Schuch, and Ingmar Bergström. "Recent Progress with the SMILETRAP Penning Mass Spectrometer." In: *Atomic Physics at Accelerators: Mass Spectrometry*. Ed. by David Lunney, Georges Audi, and H.-Jürgen Kluge. Dordrecht: Springer Netherlands, 2001, pp. 231–244 (cit. on p. 62).
- [71] G Savard et al. "Q Value of the Superalloved Decay of V 46 and Its Influence on V u d and the Unitarity of the Cabibbo-Kobayashi-Maskawa Matrix." In: *Physical review letters* 95 (Oct. 2005), p. 102501. DOI: 10.1103/PhysRevLett.95.102501 (cit. on p. 62).

- [72] Ernst Otten. "Searching the absolute neutrino mass in tritium β -decay—interplay between nuclear, atomic and molecular physics." In: *Hyperfine Interactions* 196.1 (Feb. 2010), pp. 3–23. DOI: [10.1007/s10751-009-0150-2](https://doi.org/10.1007/s10751-009-0150-2). URL: <https://doi.org/10.1007/s10751-009-0150-2>.
- [73] Marcus Beck and the Katrin collaboration. "The KATRIN experiment." In: *Journal of Physics: Conference Series* 203.1 (2010), p. 012097. URL: <http://stacks.iop.org/1742-6596/203/i=1/a=012097>.
- [74] Robert S. Van Dyck, David B. Pinegar, Seth Van Liew, and Steven L. Zafonte. "The UW-PTMS: Systematic studies, measurement progress, and future improvements." In: *International Journal of Mass Spectrometry* 251.2 (2006). ULTRA-ACCURATE MASS SPECTROMETRY AND RELATED TOPICS Dedicated to H.-J. Kluge on the occasion of his 65th birthday anniversary, pp. 231–242. DOI: <https://doi.org/10.1016/j.ijms.2006.01.038>. URL: <http://www.sciencedirect.com/science/article/pii/S1387380606000650>.
- [75] M. E. Wieser. "Atomic weights of the elements 2005 (IUPAC Technical Report)." In: *Pure and Applied Chemistry* 78.11 (2009), pp. 2051–2066. URL: <https://www.degruyter.com/view/j/pac.2006.78.issue-11/pac200678112051/pac200678112051.xml>.

ACKNOWLEDGMENTS

In addition to acknowledging the people in my life, I would like to acknowledge the main challenge I faced as a PhD student.

One of my main interests from an early age was to be free, to question society and its behaviour and not to be manipulated by it. This was possibly a reaction to the nationalistic Israeli educational system. Out of all the subjects I came in contact with, physics seemed to be the most free of bias and arbitrary facts, as close to the “objective truth” as possible, hence my reason for studying it at the university.

However, along the years I realized that, although it may sound paradoxical at first, it is not experimentation with the external world, but rather self-experimentation that offers me the most direct contact with reality. Through attentive, honest, curious and brave interactions with people and with myself, for instance through conversation, meditation, improvisational theatre, contact improvisation dance, yoga and tai chi, my attention is drawn away from the thoughts continuously generated by my ever attention-seeking, calculating, fear-driven mind. As a result I no longer identify myself with them, thus having the attention to observe and experience life as it is in the present moment. Living in the present moment, even for brief moments, is a gift of a magnitude I cannot describe in words.

I try to incorporate attentiveness, honesty, bravery and curiosity into my daily life, including in my interaction with my colleagues at the institute. There I found it especially challenging, as most of them did not seem to understand or appreciate my behaviour. Thus at times I felt misunderstood, unappreciated, lonely and frustrated at the institute. Luckily I found a group of like-minded people in Heidelberg, with whom I blossomed on a personal, social and romantic level, discovering new interests and hobbies, new friends and my first relationship. I acknowledge both my social environment at the institute and my friends in Heidelberg for helping me grow in the same direction using different impulses.

Thank you to:

The administration, especially **Frau Dücker**, **Frau Hollmach** and **Gabi Weese** for your help. Thank you **Gabi** for the readiness to also share on a personal level during the short but warm interactions on the way to and back from Klaus' office.

The radiation safety team, especially **Ralf Lackner** and **Jochen Schreiner**, for your friendly attitude and willingness to help.

The Blaum group members:

Antonia Schneider - for your honesty.

Marius Müller, **Tim Sailer**, **Kathrin Kromer**, **Antoine de Roubin**, **Bingsheng Tu**, **Christoph Schweiger**, **Charlotte König**, **Menno Door**, **Sergey Eliseev**, **Stefan Dickopf** and **Robert Wolf** - for your friendliness.

Alex Egl - for proof-reading parts of this thesis.

Sven Sturm - for the meeting in your family farm.

Wenjia Huang - for the AME-related analysis of the neon mass measurement results.

Rima Schüssler - for proof-reading parts of this thesis and for investing time and energy in making the work environment socially richer, even if I personally chose not to participate in most of the activities.

Andreas Weigel - for the encouraging words you gave me at lunch a few weeks before your defense.

Andreas Mooser - for proof-reading this thesis and for continuing the experiment, providing an opportunity for me to have closure by working in the same lab but with a different atmosphere.

Ralph Zilly - for filling our magnet with liquid nitrogen and liquid helium and for making my work environment less stressed with your humor.

Ioanna Arapoglou - for the personal conversations during seminars and conferences.

Pavel Filianin - for the personal conversations during seminars and conferences and for attending a free hugs event I organised. Thank you for the workout breaks, they were great for resetting my head.

Alexander Rischka - for the amusing philosophical discussions regarding cannibal vegans and chicken-slinging Jews. Thank you for your frequent lab visits, for providing scientific advice and for showing curiosity and appreciation for who I am. Thank you for the bike trips to the Kollersee and to the Erlebnisbad Miramar with the crazy slides. Thank you for some honest and brave things that you said.

Jiamin Hou - for hosting me in Mainz, for visiting me in Heidelberg, for your unique and inspiring way of seeing the world and for sharing it with me.

The THe-Trap group members:

Sebastian Streubel - for inspiring me to ride the bikes more often, for showing me the wonders of ducktape, for singing the Dragon Ball Z song in German in a helium-induced high-pitch voice and for introducing me to the data acquisition system and to the pressure stabilization system.

Martin Höcker - for picking me up from the bus station on one cloudy afternoon in November 2014, for inviting me to several Jewish dinners along with your wife Hermine, for driving me to the makers space and to see a movie, for the many hours spent teaching me about the experiment, for your thesis, which was the main reference I used for writing this one, for your many Matlab scripts, some of which were in use until the very end, and for your data analysis files, which I used as a reference for my own.

Marc Schuh - for renting me your student apartment for my first two weeks, for going on a super fast drive on the highway, for watching fireworks together and for saying veganism is an interesting concept. Thank you for programming the new controller and independently analyzing the neon mass measurements. Thank you for the two hours talk on your balcony late at night the day before you left where we discussed our challenges with one another and with ourselves in a personal and honest manner.

Jochen Ketter - for doing such a great job with Martin's PhD hat, for teaching me the German version of the opening song of Pokemon and other shows and for the walk in the forest. Thank you for your great generosity and willingness to help, for sharing your impressive knowledge and intellect regarding physics and other topics, and for being sensitive enough to notice some of the social difficulties I was experiencing and encouraging me.

Klaus Blaum - for inviting me to the institute for an interview and for arranging social activities during the MATS days, such as the time we ran together with Pasha. Thank you for always showing me great respect, trust and understanding, including during professional and social hardships. Thank you especially for two particular instances that come to mind where your

words greatly encouraged me, making me feel substantially more comfortable at the institute. Given the same social conditions but a supervisor who is not as sensitive, supporting and respectful as you are, I would have most probably abandoned my PhD.

My friends in Germany - For experimenting together with me in matters of the body and the heart, for making Heidelberg feel like a second home, for your appreciation and for your love. Thank you for supporting me and (more than) counter-balancing my social condition at the Institute.

Theresa - for the many things I learned and keep learning from you. Thank you for giving me both the space and the impulses to continue exploring and developing. Thank you for your curiosity and bravery. Thank you for your love.

The Israeli side:

My M. Sc. Supervisor Guy Ron - Thank you for your great support during my bachelors project and my masters, for supporting me in my decision to study for my PhD in Heidelberg and for connecting me to Klaus.

My friends in Israel - for the loving environment in which I was lucky to grow up in and for the bonds that remain warm, lively and relevant even after moving to another continent.

My family - for your love. Especially **my parents** for always supporting me and respecting my decisions, despite how unusual they sometimes were. **אני אוהב אתכם**